STUDY OF THE DEVELOPMENT OF SHELL CLOSURES AT N=32,34 AND APPROACHES TO SUB-SEGMENT INTERACTION-POINT DETERMINATION IN 32-FOLD SEGMENTED HIGH-PURITY GERMANIUM DETECTORS

By

Dan-Cristian Dinca

A DISSERTATION

Submitted to
Michigan State University
in partial fulfillment of the requirements
for the degree of

DOCTOR OF PHILOSOPHY

Department of Physics and Astronomy

2005

ABSTRACT

STUDY OF THE DEVELOPMENT OF SHELL CLOSURES AT N=32,34 AND APPROACHES TO SUB-SEGMENT INTERACTION-POINT DETERMINATION IN 32-FOLD SEGMENTED HIGH-PURITY GERMANIUM DETECTORS

By

Dan-Cristian Dinca

The even $^{52-56}$Ti isotopes have been studied with intermediate-energy Coulomb excitation and absolute $B(E2; 0^+ \rightarrow 2_1^+)$ transition rates have been deduced. Our data confirm the presence of a sub-shell closure at neutron number $N = 32$ in neutron-rich titanium isotopes above the doubly-magic nucleus ^{48}Ca and provide no direct evidence for the predicted $N = 34$ closure. Large-scale shell model calculations with the most recent effective interactions are unable to reproduce the magnitude of the measured strengths in the semi-magic Ti isotopes and their strong variation with neutron number.

Sub-segment position resolution of the γ-ray interaction points has been demonstrated for the cylindrically-symmetric 32-fold segmented HPGe detectors of the NSCL/MSU Segmented Germanium detector Array (SeGA) using digital electronics. Waveforms of the real charge signals from segments that contain interaction points and induced charge signals from neighboring segments were digitally recorded by 100 MHz ADCs. Simple integrated quantities (amplitudes, areas, peak times) were extracted from the waveforms. By analyzing the asymmetry of the induced signals we could determine the proximity of the interaction point to segments without net-charge deposition, attaining sub-segment position resolution along the crystals symmetry axis. The radial position of the interaction point was determined through an analysis of the rise times of the real charge signals. Although less precise than other methods involving a complete waveform analysis, the use of integrated quantities simplifies the problem of sub-segment interaction position estimation.

to my wife, Cornelia

ACKNOWLEDGMENTS

I am grateful to my advisor, Thomas Glasmacher, for insightful guidance through all the projects I have been involved in. He gave me the freedom to develop at my own pace and try my own ideas. I learned a lot from him.

For more than a year Robert Janssens has been my second advisor. Robert made the titanium experiment an enlightening and enjoyable endeavor. I got more attention from him than I ever deserved.

I am indebted to Alexandra Gade for her help on the analysis of the titanium experiment. Her patient answers to my not-so-smart questions made me get a deeper understanding of what I was studying.

Chris Campbell helped me on the detector development study. Our long discussions were inspiring to me.

I thank the present and former members (or associated members) of the NSCL's Gamma Group, Matt Bowen, Jenny Church, Jon Cook, Joachim Enders, Zhiqiang Hu, Pat Lofy, Wil Mueller, Heather Olliver, Ben Perry (I still remember your parties), Russ Terry, and Katie Yurkewicz.

Running the NSCL-02002 experiment, "B(E2) Rates in Even-Even $^{52-56}$Ti", was a team effort, involving more than NSCL's Gamma Group. People that made it possible and were not mentioned before are Daniel Bazin, Mike Carpenter, Partha Chowdhury, Alick Deacon, Sean Freeman, Michio Honma, Filip Kondev, Jean-Luc Lecouey, Sean Liddick, Paul Mantica, Taka Otsuka, Bryan Tomlin, and Ken Yoneda.

I thank Professors B.A. Brown, J. Linneman, S.D. Mahanti, B. Pope and B. Sherrill for serving in my PhD Guidance Committee. Dr. Brown developed the theoretical models and calculations for the energies and reduced transition probabilities for the neutron-rich titanium isotopes I have measured.

Finally, I thank Cornelia, who deserves my gratitude most. I am blessed to have

met her.

Contents

List of Figures

List of Tables

Chapter 1

Introduction

Beyond the valley of β stability, the large asymmetry between proton and neutron numbers is expected to modify the shell structure. Over the last few years, the appearance and disappearance of magic numbers [2–6] and the formation of new regions of deformation [7] have been observed. Phenomena such as the "island of inversion", where the shell inversion occurs near the ground state, illustrate that significant changes can occur in the nuclear structure of neutron-rich nuclei. Modifications in the oribital energy spacings affect properties such as nuclear excitation modes and nuclear shapes.

Specialized experimental methods have been developed to measure quantum-mechanical observables with low exotic beam rates in order to elucidate the structure of neutron-rich nuclei. Using thick secondary targets to increase luminosity, the methods involved include γ-ray spectroscopy following deep-inelastic scattering, Coulomb excitation of fast projectiles or reaccelerated beams, β-decay studies, or transfer reactions.

Beta-decay studies of ^{56}Cr indicated a possible sub-shell gap at neutron number N=32 [8]. The nearest doubly-magic nucleus is ^{48}Ca (see Figure 1.1) and if the magic numbers established for stable nuclear species are considered, the next sub-shell gap would be expected at N=40. A possible cause of the orbital reordering has been

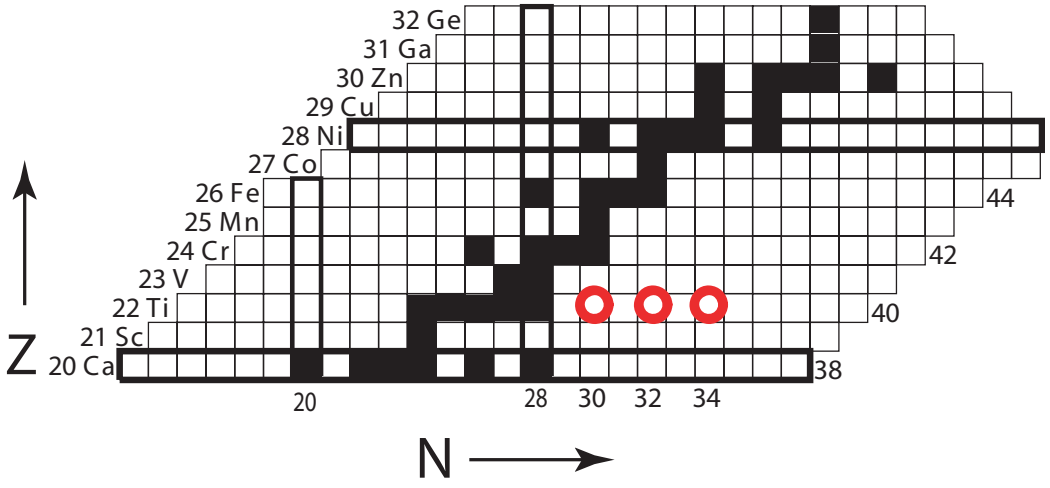

Figure 1.1: A section of the nuclear chart showing the region of interest. The black squares are the β-stable nuclei. The three titanium isotopes (^{52,54,56}Ti) are circled.

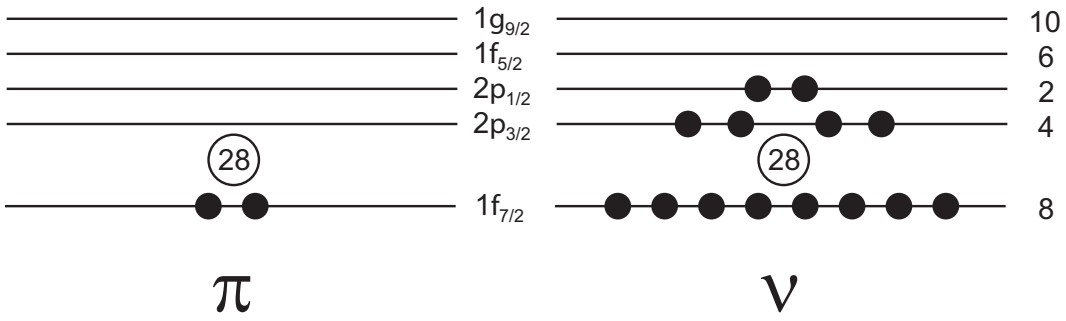

Figure 1.2: Simplistic view of the orbital structure for ^{56}Ti above the $1f_{7/2}$ shell

identified as the proton-neutron monopole interaction [9]. As the number of protons occupying the $\pi f_{7/2}$ shell decreases, the $\pi f_{7/2} - \nu f_{5/2}$ monopole pairing interaction strength weakens. As a consequence, the neutron orbital $\nu f_{5/2}$ is shifted up in energy. Coupled with the rather significant spin-orbit splitting between the $\nu p_{1/2}$ and $\nu p_{3/2}$ orbitals, this may lead to new sub-shell gaps (Figure 1.2). Shell-model calculations using the effective interaction GXPF1 [10] revealed the possibility of sub-shell gaps at neutron numbers N=32 and N=34.

To investigate the development of these shell gaps further, β-decay measurements at the NSCL [11, 12] in conjunction with prompt γ-ray spectroscopy following deep-inelastic reactions at Gammasphere [13, 14] were performed for ^{54}Ti and ^{56}Ti. The energies of the first excited states in these nuclei supported the notion of a shell gap at

N=32, but not at N=34. It has been shown that knowledge of the level scheme alone is not sufficient to identify shell closures [15, 16]. To search for additional evidence of the newly proposed shell gaps, we have measured an additional observable, which provides a direct measure of the degree of collectivity in a nucleus. The reduced transition matrix elements to the first excited 2^+ state in ^{52,54,56}Ti have been determined via intermediate-energy projectile Coulomb excitation [17] at the Coupled Cyclotron Facility of the National Superconducting Cyclotron Laboratory. Coulomb excitation is a sensitive probe to study the characteristics of quadrupole collectivity in nuclei with even number of protons and neutrons [18–20]. Simultaneous with the measurement of the de-excitation γ-ray energy, giving the energy spacing between the two bound states, the Coulomb excitation cross section is related to the electromagnetic matrix elements B(Eλ) and B(Mλ) of multipolarity λ. The B(E2) strength relates to the degree of collectivity and provides insight into details of the many-body wave functions for nuclei near closed shells. The first experiment involving Coulomb excitation of radioactive beams was performed by inelastically scattering a ^{8}Li radioactive beam at 14.6 MeV on a ^{nat}Na target [21–23]. Gamma-rays emitted by exotic beams undergoing Coulomb excitation were measured first in an experiment involving scattering of ^{76}Kr on a ^{208}Pb target at 237 MeV [24].

The first part of the thesis describes the measurement of the reduced transition probabilities to the first 2^+ state in the exotic nuclei ^{52}Ti, ^{54}Ti and ^{56}Ti via the intermediate-energy Coulomb-excitation method and discusses the development of shell closures for neutron numbers N=32 and N=34. The experimental method and the analysis procedure have been extensively described in numerous publications [17, 25–28]. Emphasis will be placed on the characteristics of this experiment and the nuclei investigated.

Experiments aimed at studying very exotic nuclei are characterized by low beam rates. Gamma-rays emitted from fast moving nuclei (v/c=0.3) are detected at Doppler shifted energies in the laboratory frame. Under current experimental conditions mea-

surements in the regime of limited statistics would gain from an enhanced peak-to-background ratio. Even for relatively large bin sizes of the γ-ray energy spectra in the projectile frame (Figures 2.10, 2.11, 2.12,2.13) the peak widths are large. An important factor in the energy resolution of a photopeak is the Doppler reconstruction mechanism. A better correction of the Doppler broadening would reduce the number of background counts under the peak, thus reducing the uncertainty in the peak area and any cross sections derived from it. Energy resolution is also a crucial when two γ-ray transitions close in energy have to be resolved.

The concept of γ-ray tracking gained a lot of attention in the past years. Collaborations like GRETA/GRETINA [29,30] and AGATA [31] were formed to address the use of γ-ray tracking for nuclear physics. The method involves the determination of the γ-ray interaction points inside a semiconductor-based detector with high spacial accuracy, down to the size of the charge cloud or better (1-2 mm). Based on the interaction positions, the path of the γ-ray is reconstructed inside the detector. The path reconstruction process involves the digitization of the signals from highly-segmented semiconductor detectors (usually high-purity germanium). The recorded signals are fitted with a base of precalculated signals to derive the interaction positions. Once the positions are known, all possible scattering histories are computed and a figure of merit is built. The path with the highest figure of merit is chosen to be the photon path. If the γ-ray scattering path is known, also the first point of interaction is determined. Knowing the first interaction point is crucial for Doppler correction. The relation between the photon energy in the projectile frame and the laboratory frame is given by:

$$E_{proj} = \gamma E_{lab}(1 - \beta cos\theta) \tag{1.1}$$

where E_{lab} and E_{proj} are the γ-ray energies in the laboratory frame and projectile

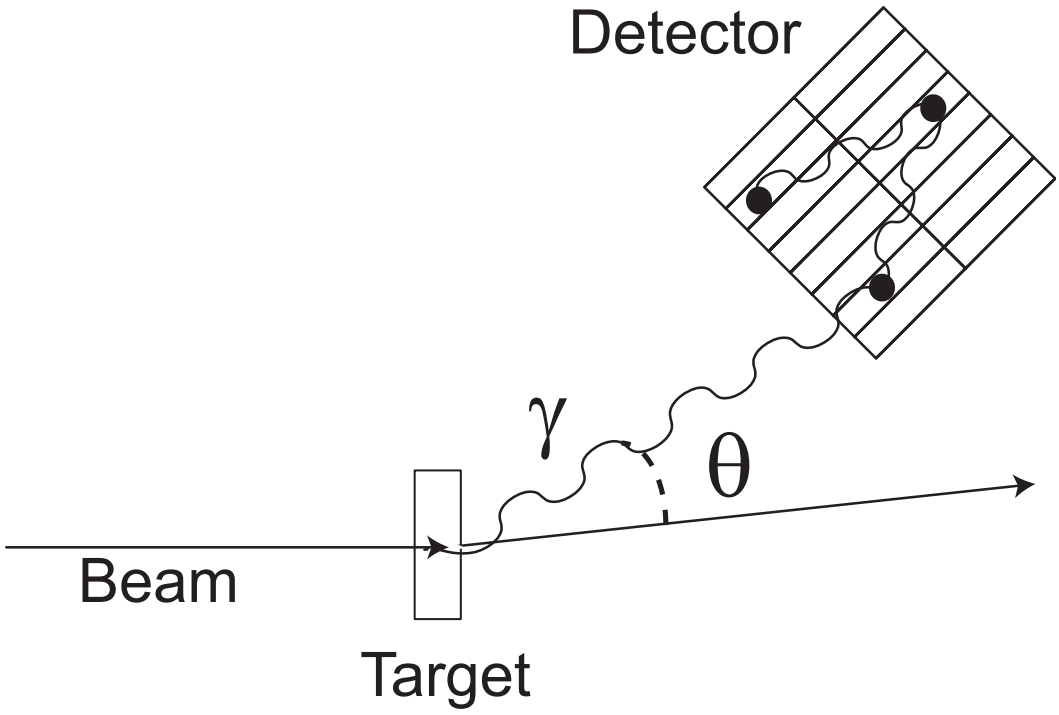

Figure 1.3: Example of γ-ray interaction with a segmented detector

frame, respectively. The beam velocity is $\beta = v/c$ and

$$\gamma = \frac{1}{\sqrt{1-\beta^2}} \tag{1.2}$$

is the relativistic factor. The angle θ is taken between the scattered beam and the γ-ray direction. This angle can be calculated by knowing the position where the nucleus emitted the photon and the point where the γ-ray first interacted with the detector. Figure 1.3 depicts an example of a γ-ray interacting three times within a segmented detector. Only the first interaction point defines the angle necessary for Doppler reconstruction.

The second part of the thesis deals with a study targeted at improving the interaction position resolution for the segmented germanium detectors used at NSCL for γ-ray spectroscopy. A sub-segment interaction position resolution offers the possibility of a better Doppler reconstruction for in-beam γ-ray spectroscopy, leading to an enhanced peak-to-background ratio. It will be demonstrated that a simpler approach

can yield good performance, without involving a full γ-ray tracking which requires expensive hardware and software solutions.

Chapter 2

Reduced transition probabilities to the first 2^+ state in ^{52,54,56}Ti and development of shell closures at $N = 32, 34$

2.1 Overview

Shell structure is the foundation for much of our present understanding of atomic nuclei, although most of our knowledge about the ordering and location in energy of the single-particle states remains empirical. In this context, neutron-rich nuclei have become the focus of recent theoretical and experimental efforts.[1] The on-going investigations are motivated to a large extent by expectations of substantial modifications of shell structure in nuclei with a sizable neutron excess [33–38]. Such alterations can have a considerable impact on global nuclear properties such as the nuclear

[1]Reprinted excerpts and figures with permission from: D.-C. Dinca, R.V.F. Janssens, A. Gade, D. Bazin, R. Broda, B.A. Brown, C. M. Campbell, M. P. Carpenter, P. Chowdhury, J. M. Cook, A.N. Deacon, B. Fornal, S. J. Freeman, T. Glasmacher, M.Honma, F.G. Kondev, J.-L. Lecouey, S. N. Liddick, P. F. Mantica, W. F. Mueller, H. Olliver, T. Otsuka, J. R. Terry, B. A. Tomlin, K. Yoneda, Physical Review C, Volume 71, Number 4, 041302, 2005. Copyright 2005 by the American Physical Society. [32]

shape or the type of excitations characterizing the low-energy level schemes. One of the proposed causes for the reordering of single-particle states is the proton-neutron monopole interaction [9]. This interaction has recently been invoked to account for the presence of a sub-shell gap at $N = 32$ in neutron-rich nuclei located in the vicinity of doubly-magic $^{48}_{20}\mathrm{Ca}_{28}$. At present, experimental evidence for the existence of this $N = 32$ gap rests solely on the low and medium spin ($I \leq 12$) level sequences of the ^{52}Ca [39], $^{52-56}$Ti [11, 13, 14] and $^{52-58}$Cr [8] even-even isotopes.

It is the purpose of our work to track the evolution of this sub-shell gap further, through the measurement of the electromagnetic transition rates to the first excited states of the ^{52,54,56}Ti isotopes with the technique of intermediate-energy Coulomb excitation [17]. Such rates provide one of the most sensitive probes of nuclear structure. In deformed nuclei, transition strengths are related to the magnitude of the deformation, while in nuclei in the vicinity of closed shells, they are of great value in probing the details of the many-body wavefunctions. In fact, these rates have often highlighted properties that were unexpected on the basis of level energies alone. For example, the $B(E2; 0^+ \rightarrow 2^+_1)$ value in doubly-magic ^{56}Ni was found to be larger than anticipated [16], while that measured for ^{136}Te, with 2 protons and 2 neutrons outside the doubly-magic ^{132}Sn nucleus, is surprisingly small [40].

In the particular case discussed here, the transition rates represent a sensitive test of the most modern effective interactions that have been developed to describe pf-shell nuclei [10]. It is shown that the data support the view of a sizable shell gap at $N = 32$, but that there is no experimental evidence for an additional sub-shell closure predicted to occur at $N = 34$. Moreover, detailed comparisons between the data and the calculations also indicate shortcomings of the proposed effective interactions in reproducing the observed trend of the $B(E2)$ values with neutron number.

Table 2.1: Summary of secondary beam properties.

Beam	Energy (before target) (MeV/nucl.)	Velocity (before target) (v/c)	Velocity (mid target) (v/c)	Target thickness (mg/cm^2)
^{76}Ge	81	0.392	0.375	256
^{52}Ti	89	0.408	0.399	256
^{52}Ti	81	0.408	0.388	518
^{54}Ti	88	0.406	0.398	256
^{56}Ti	88	0.406	0.387	518

2.2 Experimental conditions

2.2.1 Secondary beams

The measurements were carried out at the Coupled Cyclotron Facility of the National Superconducting Cyclotron Laboratory using secondary beams produced in fragmentation of ^{76}Ge primary beam at an energy of 130 MeV/nucleon. Following the 380 mg/cm^2 ^{9}Be production target, the species of interest were selected with the A1900 fragment separator [41] and directed to the target position of the high-resolution S800 magnetic spectrograph [42].

Four settings of the A1900 separator were used in the experiment. First, the ^{76}Ge primary beam was degraded to 81 MeV/nucleon and sent onto a 256 mg/cm^2 ^{197}Au target as a check of the technique and the setup. Following this measurement, secondary beams of the three even Ti isotopes of interest, all with an energy of 89 MeV/nucleon, were then selected in succession and directed onto ^{197}Au targets of 256 mg/cm^2 and 518 mg/cm^2 thickness. The thinner Au target was used with the ^{52}Ti and ^{54}Ti fragments, the thicker with ^{52}Ti and ^{56}Ti. For a primary beam intensity of 10 pnA, the three Ti settings resulted in average rates on target of 9000 Hz (^{52}Ti), 600 Hz (^{54}Ti) and 40 Hz(^{56}Ti). Each incoming beam particle was identified on an event-by-event basis, and the isotopes of interest represented respectively 58, 28 and 10% of the flux of incoming particles. A summary of the secondary beam properties is given in Table 2.1.

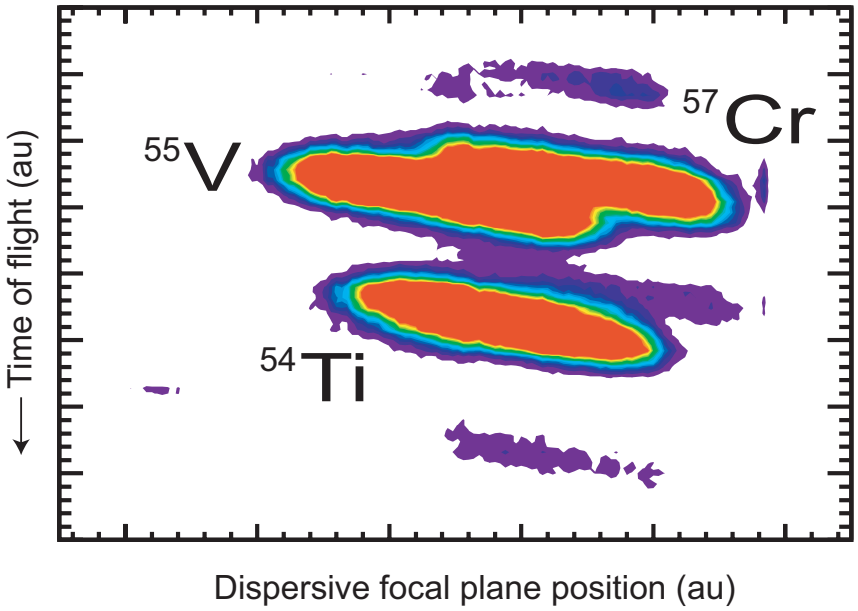

Figure 2.1: Particle identification spectrum for the ^{54}Ti setting. The dispersive focal plane is on the horizontal axis and the time of flight on the vertical axis. The number of counts is color coded and linear scale and saturated at 10% of the full scale.

2.2.2 Particle identification

As an example, the particle-identification spectra are presented for the ^{54}Ti isotope in Figures 2.1, 2.2, and 2.3. A software gate requiring the coincidence of events in both regions of interest in the dispersive focal plane versus time-of-flight spectrum and the time of flight versus energy loss spectrum define the particle identification conditions. The particle time of flight was measured between a scintillator at the object position of the spectrograph and the E1 scintillator at the back of the S800 focal plane. E1 also acted as a particle trigger detector. The focal plane ion chamber measured the energy loss and the Cathode Readout Drift Chambers (CRDCs) provided the beam position and angle on an event-by-event basis. For a detailed description of the S800 spectrograph see References [42] and [43].

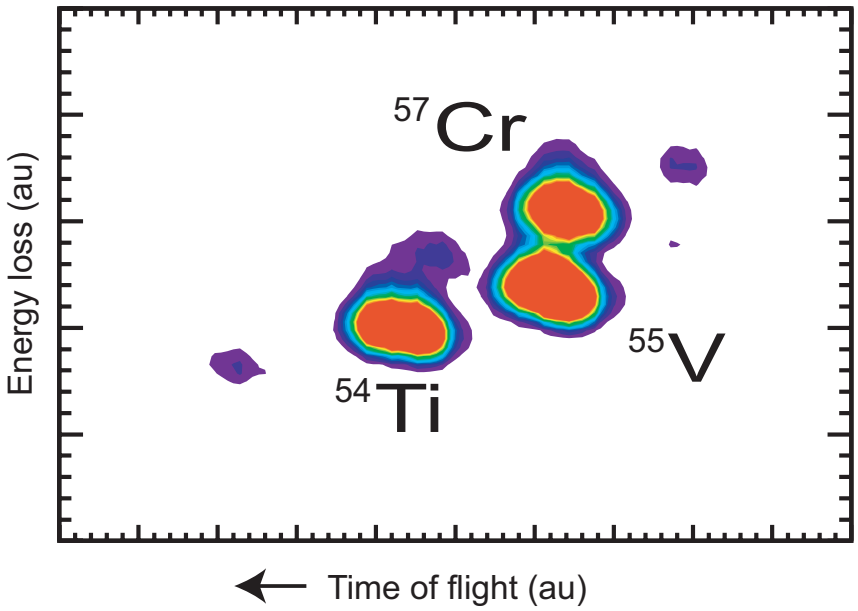

Figure 2.2: Particle identification spectrum for the ^{54}Ti setting. The number of counts is color coded and saturated at 10% of the full scale.

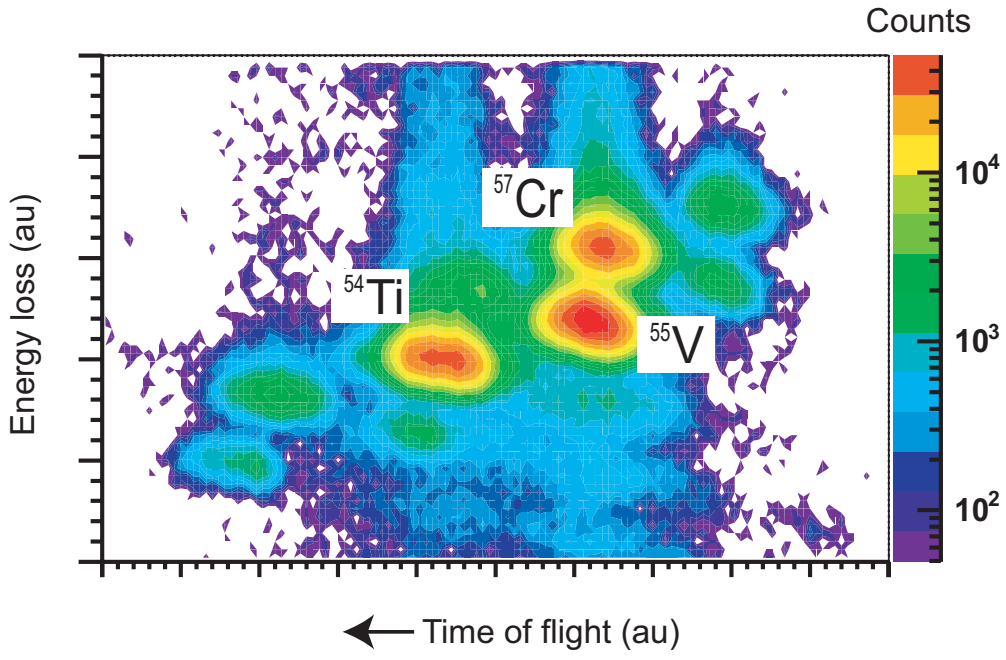

Figure 2.3: Particle identification spectrum for the ^{54}Ti setting. The number of counts is color coded and log scale.

2.2.3 Intermediate-energy Coulomb excitation (theory)

Interactions between the target and projectile nuclei occur above the Coulomb barrier. The preponderence of Coulomb excitations over nuclear reactions can be ensured by selecting only impact parameters larger than the sum of the nuclei radii plus several femtometers. This is equivalent to the selection of the most forward scattering angles [17, 26, 27]. The impact parameter b depends on the scattering angle in the center-of-mass frame θ_{cm} in the following way (Figure 2.4, Equation 2.1).

$$b = \frac{a}{\gamma} \cot\left(\frac{\theta_{cm}}{2}\right), \tag{2.1}$$

where γ is the relativistic factor (1.2) and a is dependent on the projectile and target atomic numbers (Z_{proj} and Z_{tar} respectively) and the reduced mass of the target-projectile system (m_0) via:

$$a = \frac{Z_{proj} Z_{tar} e^2}{m_0\, c^2 \beta^2}. \tag{2.2}$$

$$\frac{1}{m_0} = \frac{1}{m_{proj}} + \frac{1}{m_{tar}}. \tag{2.3}$$

Based on the kinematics of the process a relationship can be established between the scattering angles in the center-of-mass frame (θ_{cm}) and laboratory frame (θ_{lab}).

The theory of relativistic Coulomb excitation was pioneered by A. Winther and K. Alder [25]. Their work assumes that, to first order, the straight-line trajectory of the projectile is perturbed by the recoil, rescaling the impact parameter (Equation 2.4).

$$b \rightarrow b + \frac{\pi a}{2\gamma}. \tag{2.4}$$

Winther and Alder's theory link the reduced transition probabilities in the projectile to the cross section via:

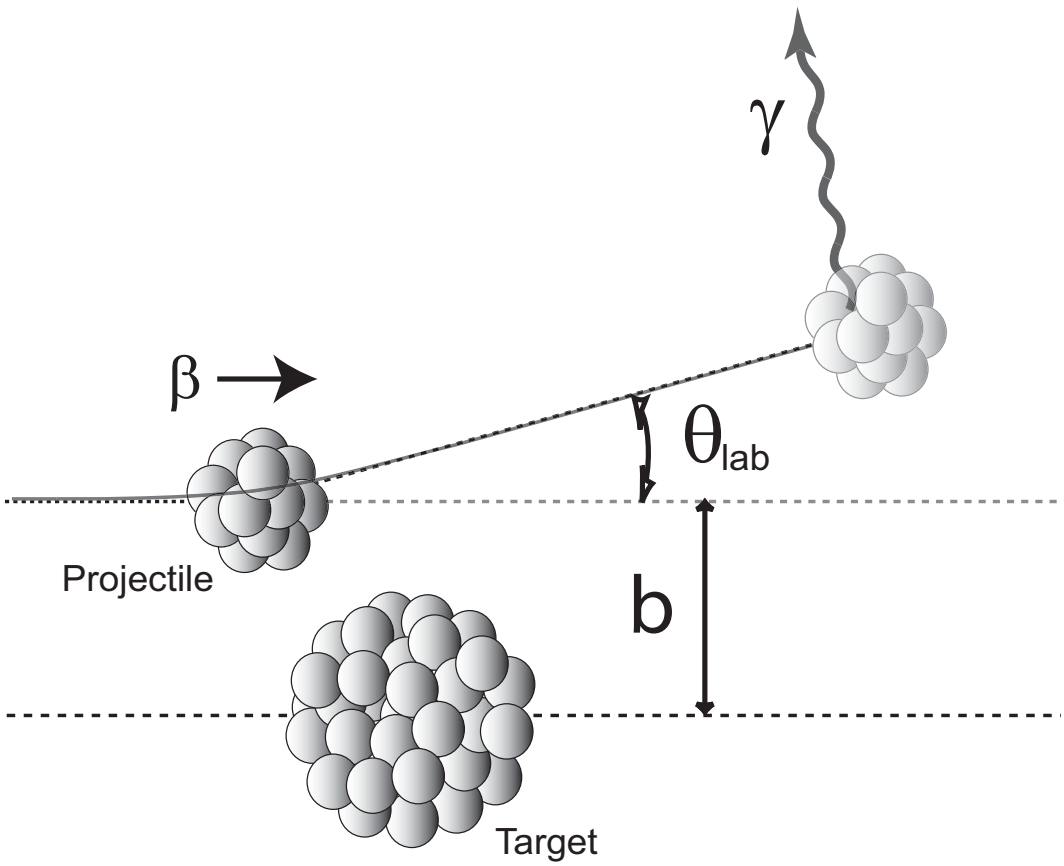

Figure 2.4: Schematics of the projectile-target interaction. The target nucleus is considered at rest after the interaction (infinite mass).

$$\sigma_{\pi\lambda} \approx \left(\frac{Z_{tar}e^2}{\hbar c}\right) \frac{B_{pro}(\pi\lambda, 0 \rightarrow \lambda)}{e^2} \pi\, b_{min}^{2(1-\lambda)} \begin{cases} (\lambda-1)^{-1} & for \lambda \geq 2 \\ 2\,\ln(b_{max}/b_{min}) & for \lambda = 1 \end{cases} \tag{2.5}$$

where π is the parity of transition and λ its multipolarity. The limits of the impact parameters considered are denoted b_{min} and b_{max}.

2.2.4 Gamma-ray spectroscopic system

The Au target was surrounded by SeGA, an array of fifteen, 32-fold segmented, germanium detectors [44] arranged in two rings with central angles of 90° and 37° relative to the beam axis (See Figure 2.5). The forward ring contained 7 detectors while the other 8 were located at 90°. The high degree of segmentation is necessary to correct for the Doppler shift of the γ rays emitted in flight (on an event-by-event basis).

2.3 Analysis method

The reduced transition matrix elements $B(E2; 0^+ \rightarrow 2_1^+)$ can be deduced from the Coulomb excitation cross section using the exact relationship of the Equation 2.5 (Reference [25]). Simulations with the code GEANT3 [45] reproduced the efficiency of SeGA measured with the standard calibration source ^{152}Eu source and provided the detector response for the in-beam data by taking into account the Lorentz boost (see Reference [27] for further details). This reference also describes the particle identification and the determination of the scattering angle carried out on an event-by-event basis with the focal plane detector system [43] of the S800 spectrograph.

The Coulomb excitation cross section is given by the relationship

$$\sigma = \frac{N_\gamma}{\epsilon_{tot}\ N_{target}\ N_{beam}} \tag{2.6}$$

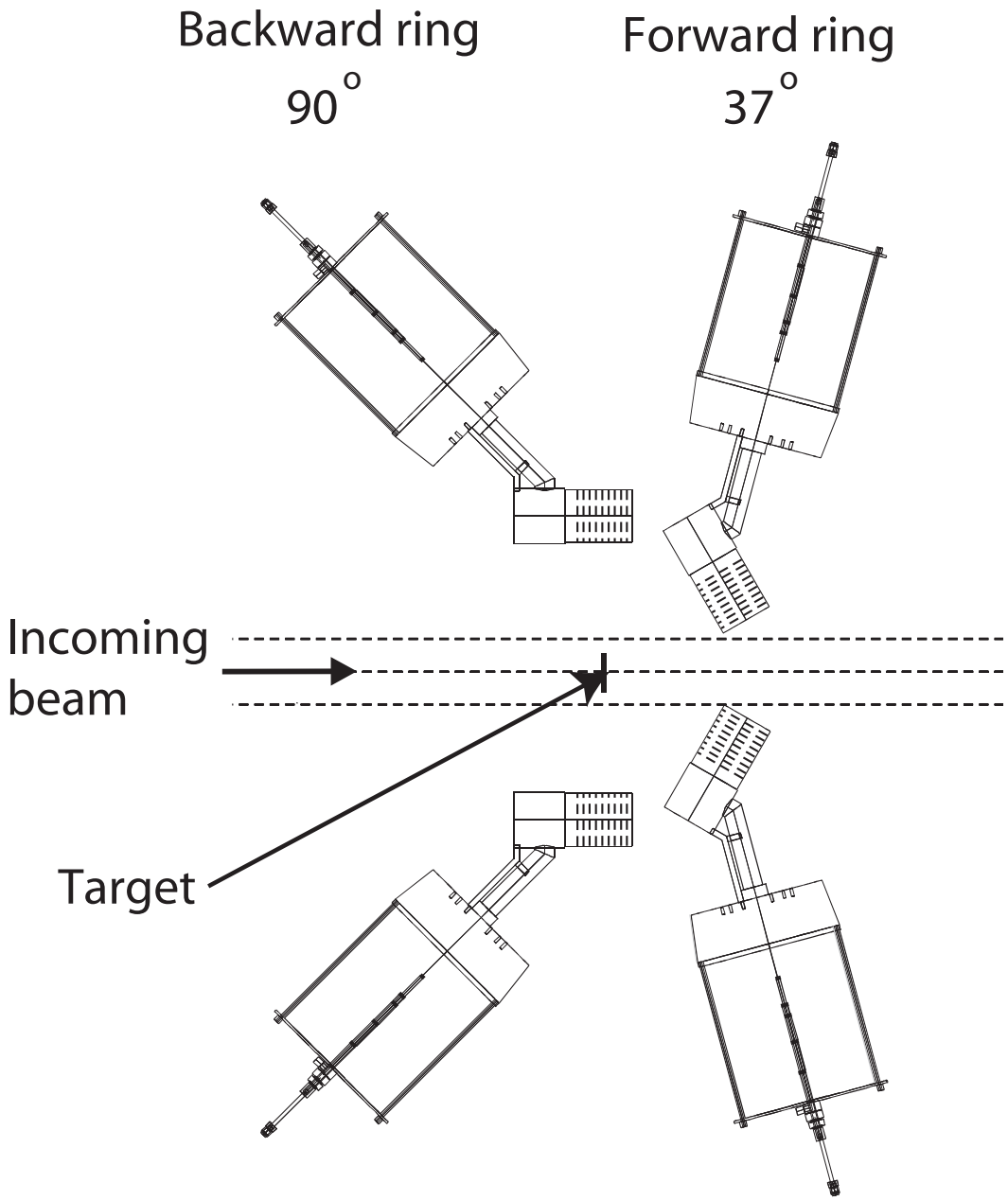

Figure 2.5: The segmented germanium detectors distributed in two rings around the secondary target position.

N_γ is the number of photons de-exciting for the state of interest. If the state is not only populated via Coulomb excitation, feeding corrections have to be applied. This was not the case for the present work. ϵ_{tot} is the total efficiency of experimental setup, including the gamma-ray detector effiency, particle detector efficiency and data acquisition system dead time corrections. N_{target} is the number of nuclei in the target, and N_{beam} is the number of incoming projectiles. The number of nuclei in the target (density per unit area) is calculated as

$$N_{target} = \frac{N_A \times \rho}{A}, \tag{2.7}$$

where N_A is Avagadro's number ($N_A = 6.022 \times 10^{23}$ particles/mol), ρ is the target density (thickness) in g/cm^2, and A is the atomic mass of the target nuclei in g/mol. N_{beam} is calculated by multiplying the number of particles integrated in the down scaled [2] (D/S) particle identification spectrum $N_{partD/S}$ times the D/S factor set in the trigger electronics $f_{D/S}$.

$$N_{beam} = N_{partD/S} \times f_{D/S}. \tag{2.8}$$

The total efficiency is the sum of the efficiencies of the two rings (Figure 2.5).

$$\epsilon_{tot} = \epsilon_{37^o} + \epsilon_{90^o} \tag{2.9}$$

For one ring of SeGA, the efficiency using the method of GEANT simulations, is

$$\epsilon_{ring} = \epsilon(E_\gamma)_{lab}^{\text{GEANT}} \times \delta_{\text{GEANT}} \times A_f. \tag{2.10}$$

[2] To reduce the dead time of the data acquisition system the trigger condition is set to a logic "OR" between the particle detector (S800) trigger and the γ-ray detector (SeGA) trigger in coincidence with S800. The particle trigger is down scaled, meaning that only one every number of events in recorded. This is equivalent to a random sample of the particles not detected in coincidence with γ-rays.

where $\epsilon(E_\gamma)_{lab}^{\text{GEANT}}$ is the efficiency simulated with GEANT in the projectile frame assuming an isotropic emission, δ_{GEANT} is the GEANT scaling coefficient, and A_f is an angular factor that accounts for the anisotropic angular distribution of the emitted γ-rays.

A discrepancy on the order of 1 to 3.5 percent is found between the GEANT-simulation photopeak efficiency for the calibration sources and the measured efficiency. To account for this discrepancy when the efficiency in the projectile frame is calculated, a scaling coefficient δ_{GEANT} is defined for the energy range of the γ-rays of interest. The uncertainty for this coefficient also includes the uncertainty in the value of the calibration source activity.

The magnetic substates are not evenly populated by the Coulomb excitation. This process should be accounted for in the analysis. Discussions regarding the γ-ray angular distribution ($W(\theta_{proj})$) can be found in References [20,25,46,47]. $N_{\theta_{proj}}$ is the number of γ-rays detected by the detector array at a given angle θ. The index "proj" indicates that the quantity is considered in the reference frame of the projectile.

$$A_f = \frac{\sum_{\theta_{proj}} N_{\theta_{proj}} W(\theta_{proj}) \sin\theta_{proj}}{\frac{1}{4\pi}\sum_{\theta_{proj}} N_{\theta_{proj}} \sin\theta_{proj}} \tag{2.11}$$

The uncertainty of the experimental cross section is

$$\Delta\sigma = \sigma\sqrt{\left(\frac{\Delta N_\gamma}{N_\gamma}\right)^2 + \left(\frac{\Delta N_{beam}}{N_{beam}}\right)^2 + \left(\frac{\Delta N_{target}}{N_{target}}\right)^2 + \left(\frac{\Delta\epsilon_{tot}}{\epsilon_{tot}}\right)^2} \tag{2.12}$$

where

$$\Delta N_\gamma = \sqrt{N_\gamma} \tag{2.13}$$

$$\Delta N_{target} = N_{target}\sqrt{\left(\frac{\Delta\rho}{\rho}\right)^2 + \left(\frac{\Delta N_A}{N_A}\right)^2} \tag{2.14}$$

A_f and $\epsilon(E_\gamma)_{lab}^{\mathrm{GEANT}}$ are based on GEANT simulations and analytical calculations and the uncertainties induced by them are considered negligible compared to the other sources. The main source of uncertainty are the peak area (N_γ) and the simulation scaling coefficient δ_{GEANT} (5 - 6%).

2.4 Results

Inelastic scattering of the primary ^{76}Ge beam on a ^{197}Au target was used to validate the experimental technique. In ^{76}Ge, the reduced transition probability has previously been determined through Coulomb excitation at energies below the Coulomb barrier [48]. The relevant spectrum measured in the projectile frame, for scattering angles restricting the impact parameter of the reaction to values larger than the sum of the two nuclear radii plus 5 fm, is given in Figure 2.10. Using the Winther-Alder theory of relativistic Coulomb excitation [25], the angle-integrated cross section measured under these conditions translates into a value of $B(E2; 0^+ \rightarrow 2_1^+) = 2923(346)$ $e^2\mathrm{fm}^4$ that compares well with the adopted one of 2780(30) $e^2\mathrm{fm}^4$ [48]. From the same measurement, a similar comparison can be made for the excitation of the Au target and good agreement is again found between the present data and the literature [49]: $B(E2; 3/2^+ \rightarrow 7/2^+) = 4472(951)$ versus 4494(409) $e^2\mathrm{fm}^4$.

For all settings the reduced transition probability to the $7/2^+$ state in the Au target was also calculated. Figure 2.6 shows the $B(E2; 3/2^+ \rightarrow 7/2^+)$ for all settings. The first value labeled ^{52}Ti is for the 256 mg/cm^2 ^{197}Au target thickness and the second is for the 518 mg/cm^2. The value labeled "adopted" is the one from [49]. The velocity of the excited ^{197}Au target nuclei is very small and no Doppler correction is needed. The de-excitation gamma-ray peaks have higher resolution (Figure 2.7) than the ones for gamma-rays emitted by fast moving nuclei because the Doppler broadening has no significant contribution at that velocity. The ^{197}Au nuclei from the target can be considered at rest.

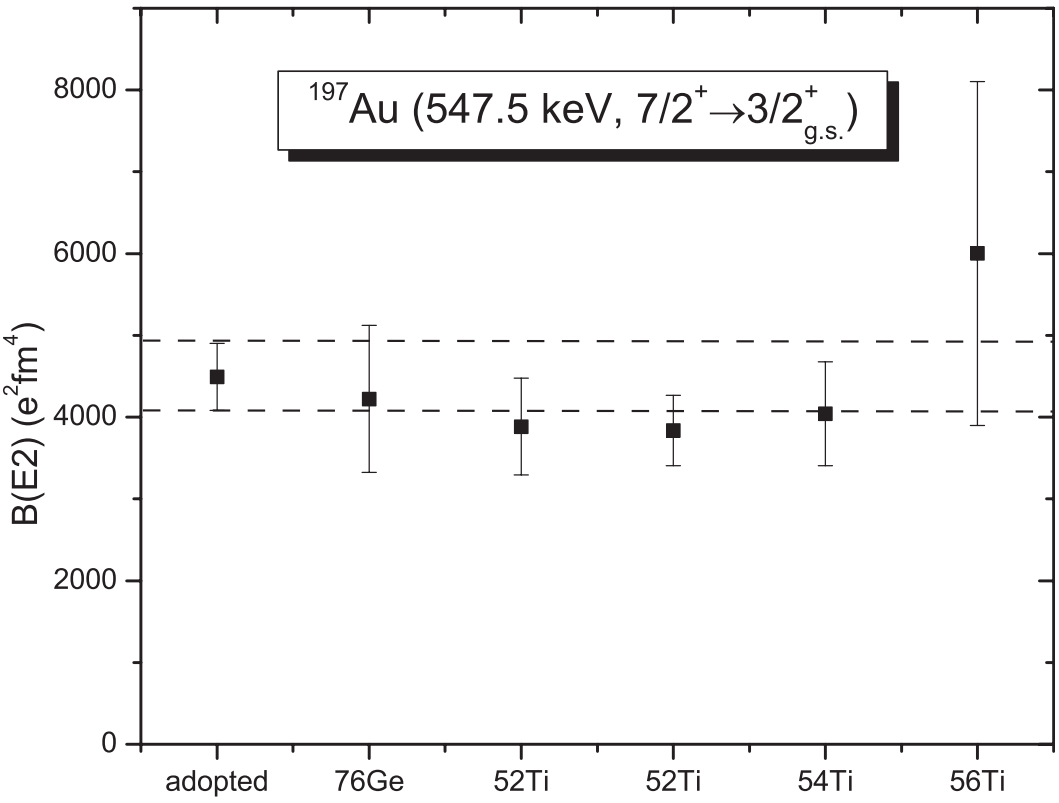

Figure 2.6: Measurement of the reduced transition probability from the ground state to the $7/2^+$ state in the Au target for all beams used in this experiment.

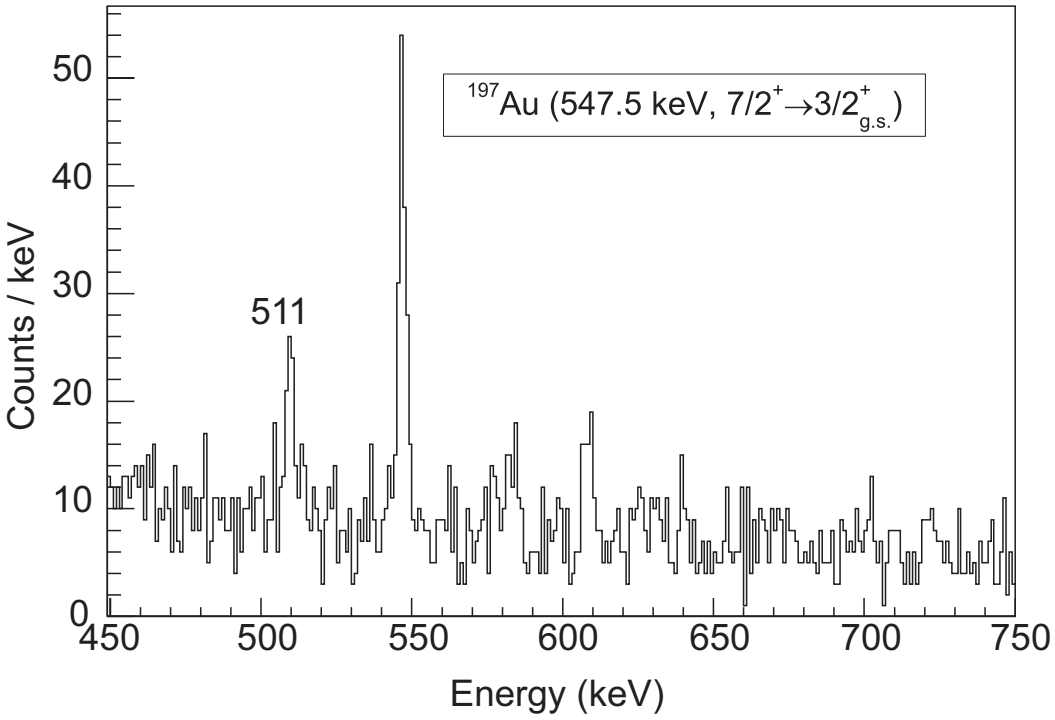

Figure 2.7: Laboratory frame coincidence γ-ray spectra for ^{197}Au. The nucleus is Coulomb excited by the electromagnetic field of the incoming ^{54}Ti beam.

Background subtraction is employed in this type of experiment when the hardware time gates of the data acquisition triggering system have to be wide and permit a large number of events that are uncorrelated with the reaction of interest to be recorded. Another situation in which the background subtraction is used is when the counts from background lines (e.g. ^{40}K from the environment, ^{60}Co from activated pieces of beam pipe) are repositioned in the reconstructed projectile frame energy spectrum by Doppler correction in the same region as the in-beam peaks of interest. A software "prompt time" gate is defined around the prompt time peak of each germanium detector time spectrum (see Figure 2.9). A logic "OR" gate is defined for the prompt time peaks of all the SeGA detectors. The same procedure is applied for a gate with the same time duration (width), placed after the prompt time peak. When using the background subtraction method, the data are scanned first requiring a logic "AND" of the software particle identification gate and the prompt time of SeGA. Then data are scanned with a logic "AND" condition for the particle identification gate and the off-prompt SeGA time. The resulting γ-ray spectrum is subtracted from the spectrum obtained for the prompt time. The result is a background subtracted spectrum. As an illustration of the results, a background subtracted spectrum for ^{197}Au is displayed in Figure 2.8. Compared to the Figure 2.7 the background around the ^{197}Au peak is more flat (e.g. the 511 keV line disappeared).

Figures 2.10, 2.11, 2.12, and 2.13 show representative coincidence γ-ray spectra for ^{76}Ge and the even $^{52-56}$Ti isotopes Doppler reconstructed event-by-event in the projectile frame. The energy at mid-target for ^{76}Ge was 73.5 MeV/nucleon, and the minimum impact parameter 17.6 fm as deduced from the maximum scattering angle in the center-of-mass frame of projectile and target, $\theta_{cm} < 3.1^{\circ}$. For ^{52}Ti the corresponding values for the 256 mg/cm^2 and 518 mg/cm^2 Au targets were 82.4 and 79.1 MeV/nucleon, respectively, with $\theta_{cm} < 3.1^{\circ}$ and $< 3.3^{\circ}$ and similar minimum impact parameter of 13.9 fm. The spectrum measured with the thinner target is shown in the Figure 2.11. For ^{54}Ti and ^{56}Ti, the respective projectile energies were 83.3

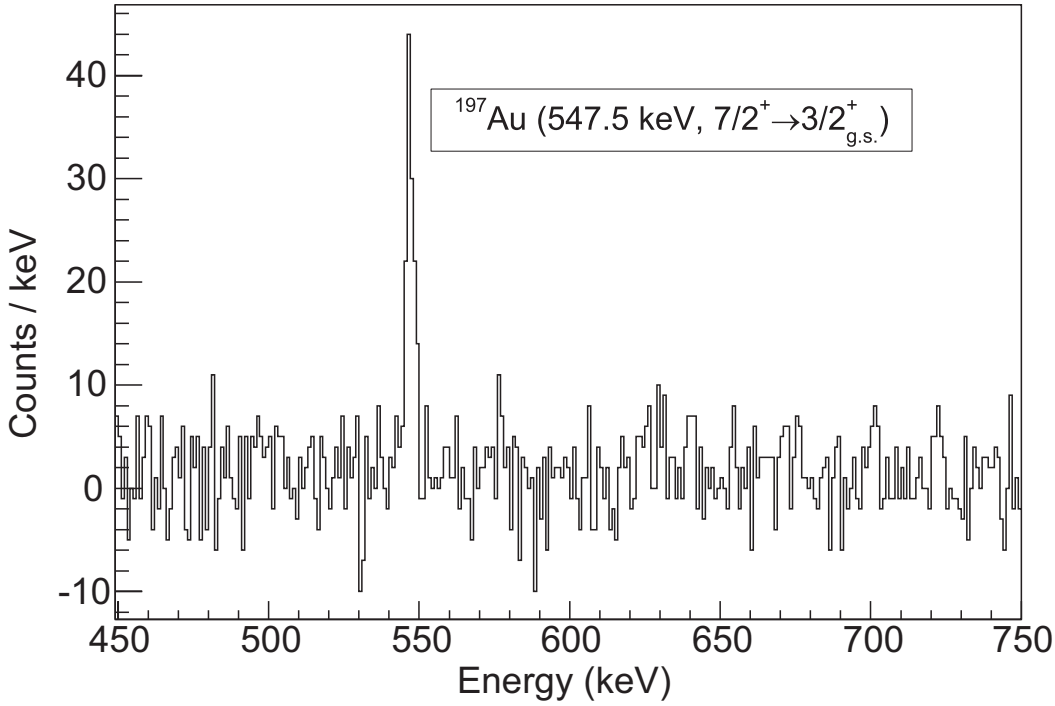

Figure 2.8: Laboratory frame γ-ray spectra for ^{197}Au in coincidence with ^{54}Ti. Background subtraction applied.

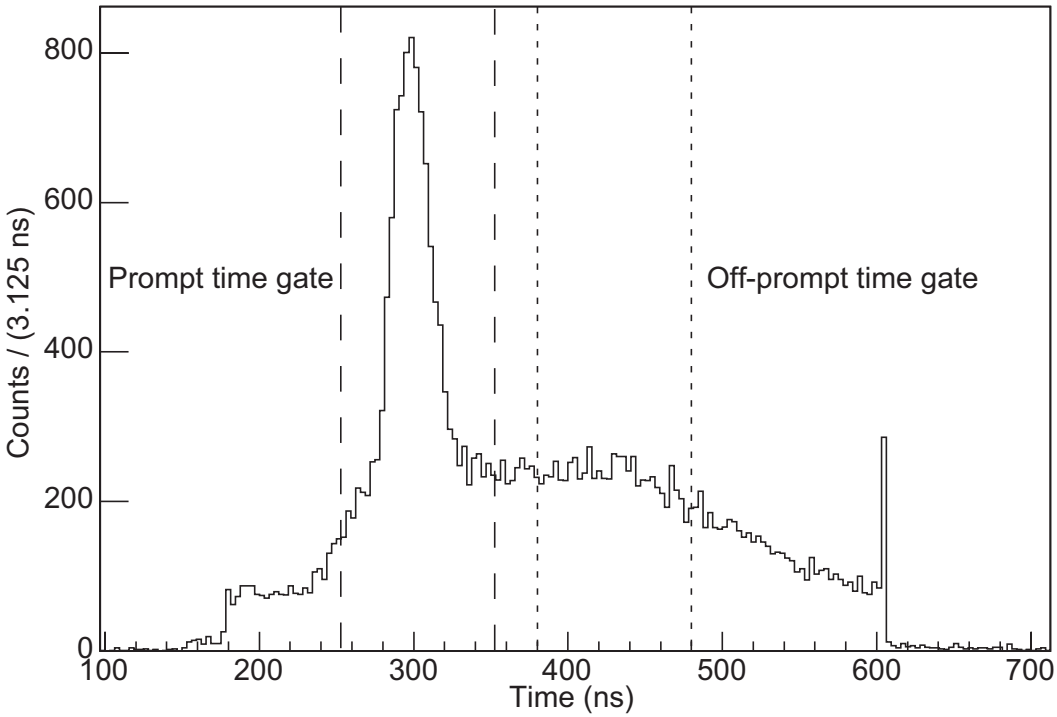

Figure 2.9: Typical time spectrum for a SeGA detector. Prompt time gate is depicted in dashed line. The off-prompt time gate, equal in width with the prompt time gate is in dotted line.

Table 2.2: Summary of scattering angle cuts. The first entry for ^{52}Ti corresponds to the 256 mg/cm^2 target and the second to the 518 mg/cm^2 target.

Beam	Minimum impact parameter (fm)	Center-of-mass angle (°)	Laboratory-frame angle (°)
^{76}Ge	17.6	3.06	2.18
^{52}Ti	13.9	3.10	2.42
^{52}Ti	13.9	3.29	2.57
^{54}Ti	14.0	3.20	2.48
^{56}Ti	14.1	3.58	2.75

Table 2.3: Summary of measured transition energies ($2_1^+ \rightarrow 0_{g.s.}^+$), number of particles detected and Coulomb excitation cross sections.

Beam	Energy $2_1^+ \rightarrow 0_{g.s.}^+$ (keV)	Particles detected	Cross section (mb)	Target thickness (mg/cm^2)
^{76}Ge	562.6(6)	26×10^6	394(47)	256
^{52}Ti	1050(2)	130×10^6	119(16)	256
^{52}Ti	1049(2)	67×10^6	125(16)	518
^{54}Ti	1497(4)	92×10^6	83(15)	256
^{56}Ti	1123(7)	6×10^6	155(51)	518

and 78.6 MeV/nucleon, with minimum impact parameters of 14.0 fm and 14.1 fm computed from $\theta_{cm} < 3.2°$ and $< 3.6°$. The arrows indicate the expected location of transitions deexciting the 2_2^+ levels. A summary of minimum impact parameters and the center-of-mass and projectile frame maximum scattering angles is presented in the Table 2.2. Table 2.3 shows the measured transition energies ($2_1^+ \rightarrow 0_{g.s.}^+$) the number of particles detected (with down scaler correction) and Coulomb excitation cross sections measured for the angular ranges in Table 2.2.

For all settings in this experiment, projectile and laboratory frame, the areas of the peaks of interest were determined with and without background subtraction. In all situations no difference between the results with statistical significance was found. Figures 2.14, 2.15, 2.16, 2.17 show particle-γ coincidence spectra for Doppler corrected γ-ray energy with background subtraction applied.

With the reliability of the technique demonstrated, attention can now turn to the

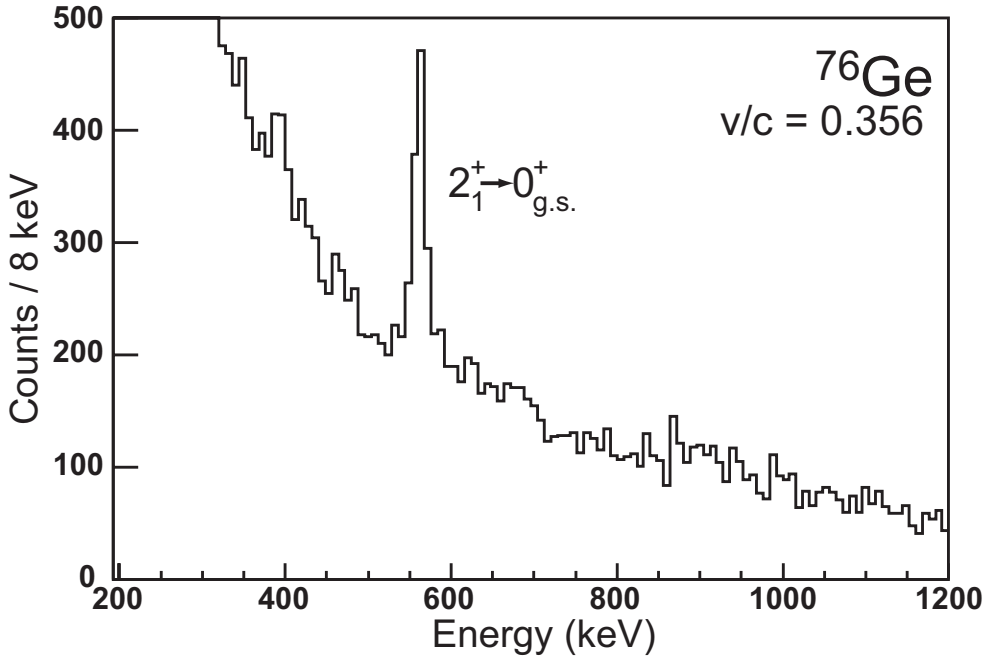

Figure 2.10: Coincidence γ-ray spectra for ^{76}Ge Doppler-reconstructed event-by-event in the projectile frame.

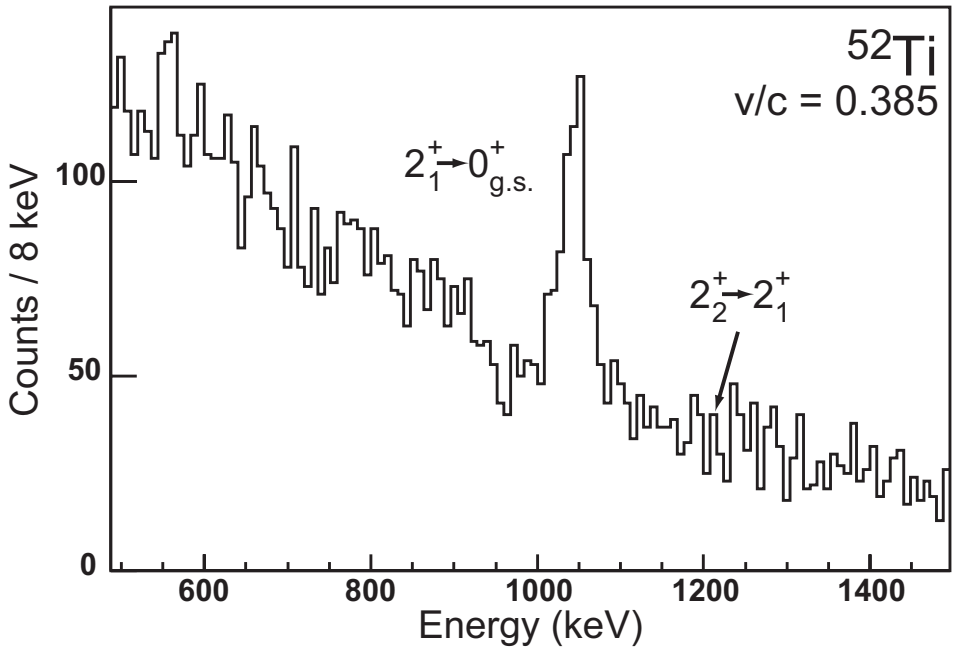

Figure 2.11: Coincidence γ-ray spectra for ^{52}Ti Doppler-reconstructed event-by-event in the projectile frame. The possible location of the $2_2^+ \rightarrow 2_1^+$ transition is shown by an arrow

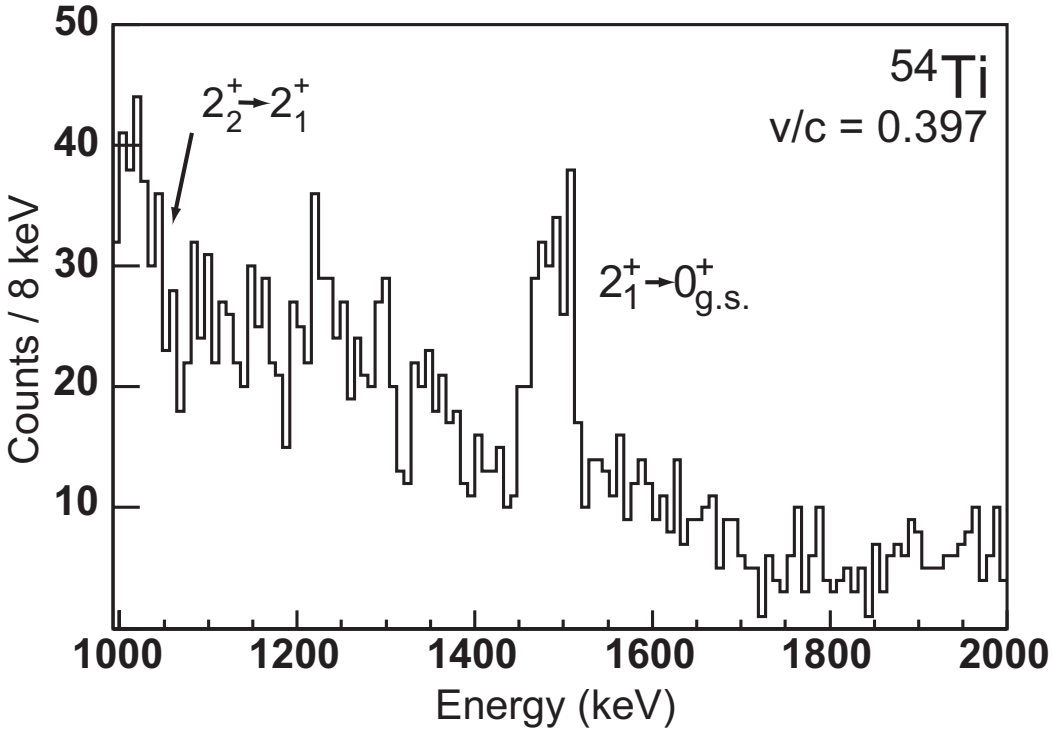

Figure 2.12: Coincidence γ-ray spectra for ^{54}Ti Doppler-reconstructed event-by-event in the projectile frame. The possible location of the $2_2^+ \rightarrow 2_1^+$ transition is shown by an arrow.

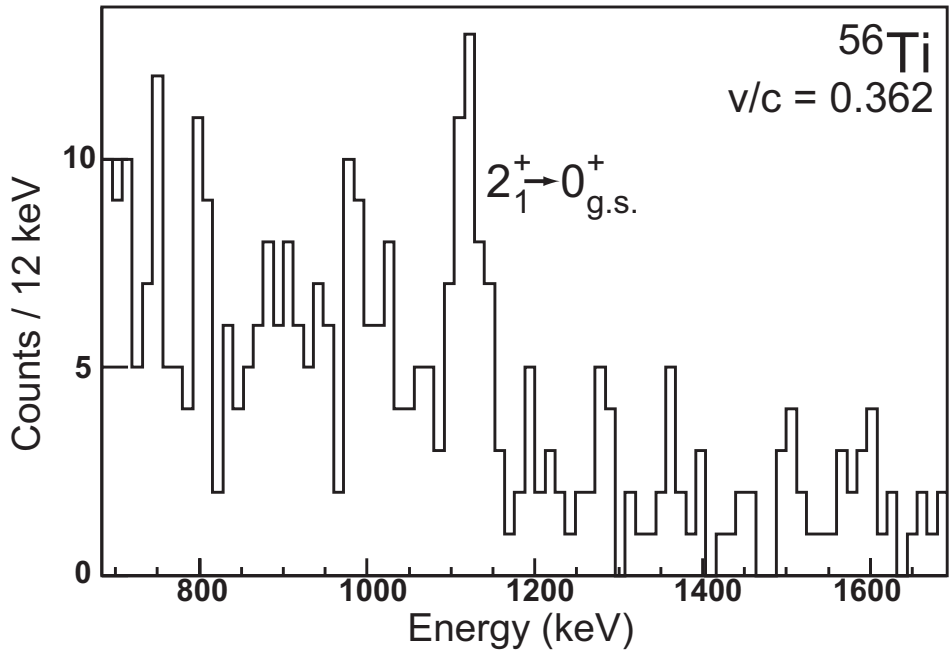

Figure 2.13: Coincidence γ-ray spectra for ^{56}Ti Doppler-reconstructed event-by-event in the projectile frame.

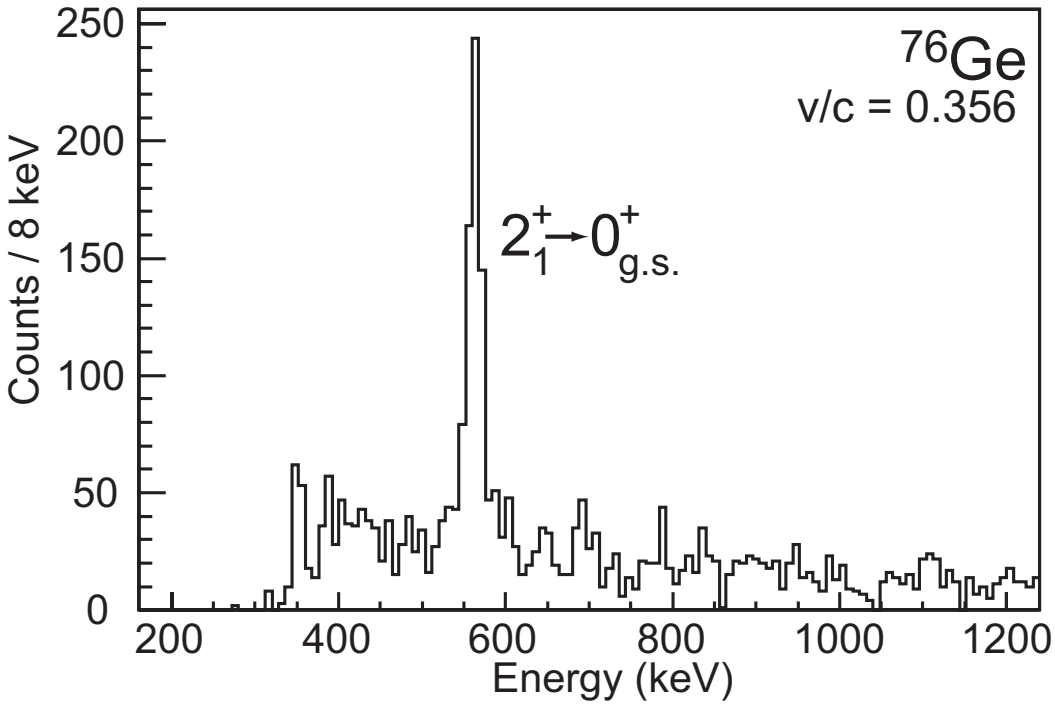

Figure 2.14: Projectile frame γ-ray energy in coincidence with ^{76}Ge. Background subtraction applied.

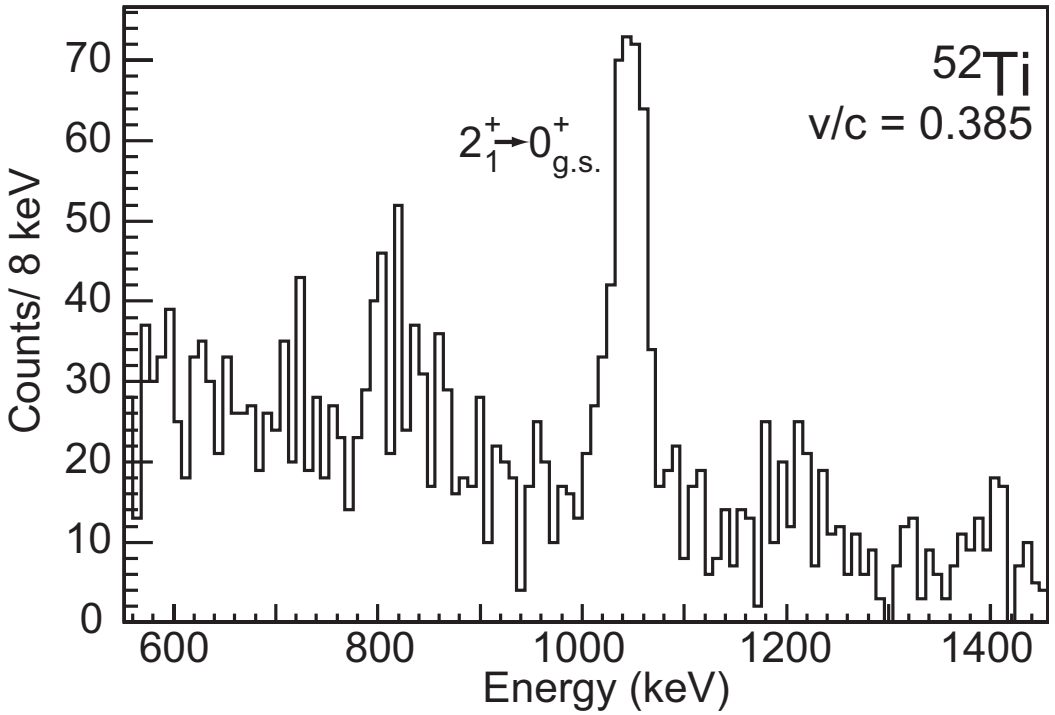

Figure 2.15: Projectile frame γ-ray energy in coincidence with ^{52}Ti. Background subtraction applied.

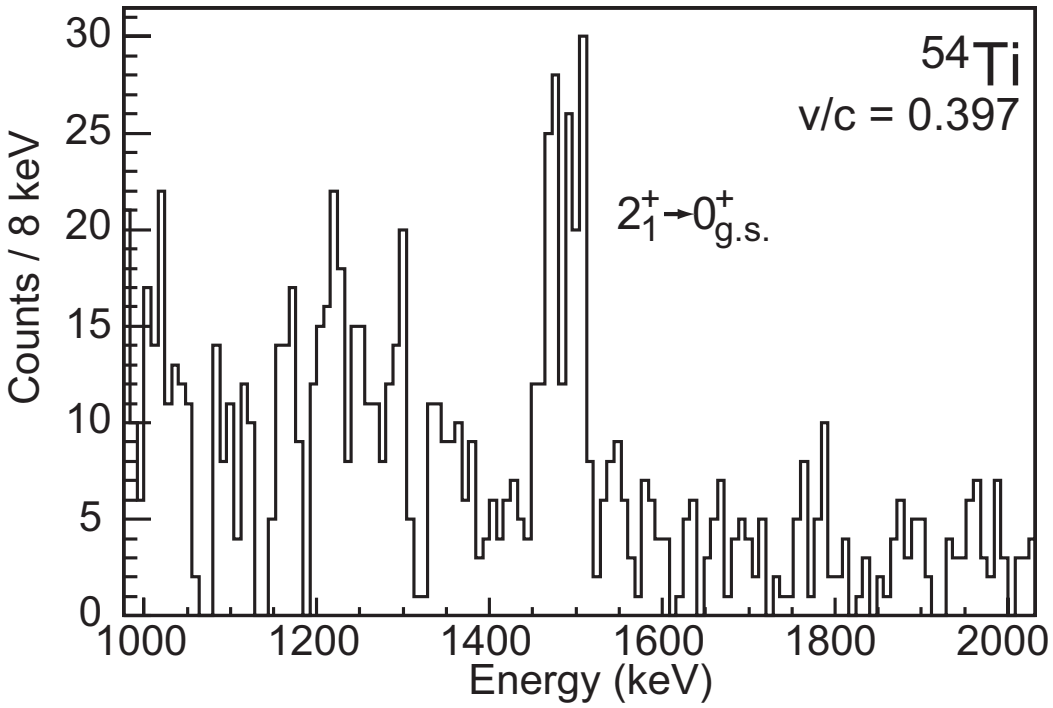

Figure 2.16: Projectile frame γ-ray energy in coincidence with ^{54}Ti. Background subtraction applied.

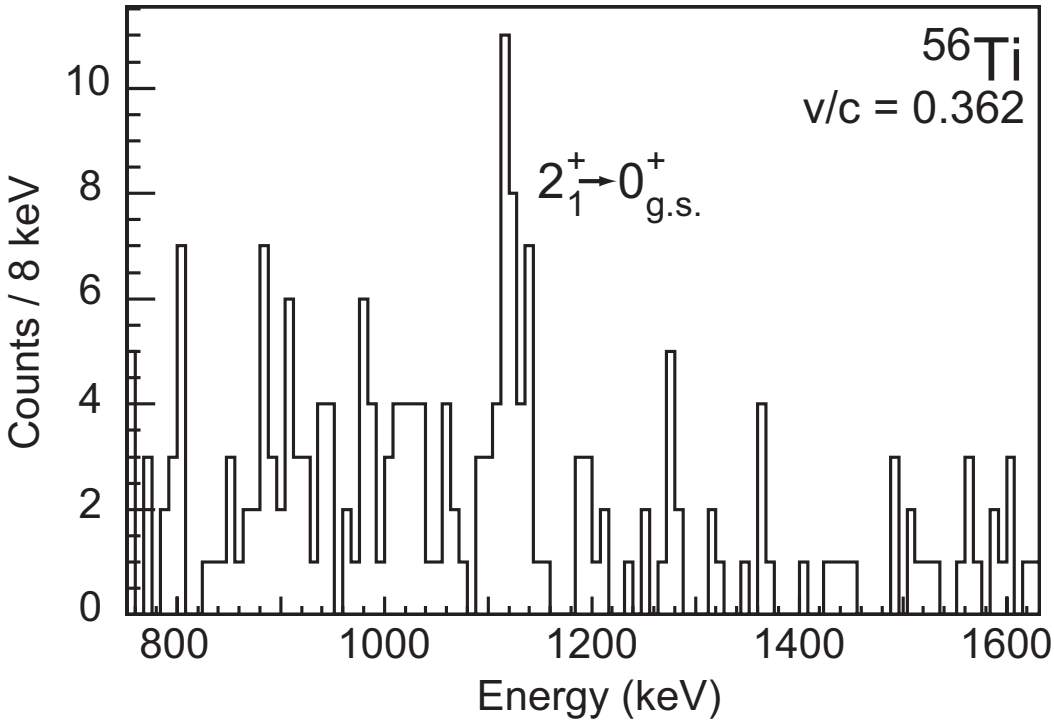

Figure 2.17: Projectile frame γ-ray energy in coincidence with ^{56}Ti. Background subtraction applied.

Table 2.4: Comparison of measured $B(E2;0^+ \rightarrow 2_1^+)$ values (labeled $B(E2;\uparrow)$ in the table) with shell model calculations using the GXPF1 interaction as well as the recently proposed GXPF1A interaction. The two ^{52}Ti entries correspond to separate measurements with Au targets of different thicknesses; (a) 256 mg/cm^2, (b) 518 mg/cm^2 and (c) the weighted average of the two. Data on the excitation of the Au target by the various Ti isotopes are given as well.

Nucleus	$B(E2;\uparrow)$ (e^2fm^4) expt.	$B(E2;\uparrow)$ (e^2fm^4) GXPF1	$B(E2;\uparrow)$ (e^2fm^4) GXPF1A	$B(E2;\uparrow)$ (e^2fm^4) 547 keV Au
^{52}Ti $^{(a)}$	593(80)	427	435	4114(627)
^{52}Ti $^{(b)}$	548(70)	427	435	4063(455)
^{52}Ti $^{(c)}$	567(51)	427	435	
^{54}Ti	357(63)	453	446	4279(672)
^{56}Ti	599(197)	483	448	6356(2227)

three even-mass Ti isotopes of interest. The analysis was carried out following the prescription given above for ^{76}Ge. In each case, the cross section for the excitation of the first 2^+ level was extracted from the γ-ray yields measured in spectra corrected for the Doppler shift and the response of the SeGA detectors (representative spectra are shown in Figures 2.10, 2.11, 2.12, 2.13), with appropriate restrictions on the scattering angle of the Ti fragments (see discussion above and Ref. [27]). Table 2.4 presents the derived $B(E2;0^+ \rightarrow 2_1^+)$ values. In the case of ^{52}Ti, measurements were carried out with two targets of different thickness in order to ensure the validity of the experimental approach when thicker targets are required to compensate for lower fragment yields, as is the case here for ^{56}Ti. The two ^{52}Ti data points are in excellent agreement (Table 2.4). Furthermore, they also agree with an earlier measurement [50], though the errors are large: $B(E2;0^+ \rightarrow 2_1^+) = 665^{+515}_{-415}$ e^2fm^4. Additional confidence in the transition rates of Table 2.4 comes from the data gathered simultaneously for Coulomb excitation of the target: the $B(E2;3/2^+ \rightarrow 7/2^+)$ values for the excitation of ^{197}Au agree with each other and with the adopted value [49] (see Table 2.4).

The values in Table 2.4 assume that the excitation of the 2_1^+ levels of interest occurs in a one-step, direct process without significant contribution(s) from higher-

lying 2^+ states to the measured $2_1^+ \rightarrow 0^+$ γ-ray yields. In ^{52}Ti, a number such higher 2^+ states are known [51], and a 2_2^+ level has also been proposed tentatively in ^{54}Ti [13]. In the data for both nuclei, none of the γ rays associated with decays from these levels towards the ground state and the yrast 2_1^+ level was observed, as illustrated in Figures 2.11 and 2.12 where the location of the $2_2^+ \rightarrow 2_1^+$ transitions in ^{52,54}Ti is given with arrows. The absence of peaks indicates that any feeding correction must be small. Furthermore, as discussed below, these excited levels are understood in the context of the shell model and the associated reduced transition probabilities are calculated to be smaller by an order of magnitude or more than the $B(E2; 0^+ \rightarrow 2_1^+)$ values under discussion here. The largest such strengths is predicted to occur for the 2_2^+ level in ^{52}Ti. In this case, the upper limit for the $2_2^+ \rightarrow 2_1^+$ intensity obtained from the data translates into a maximum correction to the $B(E2; 0^+ \rightarrow 2_1^+)$ value of 34 e^2fm^4, *i.e.*, well within the error bars of Table 2.4. In all other cases the contributions from higher 2^+ levels would be even smaller and it is concluded that possible feeding corrections do not affect the values of Table 2.4 significantly.

2.5 Discussion

Experimental evidence for a shell closure is usually inferred from at least two observables derived from nuclear spectra: the energy of the first excited state and the reduced transition probability to the same level. The former is expected to be rather large, reflecting the sizable energy gap associated with a shell or sub-shell closure, and the latter is anticipated to be small and comparable to single-particle estimates. Figures 2.18 and 2.19 present the two physical quantities of interest for all even Ti isotopes with mass $A = 48$ to $A = 56$. From the figure, a clear anti-correlation between the two observables can be readily seen: while the $E(2_1^+)$ energies increase significantly at $N = 28$ and $N = 32$ (Figure 2.18), the $B(E2; \uparrow)$ strengths are lowest for these two neutron numbers (Figure 2.19). Furthermore, both these physical quantities also

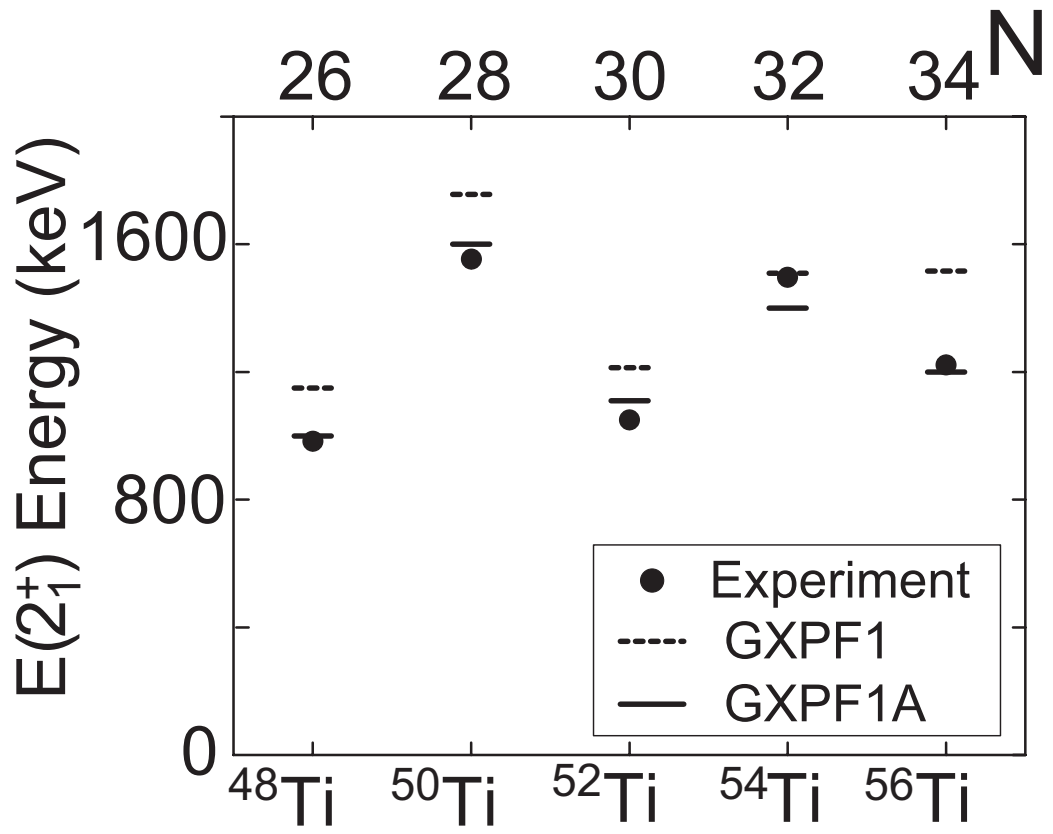

Figure 2.18: Comparison of the measured 2_1^+ excitation energies with the results of large-scale shell model calculations using the GXPF1 (dashed lines) and GXPF1A (solid lines) effective interactions.

differ markedly from the corresponding values at neutron numbers $N = 26, 30$ and 34. For ^{50}Ti, the well known shell closure at $N = 28$ translates into a small transition probability: with the $B(E2)$ value of Figure 2.19, the deexcitation from the 2_1^+ level to the ground state has a strength of only 5.6 single-particle units.

The fact that the excitation energy and the reduced transition probability observed in ^{54}Ti are comparable to those in ^{50}Ti (see Figure 2.19 and Table 2.4) then suggests that the Ti isotope with $N = 32$ is as good a semi-magic nucleus as its $N = 28$ counterpart and, hence, that a substantial sub-shell gap must occur at $N = 32$. Conversely, the fact that the three other Ti isotopes have 2_1^+ excitation energies lower by several hundreds of keV and $B(E2; 0^+ \rightarrow 2_1^+)$ values higher by a factor of ~ 2 can be interpreted as an experimental indication for the absence of sub-shell gaps in the

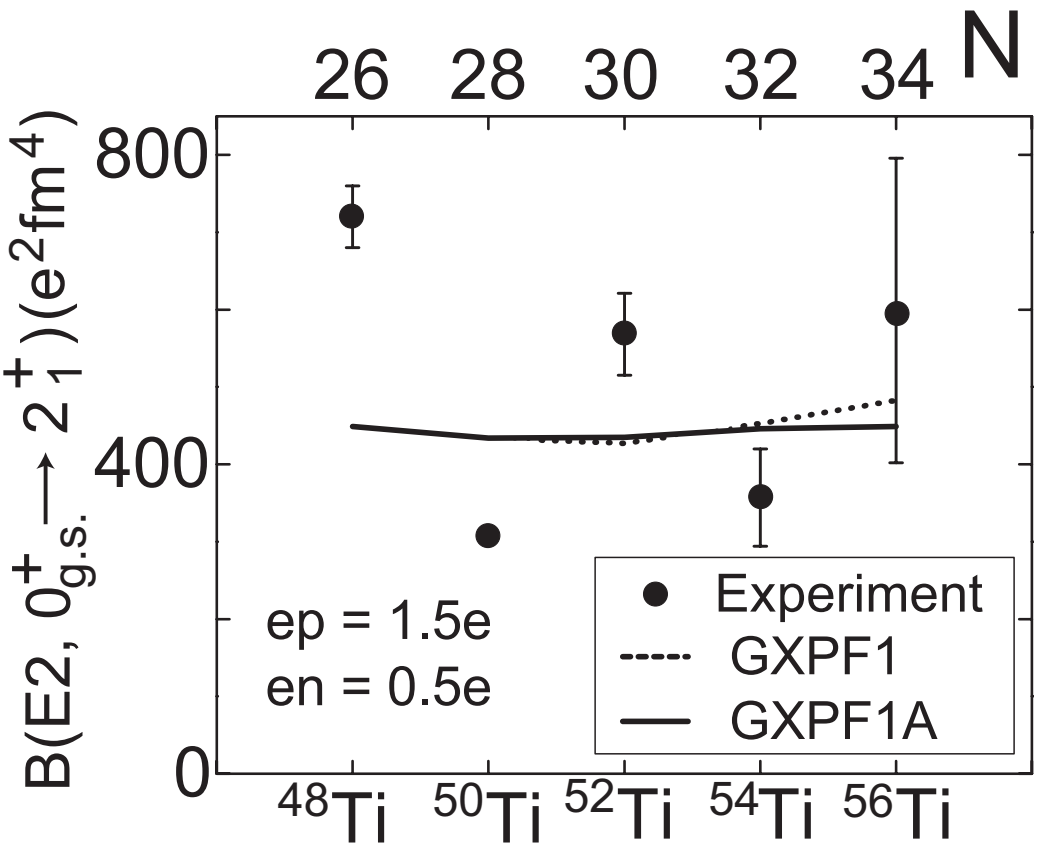

Figure 2.19: Comparison of the measured absolute $B(E2; 0^+ \rightarrow 2_1^+)$ transition strengths with the results of large-scale shell model calculations using the GXPF1 (dashed lines) and GXPF1A (solid lines) effective interactions. The $B(E2; 0^+ \rightarrow 2_1^+)$ value for ^{52}Ti is the weighted average of the two measurements given in Table 2.4.

neutron single-particle spectrum at $N = 26, 30$ and 34.

Diagonalization of Hamiltonian matrices when the full valence-nucleon space is considered is difficult due to limitation in computing power. For the pf-shell, an effective interaction, GXPF1 [10], was proposed, based on microscopic effective interaction [52] based on the Bonn-C potential.

Large-scale shell model calculations with the GXPF1 effective interaction, optimized for the description of pf-shell nuclei [10], attribute the onset of a $N = 32$ gap in neutron-rich Ca, Ti and Cr nuclei to the combined actions of the $2p_{1/2} - 2p_{3/2}$ spin-orbit splitting and the weakening of the monopole interaction strength between $f_{7/2}$ protons and $f_{5/2}$ neutrons. The dashed lines in Figure 2.18 represent the results of calculations with this interaction: while the $N = 32$ gap in the Ti isotopes is accounted for, the calculations also predict an additional gap at $N = 34$ that is not borne out by experiment. As pointed out in References [11, 14], the data suggest instead that the energy spacings between the $p_{3/2}$, $p_{1/2}$ and $f_{5/2}$ neutron orbitals, as well as the degree of admixture between these states in the wavefunctions of the ^{56}Ti yrast excitations, require further theoretical investigation. This has been done recently by Honma *et al.* [53] with the introduction of a modified version of the interaction, labeled GXPF1A, in which the matrix elements of the interaction involving mostly the $p_{1/2}$ orbital have been readjusted. It is worth pointing out that the evaluation of the properties of this orbital from experimental data is particularly challenging since it contributes little angular momentum to any given state. Traces of its impact are often obscured as a result. The solid lines in Figure 2.18 indicate that the GXPF1A calculations reproduce the $E(2_1^+)$ energies. In fact, they provide a satisfactory description of all the known levels in the even Ti nuclei, including those above the 6^+ level in ^{54}Ti which involve neutron excitations across the $N = 32$ shell gap [53]. They also describe the odd Ti nuclei satisfactorily [54].

Shell-model predictions of the reduced transition matrix elements were calculated

using

$$B(E2\uparrow) = \frac{(e_p A_p + e_n A_n)^2}{2J_i + 1}, \tag{2.15}$$

where A_p and A_n are the E2 matrix elements calculated in the model space matrix of the proton and neutron. e_p and e_n are the total effective charges of the proton and neutron [55]. The choice of effective charge values for protons and neutrons is related to the core polarization models [56]. The effective charges account for average effects of the renormalization from wavefunction admixtures outside the model space and center-of-mass corrections. J_i is the spin of the initial state, 0 in the case of the ground states of ^{52,54,56}Ti. The MSHELL code [57] was used to carry out the computations.

For all the even Ti isotopes, the wavefunctions of the 2^+ levels are dominated by $(f_{7/2})^2$ proton configurations coupled to ground and excited states of the neutron configurations. This is reflected in the proton and neutron amplitudes A_p and A_n from which the $E2$ matrix elements are computed (see below). For the GXPF1 interaction, these (A_p, A_n) amplitudes, in units of $e\text{fm}^2$, have respective values of (8.8,15.4), (10.7,9.5), (9.0,14.4), (10.7,10.6), and (11.8,8.7) for the even $^{48-56}$Ti. The theoretical shell gaps for neutrons at $N = 28, 32$ and 34 result in reduced A_n amplitudes and in excitation spectra for ^{50,54,56}Ti that most closely reflect the $(f_{7/2})^2$ proton structure. The deviation of the experimental ^{56}Ti spectrum from theory indicates a weaker shell gap at $N = 34$. As stated above, the new GXPF1A interaction [53] improves the agreement, and the new amplitudes $(A_p, A_n) = (10.3,11.4)$ reflect a larger neutron admixture. With this interaction, the calculated $p_{1/2} - f_{5/2}$ shell gap at $N = 34$ is still significant, i.e., 2.5 MeV. Furthermore, this gap is calculated to increase to 3.5 MeV for ^{54}Ca [53], so that a neutron sub-shell closure is still predicted in this case. The $B(E2,\uparrow)$ rates computed from the (A_p, A_n) values (Equation 2.15) with conventional effective charges of $e_p = 1.5e$ and $e_n = 0.5e$ overestimate the measured transition rates for the $N = 28$ and 32 nuclei (Table 2.4, Figure 2.19). Moreover, they

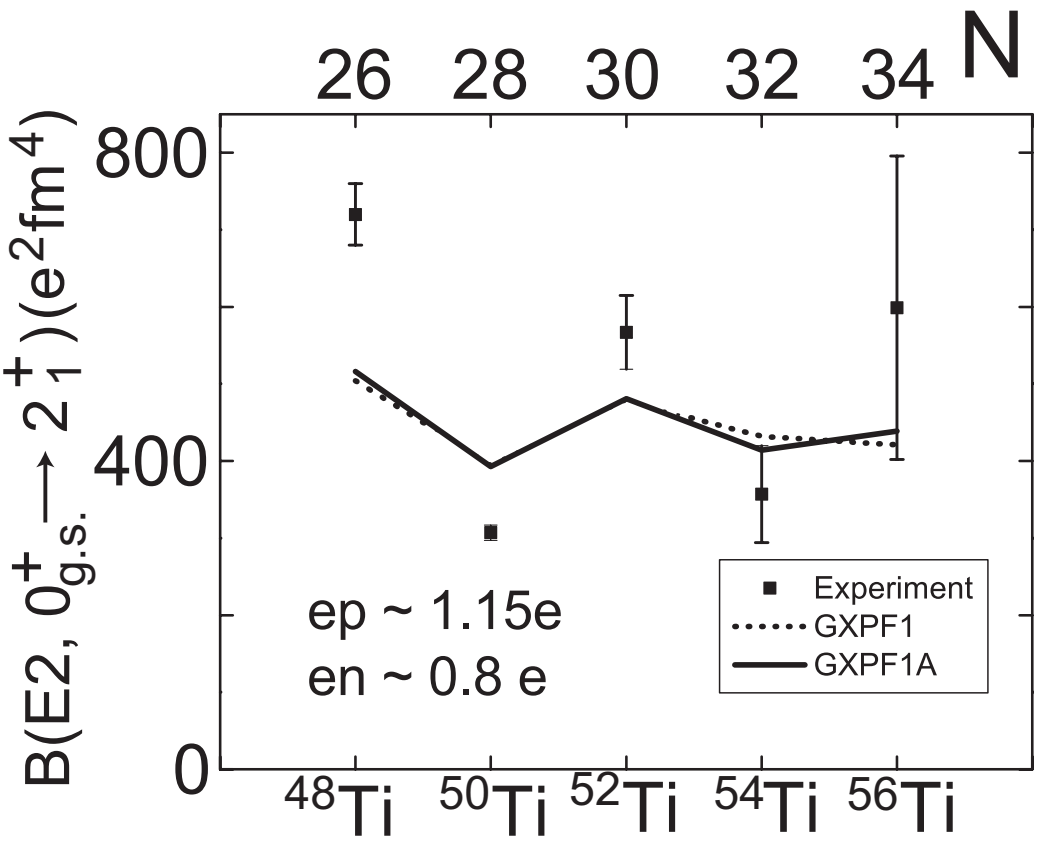

Figure 2.20: Comparison of the measured absolute $B(E2; 0^+ \rightarrow 2_1^+)$ transition strengths with the results of large-scale shell model calculations using the GXPF1 and GXPF1A effective interactions using the effective charges calculated from Ref. [1].

are rather constant as a function of neutron number, in contrast with the oscillating behavior observed in the experiment. An oscillation related to the neutron shell gaps is present in the A_n amplitudes. It is possible that, for neutron-rich nuclei, the neutron e_n effective charge needs to be increased, while keeping the isoscalar effective charge $e_p + e_n$ constant. Such a modification in the e_p and e_n charges could result in a better agreement with experiment. Recent data [1] on analogue states in $A = 51, T_z = \pm 1/2$ mirror nuclei suggest that this may well be the case and values of $e_p \sim 1.15e$ and $e_n \sim 0.8e$ were proposed. While these values would induce a small staggering in the calculated $B(E2)$ values (see Figure 2.20), they are not sufficient to bring experiment and theory in agreement. Additional data on pf-shell nuclei are needed to investigate this issue further.

In summary, the present data on absolute $E2$ transition rates, together with earlier work on excitation energies, confirm the presence of a sub-shell closure at neutron number $N = 32$ in neutron-rich Ti nuclei above ^{48}Ca, an observation in agreement with the results of shell model calculations with the most recent effective interactions. However, the data do not provide any direct indication of the presence of an additional $N = 34$ sub-shell gap in the Ti isotopes. Moreover, the measured $B(E2; 0^+ \rightarrow 2_1^+)$ probabilities highlight the limitations of the present large-scale calculations as they are unable to reproduce in detail the magnitude of the transition rates in the semi-magic nuclei and their strong variation across the chain of neutron-rich Ti isotopes.

Chapter 3

Sub-segment interaction position resolution for the NSCL SeGA detectors

3.1 Physics with fast exotic beams at the NSCL

The National Superconducting Cyclotron Laboratory (NSCL) at Michigan State University has designed and purchased an array of eighteen 32-fold segmented high-purity germanium (HPGe) detectors [44]. The Segmented Germanium Array (SeGA) was optimized for nuclear spectroscopy of fast exotic beams produced by projectile fragmentation. Since its commissioning in 2001 the types of experiments in which SeGA played a central role ranged fromγ-ray spectroscopy following β-decay [58, 59] and transfer reactions to Coulomb excitation [27, 32], inelastic proton scattering [60, 61], one- or two-nucleon knockout or fragmentation [62, 63]. Despite the broad range of reaction types studied, all experiments except β-decay measurements share common characteristics. The nuclei that compose the secondary beams delivered to the experimental stations have velocities in the 0.15c - 0.65c range at the γ-ray emission time. For most experiments the detector multiplicity is one with the highest proba-

bility, meaning that the array will have on average about one detector triggering for a given event. Gamma-ray multiplicity per detector is also mostly 1 (a detector is hit by a single γ-ray), and there is no need to disentangle the signals from two or more photons. The triggered count rate is usually lower than 1 kHz. This affects the cost of the digital data acquisition system because some of the digital signal processing (DSP) features can be implemented in software in commercial off-the-shelf computers and components. SeGA is used in conjunction with an ancillary particle detector that triggers the data acquisition (e.g. NSCL's S800 spectrograph). In addition to reducing the trigger rate in the γ spectroscopic system, ancillary detectors also provide information about the incoming and outgoing beam (direction, velocity, isotope identification). SeGA is not designed to be used as a Compton camera. Photons come mostly from the target or from room background. Logic "AND" trigger conditions with the particle detectors reduce the room background random coincidences to a manageable level. Also, various particle tracking detectors can be used to estimate the γ-ray emission point. Due to the relativistic velocities at which the nuclei travel, the emitted γ-rays are Doppler shifted in the laboratory frame where the measurement is performed. Gamma-rays detected in the laboratory frame at forward angles have energies higher than in the center-of-mass, while those detected at backward angles have energies lower than in the center of mass. The energy in the center-of-mass frame is the one characteristic of the nuclear transition, and it must be Doppler reconstructed from the energy measured in the laboratory frame. The Doppler corrected energy depends on the measured γ-ray energy in the laboratory frame, the velocity of the beam, and emission angle with respect to the velocity of the beam (see Equation 1.1). The angle between the projectile velocity and the γ-ray emission direction is determined if the emission point, the velocity vector of the nucleus, and the first interaction point with the detector are known. The source of γ-rays of interest is known as the target is usually placed in the center of the array. The emission point can be estimated using the particle detectors placed before and after the secondary target.

The lifetimes of the excited states are usually very small. Typically the γ-ray emission occurs while the nucleus is still inside the target. The determination of the first interaction point with the detector depends on the characteristics of the given γ-ray spectroscopy system. For a given energy and orientation of the crystals the efficiency of the system is proportional to the inverse square of the average distance between detectors and target. The energy resolution describes how well two energy peaks can be separated and determines how large the peak-to-background ratio is. It depends on the intrinsic resolution of the detector (crystal plus accompanying electronics), the uncertainty in the beam velocity and the opening angle of the detector. It is given by the relationship:

$$\left(\frac{\Delta E_\gamma}{E_\gamma}\right)^2 = \left(\frac{\beta \sin\theta}{1-\beta\cos\theta}\right)^2 (\Delta\theta)^2 + \left(\frac{-\beta+\cos\theta}{(1-\beta^2)(1-\beta\cos\theta)}\right)^2 (\Delta\beta)^2 + \left(\frac{\Delta E_{\text{int}}}{E_\gamma}\right)^2. \tag{3.1}$$

where β is the velocity of the nucleus that emitted the γ-ray at the time when the nuclear transition occurred, θ is the emission angle with respect to the velocity of the beam and E_γ is the γ-ray energy. In a first approximation, the uncertainty in the determination of the target position is neglected. The intrinsic contribution ΔE_{int} is not strongly dependent on energy. The uncertainty in the beam velocity is due to the fact that, if the de-excitation takes place inside the target, the velocity of the beam at that point is not known. The $\Delta\beta$ term depends on the lifetime of the excited state and on the target thickness. The uncertainty in the opening angle of the detector is the angle subtended by the active volume of the detector that measured the γ-ray. By segmenting the outer contact of the detector in a number of slices and quadrants the interaction position can be determined with higher accuracy. The opening angle is reduced approximately linearly with the number of transverse segment groups.

Each of SeGAs 18 coaxial detectors is 32-fold electronically segmented in 8 longitudinal slices and 4 axial quadrants [44]. In the experiment setups the SeGA detectors are placed with their symmetry axes parallel to the beam axis to take advantage of

the 8 longitudinal segment groups for Doppler reconstruction. In the case of SeGA detectors, if the segment where the first interaction occurred could be established, the uncertainty in the opening angle would be the angle subtended by a single segment. Figure 3.1 shows the energy resolution dependency on the angle of the center of the detector with respect to the beam axis for a set of typical parameters, considering, for simplicity, the lifetime of the excited state to be zero. For the angles at which detectors can be physically placed, even if the uncertainty induced by the opening angle is reduced to zero, there will still be the uncertainty due the beam velocity that is dependent on the target characteristics and the lifetime of the excited state (considered zero in derivation of the Equation 3.1)

In the determination of the first interaction position, presently the segment with maximum energy deposited is selected. This simple algorithm gives satisfactory results because low-energy photons tend to deposit most of their energy in the first interaction and the photons with higher energy tend to scatter forward. The forward scattering does not change the primary γ-ray emission angle by a significant amount. Figure 3.2 shows an example of a γ-ray energy spectrum from the Coulomb excitation of ^{52}Ti on a ^{197}Au target, measured in the laboratory frame for the upper panel and Doppler reconstructed with the "hit on maximum" algorithm in the lower panel.

In the lab frame only the background lines are clearly visible. After Doppler correction the ^{52}Ti appears and the background lines are smeared out. Only the first interaction of the γ-ray with the detector is of importance for Doppler reconstruction. Neglecting the loss in energy resolution due to the finite lifetime of an excited state, the effective energy resolution obtained in experiments is lower than the theoretical prediction also because the segment with the highest energy deposited is not always where the γ-ray first interacted with the detector. These mispredictions lead to a degradation of the energy resolution for Doppler corrected spectra. There are several approaches to address this problem. The γ-ray tracking methods [29, 30] involve a very precise (down to 1-2 mm) determination of the interaction position.

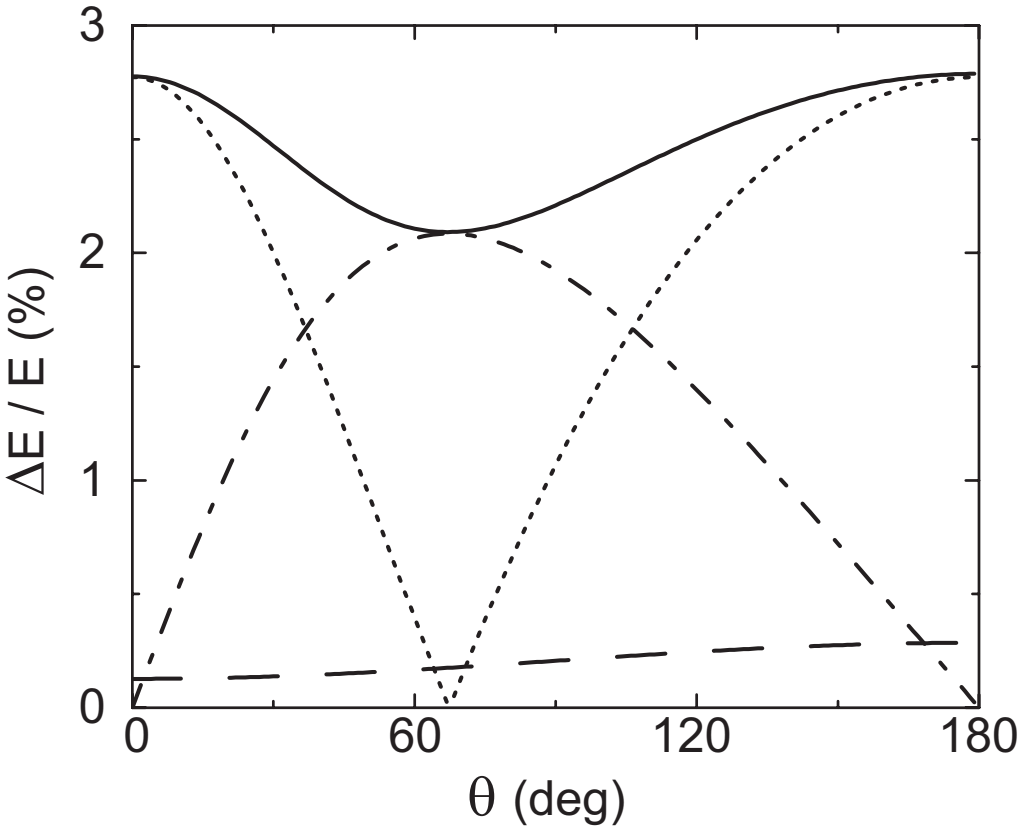

Figure 3.1: The energy resolution dependence with the detector angle for a ^{52}Ti beam with $\beta = 0.385$ and uncertainty $\Delta\beta = 0.024$. The energy of the γ-ray is considered $E_{CM} = 1.049$ MeV (projectile frame). The opening angle of the detector is considered $\Delta\theta = 3$ deg, corresponding to a SeGA detector places at 20 cm from target. The intrinsic constant is $\Delta E_{int} = 0.002$. The dotted line indicates the contribution from the beam velocity uncertainty. The dash-dot line corresponds to the contribution from the opening angle of the detector. The contribution of the intrinsic resolution is plotted in dashed line. The total energy resolution is plotted the continuous line. The conditions are typical for fast exotic beams physics at the NSCL.

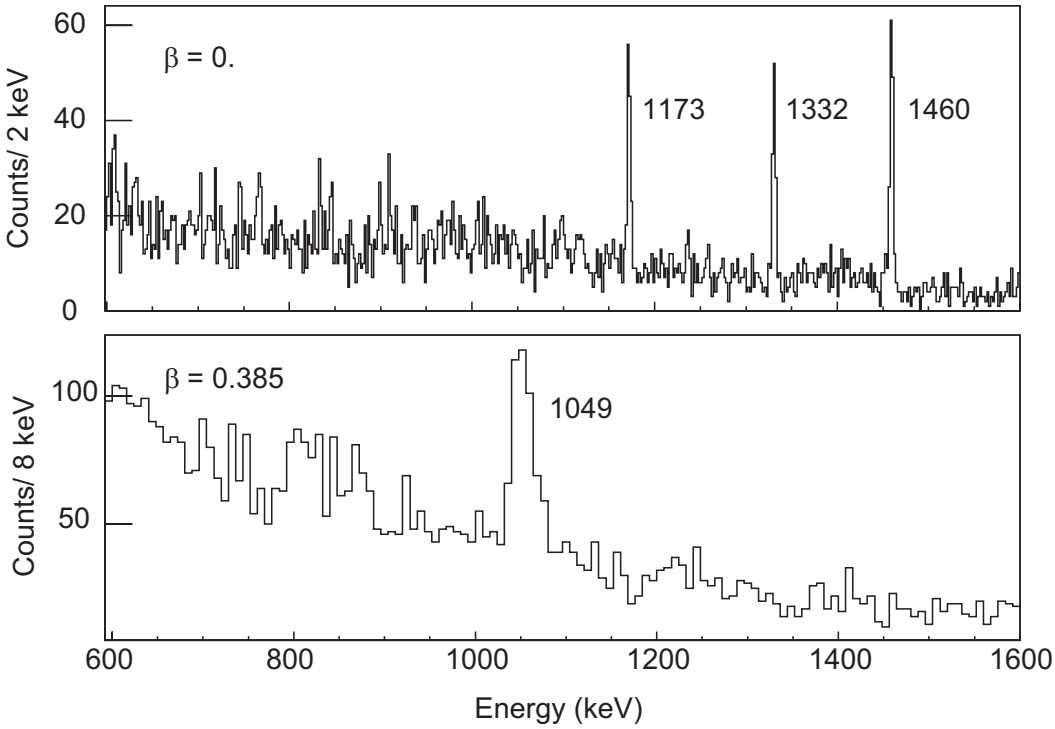

Figure 3.2: Laboratory frame (upper panel) and projectile frame (lower panel) γ-ray energy spectra. In the laboratory frame, the 1173 keV and 1332 keV lines correspond to the ^{60}Co decay and the 1460 keV line to the ^{40}K decay. In the projectile frame, the 1049 keV line corresponds to the ^{52}Ti $2_1^+ \rightarrow 0_{gs}^+$ transition.

With the interaction points and the energies deposited in each of them determined, the probability of each type of scattering history is calculated for every permutation of interaction points using the scattering angles from segment to segment and energies and a figure of merit is built. Based on the value of the figure of merit the most probable interaction path is determined. For Doppler reconstruction purposes the first interaction point in that path is considered. Another approach is to use an energy-weighted position. Instead of choosing one of the segment or sub-segment positions to be the first interaction, an average position based on physics considerations is chosen. In any of the above mentioned approaches, finer segmentation is needed to reduce the uncertainty in the scattering angles between the interaction points. One way to accomplish this is by using the properties of the signals formed in the semiconductor.

3.2 Signal formation in HPGe detectors

Semiconductor radiation detectors are the unquestionable favorites of the high-resolution γ-ray spectroscopy scientific community. Their energy resolution is unmatched by scintillators. In addition, semiconductor-based detectors have high efficiency, due to their large atomic number. For the energy range of interest, the photoelectric effect cross section is proportional to $Z^{3.5}$, the Compton effect to Z, and the pair production with Z^2. The high-purity germanium (HPGe), with the atomic number equal to 32 is the material of choice for high-resolution spectroscopy. Semiconductor materials investigated thus far that have a Z higher germanium (HgI_2, CdTe, GaAs) suffer from charge trapping problems that lead to incomplete charge collection, depending on the interaction position inside the crystal. Such problems make these materials unsuitable for most high-resolution applications. A further advantage of Ge is the maturity of the technology to grow, cut, implant and diffuse impurities in crystals. To some extent the crystals can be machined in different shapes and the impurity profile can be controlled. The NSCL SeGA detectors are close-ended, coaxial cylindrically sym-

metric. The impurity profile is of the n-type, meaning that the outer contact is a thin region implanted with boron atoms (50 μm) and the central contact region is lithium diffused (500 μm). The Boron is a substitution acceptor in germanium forming a p^+ region. On the central contact side, the lithium acts as a an interstitial donor atom in germanium forming an n^+ impurity region. The central contact is biased to a voltage varying from 4000 V to 5000 V depending on the detector (positive polarity). The signal from the inner contact is collected by an AC-coupled preamplifier and the signals from the outer segments are collected by a DC-coupled preamplifier, also connected to the ground. For more details see Reference [44].

A γ-ray photon with the energy in the range of interest for the experiments performed at the NSCL can interact with the germanium detector via four major processes: photoelectric effect, Compton effect, Rayleigh (coherent) scattering, and pair production. From several keV up to around 3 MeV, the photoelectric effect and the Compton scattering are the dominant interaction modes. The Rayleigh scattering is of importance for low energy photons and although the threshold is at 1.022 MeV, the pair production mechanism starts to play a role only for photon energies higher than 5 MeV. Viewed from the crystals point of view, an interaction with a photon produces an electron (for Compton scattering and photoelectric effect) or an electron and a positron in the case of a pair production event. For the photon energies of interest, the electron has an energy much larger than the other electrons bound in the crystal lattice. The primary electron interacts with the lattice via ionization (electron direct and indirect ionization) and non-ionization processes (phonon excitations). During the stopping process, the primary electron creates a large number of electron-hole pairs. The number of electron-hole pairs can be estimated from the average energy spent to move an electron from the valence band into the conduction band. This energy is 2.96 eV for Ge at 77 K. As an example, a 1 MeV photon that deposits all its energy in the crystal produces around 3.4 $\times 10^5$ electron-hole pairs. The 2.96 eV energy is larger than the Ge band gap at 77 K because some of the primary electron

energy is lost in the production of crystal lattice vibrations (phonons).

The ensemble of created electron-hole pairs is called the charge cloud. In normal conditions, the pairs recombine locally. In the case of the detector, the crystal is biased, and the charges start moving in opposite directions, depending on the sign of their charge. Electrons promoted into the conduction band and their vacancies left in the valence band (holes) move as independent charge carriers.

Signal formation at the electrodes is described by the Ramo-Shockley theorem via the weighting potential method [64, 65]. The weighting potential is not a real potential. It is a measure of the coupling between the charge carriers at the specified position in space and the sensing electrode. It can be calculated by solving Laplace's equation in the crystal volume for the sensing electrode placed at a potential of one volt and all the other electrodes grounded. After an interaction, the electrons and holes move in the real electric field of the detector, but the signals they produce at the collecting electrodes are determined by the weighting potential.

Briefly, this is the recipe on how the signal shapes can be calculated. If the properties of the crystal (shape, impurity profile, dielectric constant) and the voltage bias are known, the net space charge density ($\rho(r)$) can be calculated from the distribution of donor atoms ($N_d(r)$) via the relationship:

$$\rho(r) = eN_d(r) \tag{3.2}$$

where e is the electron charge. The electric potential ($\Phi(r)$) throughout the crystal can be obtained by solving the Poisson equation:

$$\nabla^2\Phi(r) = -\frac{\rho(r)}{\epsilon} \tag{3.3}$$

where ϵ is the dielectric constant of germanium. There are only a few trivial cases for which this equation can be solved analytically (see for example [66]). Most of the time a numerical solver is needed. The electric field inside the crystal is the gradient

of the electric potential.

$$E(r) = -\nabla\Phi(r) \tag{3.4}$$

The charge carrier drift velocity is then:

$$v_{drift,c}(r_c) = \mu_c E(r_c) \tag{3.5}$$

The subscript c stands for charge carrier, since the electron and hole mobilities (μ_e and μ_h) are different, depending on the effective mass of the carrier which in turn is a tensor whose components vary depending upon the crystal axes orientation. For a study concerning the anisotropy of the electron drift velocity in germanium crystals at high electric fields and low temperature and its influence on the charge collection process see Reference [67].

Net charges inside the crystal create image charges in the inner and outer electrodes. These image charges create the signals that are picked up by the preamplifiers. It is a common missconception that the charges collected at the electrodes create the signals. Instead, their image charges are the ones responsible for generating signals. The real charge collected is the integral of the image charge induced. According to the Ramo-Shockley theorem the current induced in the electrodes is:

$$i_c = q_c.\vec{v}_{drift,c}\vec{E}_w \tag{3.6}$$

where $\vec{E}_w$ is the weighting field calculated from the weighting potential.

For a SeGA detector, the labeling scheme of the segments is the one provided in Figure 3.3.

Two cross sections of the weighting potential for segment E are plotted in Figures 3.4 and 3.6. Figure 3.4 shows a cross section of the weighting potential for segment E, 2 mm above the separation plane between the segments E and D. Let's assume that two charge carriers are moving on the paths "1" and "2". The charge moving on the

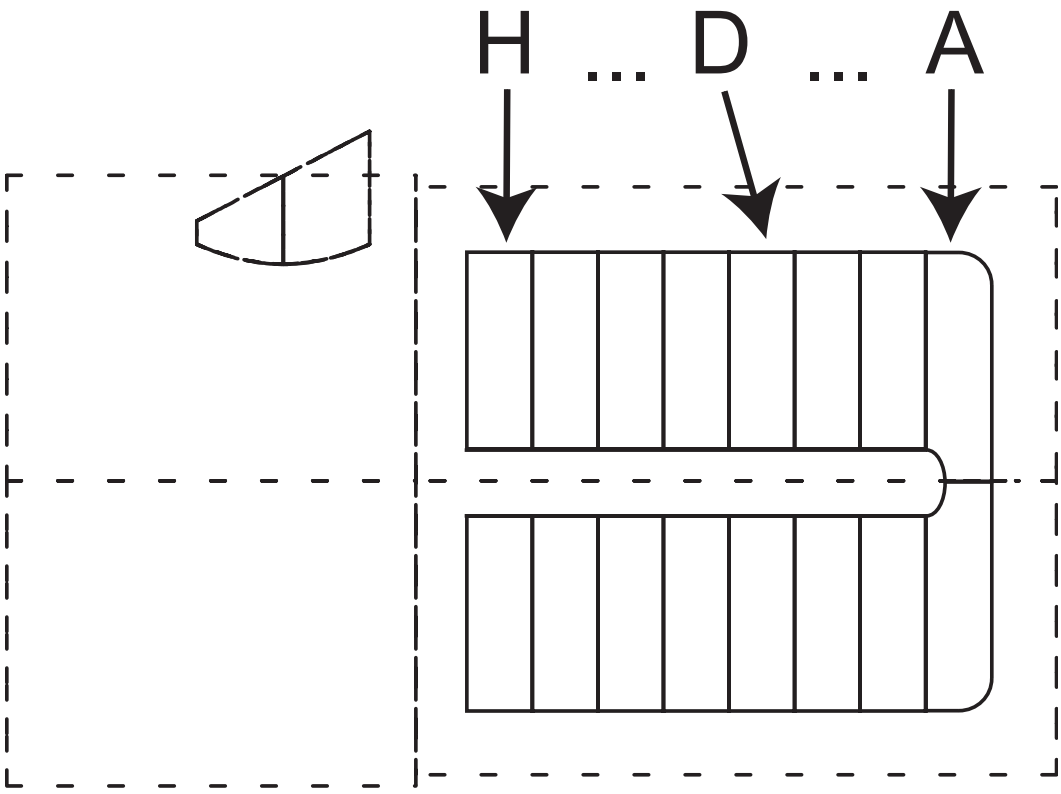

Figure 3.3: Segment labeling scheme for SeGA crystals.

red path (labeled “1”) is sensed differently by the electrode E than a charge moving on the blue path (labeled “2”). The weighting potential along paths “1” and “2” are plotted in Figure 3.5. If the charge carrier is of the same type (electron or hole), the electric field being axially symmetric, the signal produced by the charge moving on path “1” will have a larger amplitude than the charge on path “2”. Let’s consider a longitudinal cross section of the weighting potential for segment E at 45 degrees (midway between the quadrants) (Figure 3.6). A charge moving in segment D 2 mm above segment E will be sensed differently in segment E than a charge moving 4 mm above segment D. The signal amplitude of the trajectory at 2 mm will be different (larger) from the amplitude at 4 mm or more.

To qualitatively illustrate the possibility of sub-segment radial resolution, an example of three interactions is presented in Figure 3.7. It is important to keep in mind that the sensing/collecting electrodes for the segments are on the outer border of

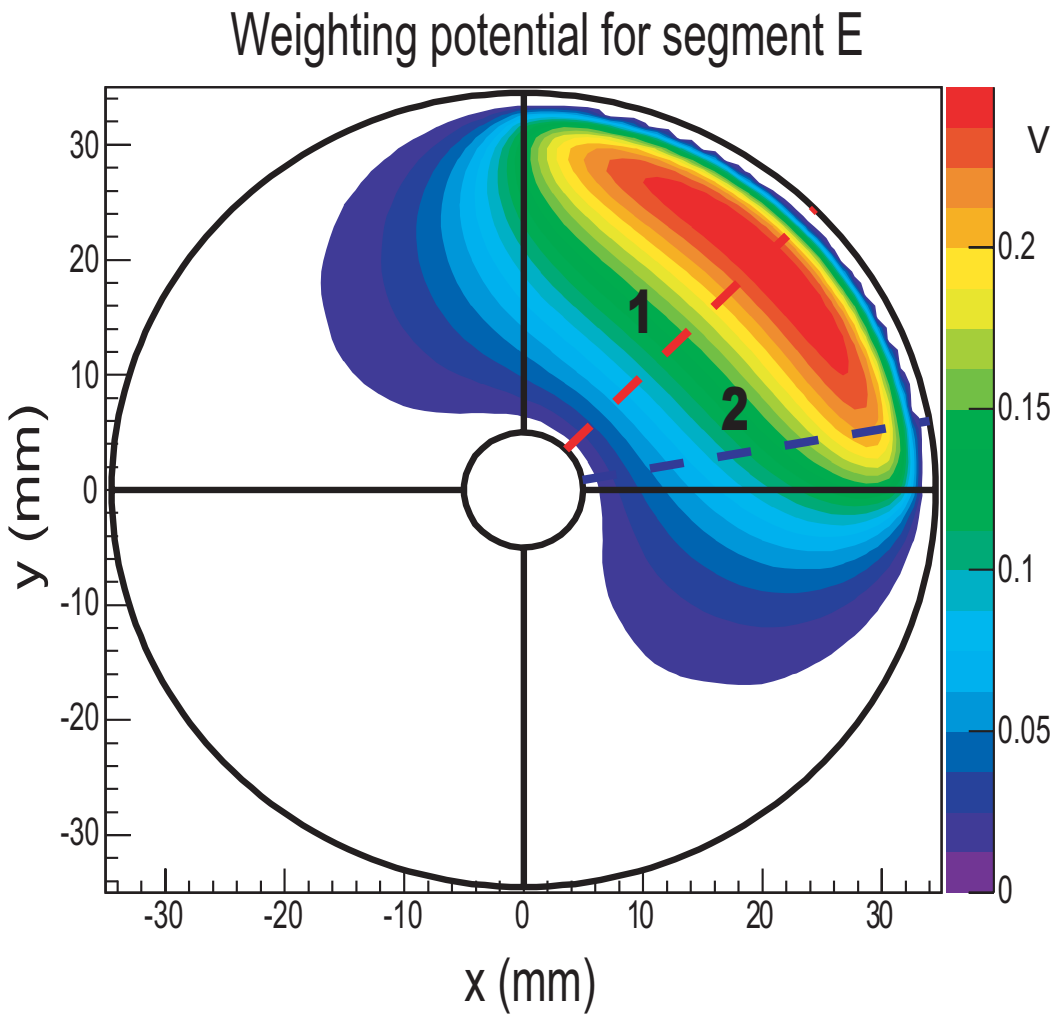

Figure 3.4: Weighting potential for segment E, transversal cut 2 mm above the border between segments E and D.

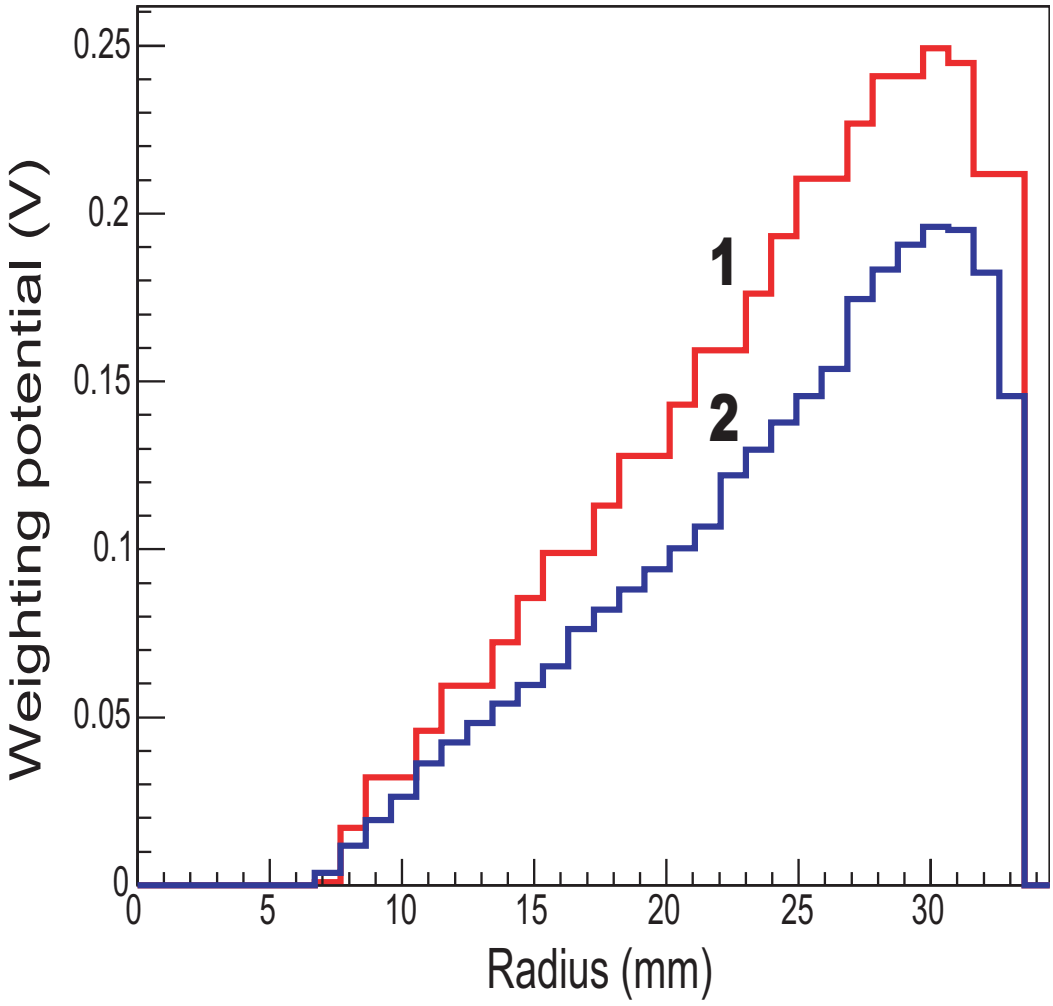

Figure 3.5: Weighting potential along the trajectories “1” and “2” in Figure 3.4.

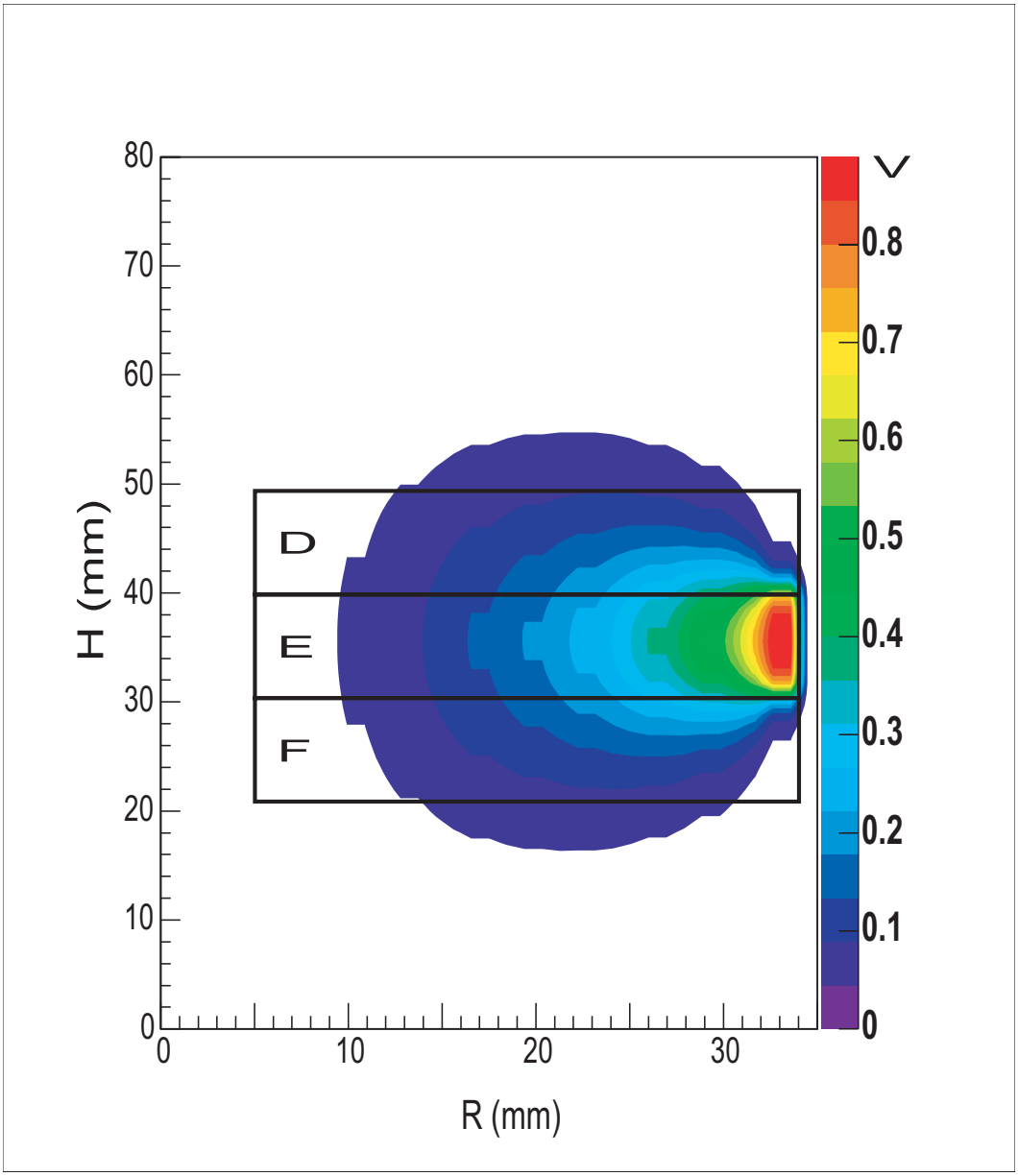

Figure 3.6: Weighting potential for segment E, longitudinal cut at 45 degrees.

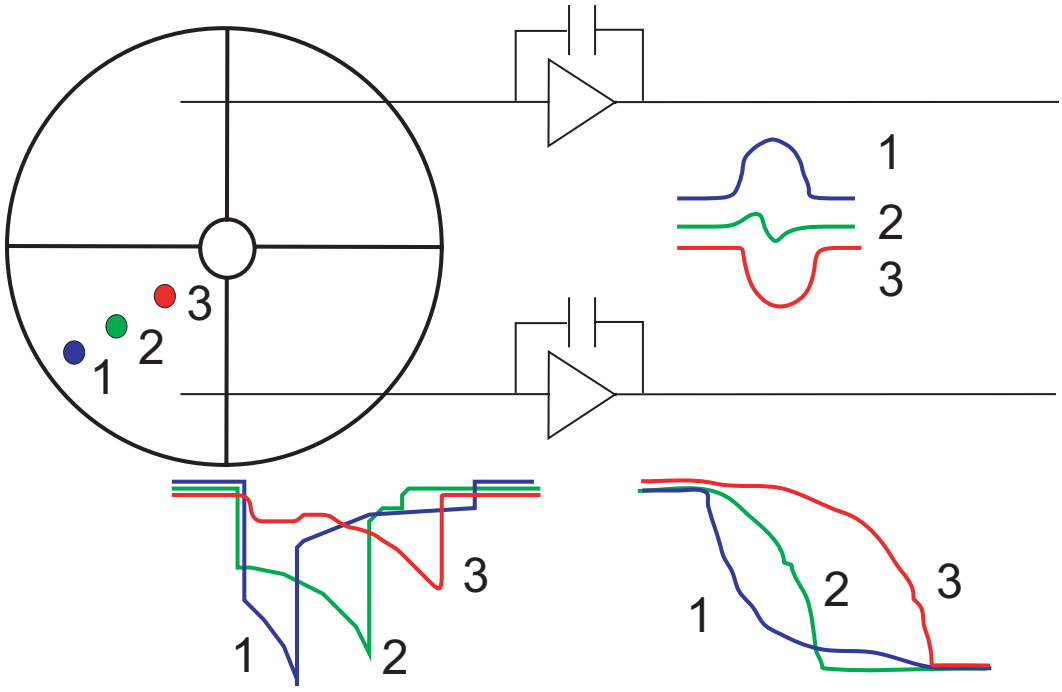

Figure 3.7: Example of real and transient charge signals.

the detector. After the electron-hole pairs are created, the electrons move toward the central contact and the holes toward the outer contacts (segments).

For the interaction point labeled "1", both electrons and holes are close to the sensing electrode. At first electrons dominate, so the shape of the signal that peaks rapidly. But since they move away from the electrode their contribution becomes smaller and smaller. The holes give a strong signal at first, but they are fully collected sooner than the electrons and their contribution soon dies out. For the interaction point labeled "3", the electrons are rapidly collected by the central contact and are far from the sensing electrode. Their contribution is small. The holes travel almost the entire radius of the detector and produce a small signal at first that gets amplified as the charge carriers get closer to the collecting electrode. The interaction point "2" is an intermediate situation. For the neighboring segments, the transient signal is a variation of positive and negative signals that integrate to zero. Signals from the SeGA detectors cannot be read directly from the crystal in a technically feasible way. Each channel has a charge-sensitive preamplifier to condition the signal. The charge-

sensitive preamplifier works in the first approximation as an integrator. The Figure 3.7 also shows the signals from the interacting and neighboring segments after the preamplifier. They have different rise times depending on the interaction position. In the interaction segments, because real charge is collected, the preamplifier integrates to a given value proportional to the charge created in the segment, which in turn is proportional to the energy deposited in the interaction.

3.3 Experimental setup

A γ-γ coincidence setup was assembled. Figure 3.8 shows the SeGA scanning stand where the experiment was performed. The purpose of the setup was to investigate the segments and the central contact signals for a single interaction Compton process. The 662 keV γ-rays from a collimated ^{137}Cs source were directed at the SeGA detector perpendicular to the detector axis. The heavimet collimator had a length of 100 mm with a cylindrical hole with a diameter of 2 mm. The distance between the radioactive source and the outer surface of the detector was about 150 mm, limiting the maximum diameter of the beam spot at the interaction region to around 5mm. A 3"x3" Bicron NaI(Tl) scintillation detector was placed underneath the SeGA detector to allow detection of γ-rays scattered from the germanium crystal. Two 50 mm thick lead bricks were used to create a collimating slit between the two detectors of about 2 mm in width. Two Struck 100 MHz sampling rate SIS3300 12-bit and two SIS3301 14-bit flash analog-to-digital converters were used to digitize the waveforms from the central contact and 31 segments out of a total of 32. For the coincidence measurements one channel was used for the pre-amplified NaI detector signal, reducing the number of digitized signals from segments to 30. To include all the shape information contained in the pulse, the length of the trace was set to include the rise time part of a segment signal with energy deposited (comparable with the drift time of 200 ns - 500 ns) and parts of the signal before and after the rising/falling edge. A number of 128 samples

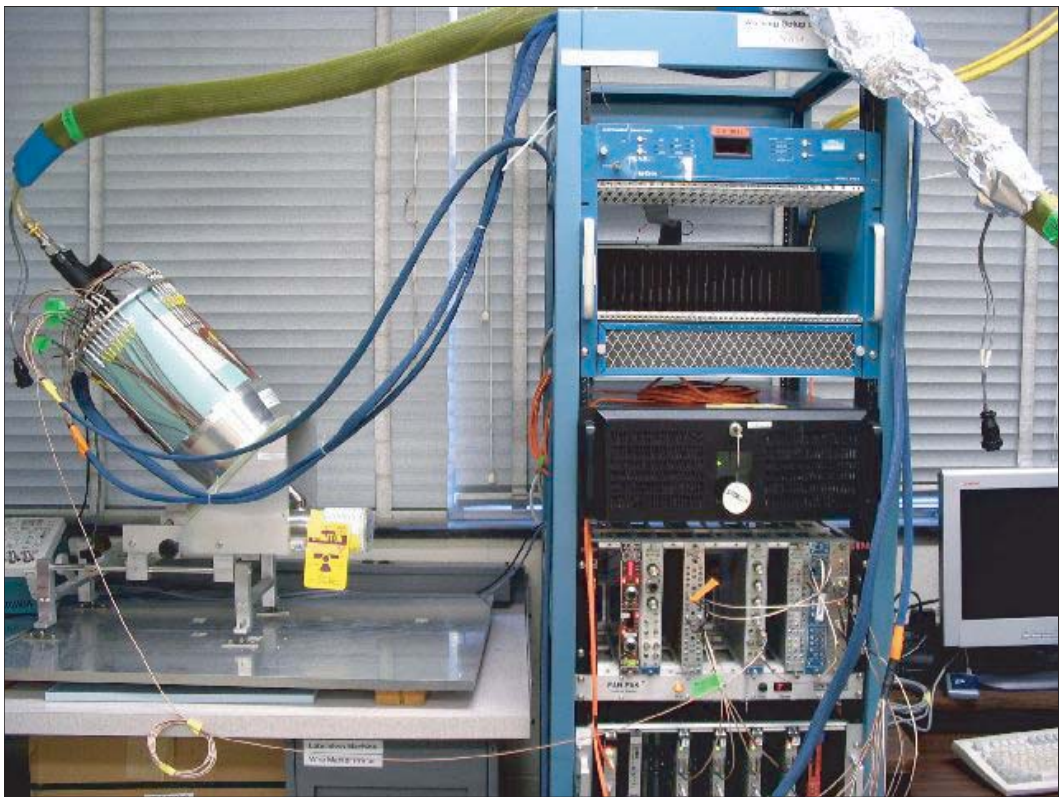

Figure 3.8: Experimental setup of the SeGA scanning stand.

per waveform is sufficient to extract timing and position information. Various settings have been tried, from 128 ($\sim$1.3 μs) to 1024 samples per trace($\sim$10μs).

All 4 digitizing modules were placed on a VME backplane communicating with the data acquisition PC via an SBS/Bit3 interface. The experimental setup used the standard NSCL data acquisition software, NSCLDAQ [68] for reading out the modules and NSCLSpecTcl [69] for data analysis. The DSP filters and the software gates particular to the analysis of this experiment were implemented as C++ classes and Tcl/Tk scripts.

3.4 Results

The collimated 662 keV photon beam has been swept across the D4 segment, parallel to the quadrant segmentation plane between segment groups 1,4 and 2,3. Due to the geometry of the setup, beside random coincidences from the room background

and cosmic rays, only the 622 keV γ-rays from the ^{137}Cs source that interact once in the HPGe detector, scatter at about 90 deg (deposited energy 370 keV) and then interact with the NaI(Tl) detector are expected to trigger the data acquisition. After the calibration of both detectors, software gates can be imposed, such that the event for which the energies deposited in the germanium and NaI have values close to the single Ge scattering at 90 deg scenario. In Figures 3.9, 3.10 and 3.11, 3.12 two relevant events are presented. In Figures 3.9 and 3.10, signals are for an interaction when the collimator is placed closer to the E side, and Figures 3.11 and 3.12 for an interaction closer to the C side. The D4 segment signal shows the deposition of 370 keV electron energy on which the γ-ray initially scattered. The amplitude of the induced signal in segment E4 is larger compared to the amplitude in segment C4 in the case showed in Figures 3.9 and 3.10. In Figures 3.11 and 3.12 the transient signal amplitudes in C4 are larger than the ones in E4.

Waveforms and simple quantities based on waveforms often have arbitrary units assigned in the plots presented. The flash ADCs have a full range of 1 V, from -0.5 V to +0.5 V. Each segment has its own DC offset. Depending on the ADC type, the full 1 V range is digitized into 4096 bins (12-bit ADC) or 16384 bins (14-bit ADC). The average sensitivity of the segment preamplifier is $\sim$ 125 mV/MeV.

For each linear position of the collimator, the differences in the induced signal amplitudes for segments E4 and C4 were histogrammed and fit with a Gaussian. The linear position of each run was plotted versus the corresponding Gaussian centroid. A linear fit to the data was performed. To diminish the effect of incorrect position determination, any position calculated to be outside a +/-3.7 mm window centered on the segment center is forced into the window's edge.

Using this algorithm, the same data set was then used to determine the algorithm's success. The average miss was calculated as the average over a given data set of the absolute value of the difference between the expected interaction point and the calculated value. The average miss for a SeGA detector using only the contact

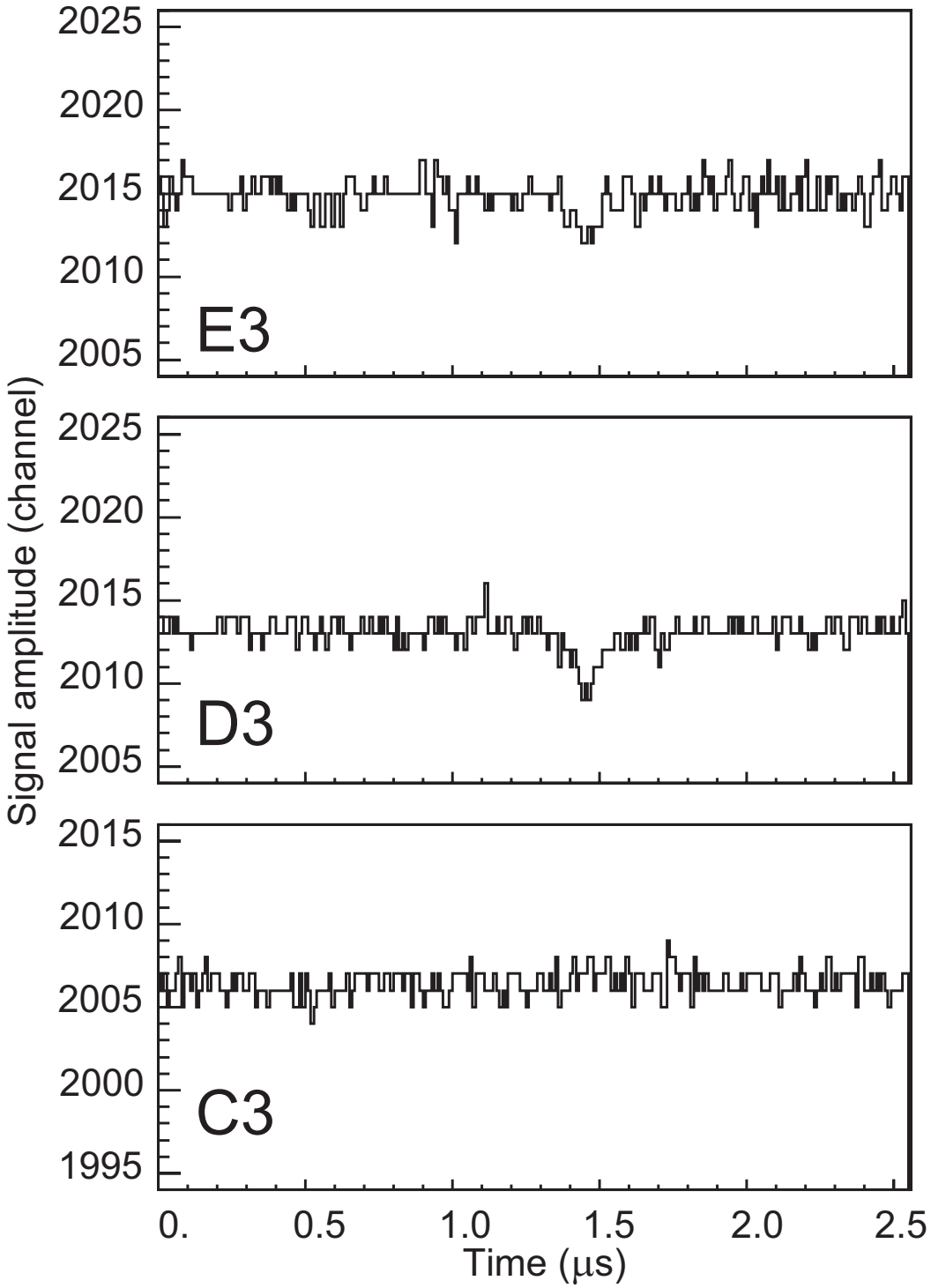

Figure 3.9: Segment signals for an interaction closer to the E4 side of the D4 segment (Quadrant 3).

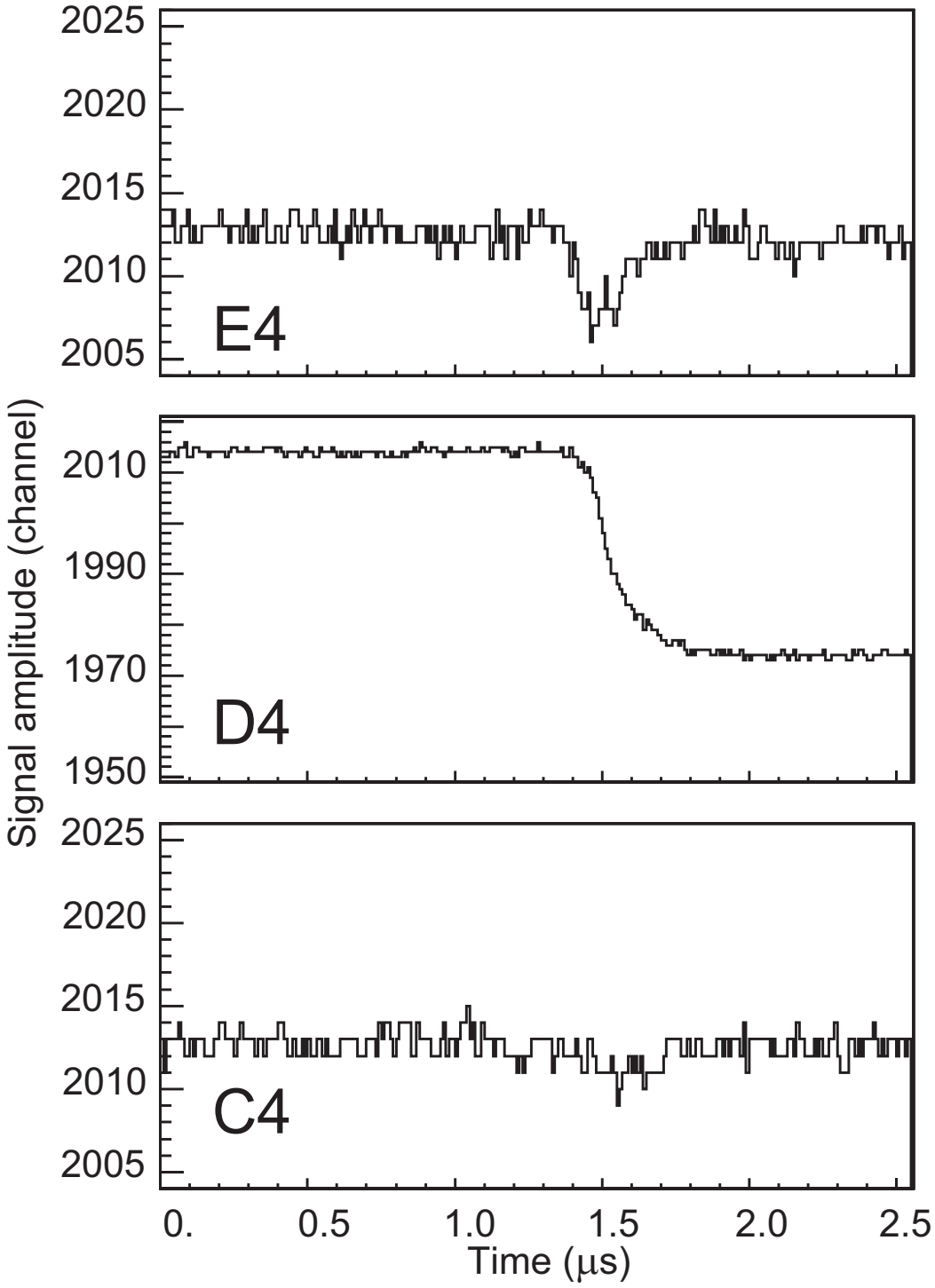

Figure 3.10: Segment signals for an interaction closer to the E4 side of the D4 segment (Quadrant 4).

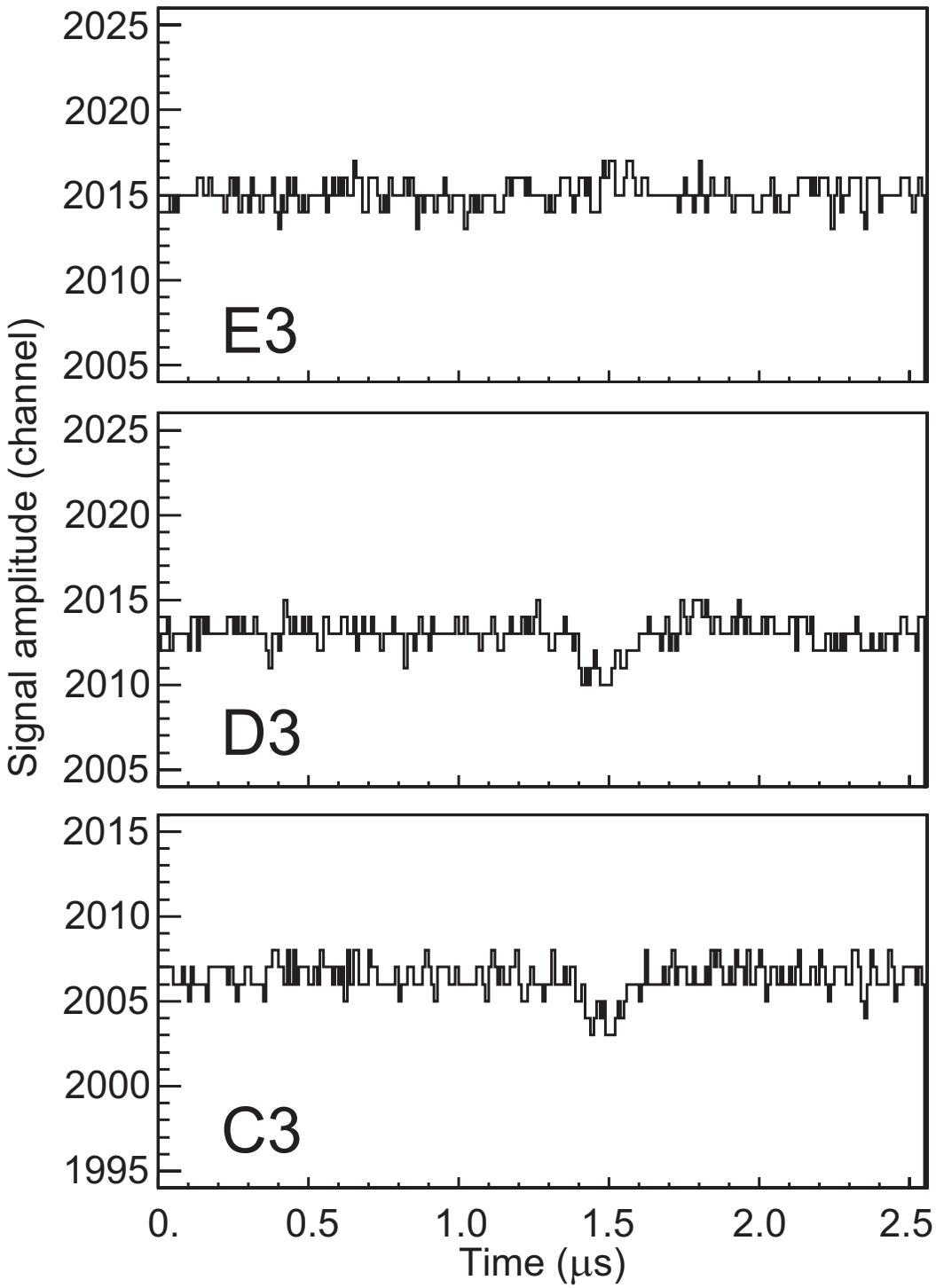

Figure 3.11: Segment signals for an interaction closer to the C4 side of the D4 segment (Quadrant 3).

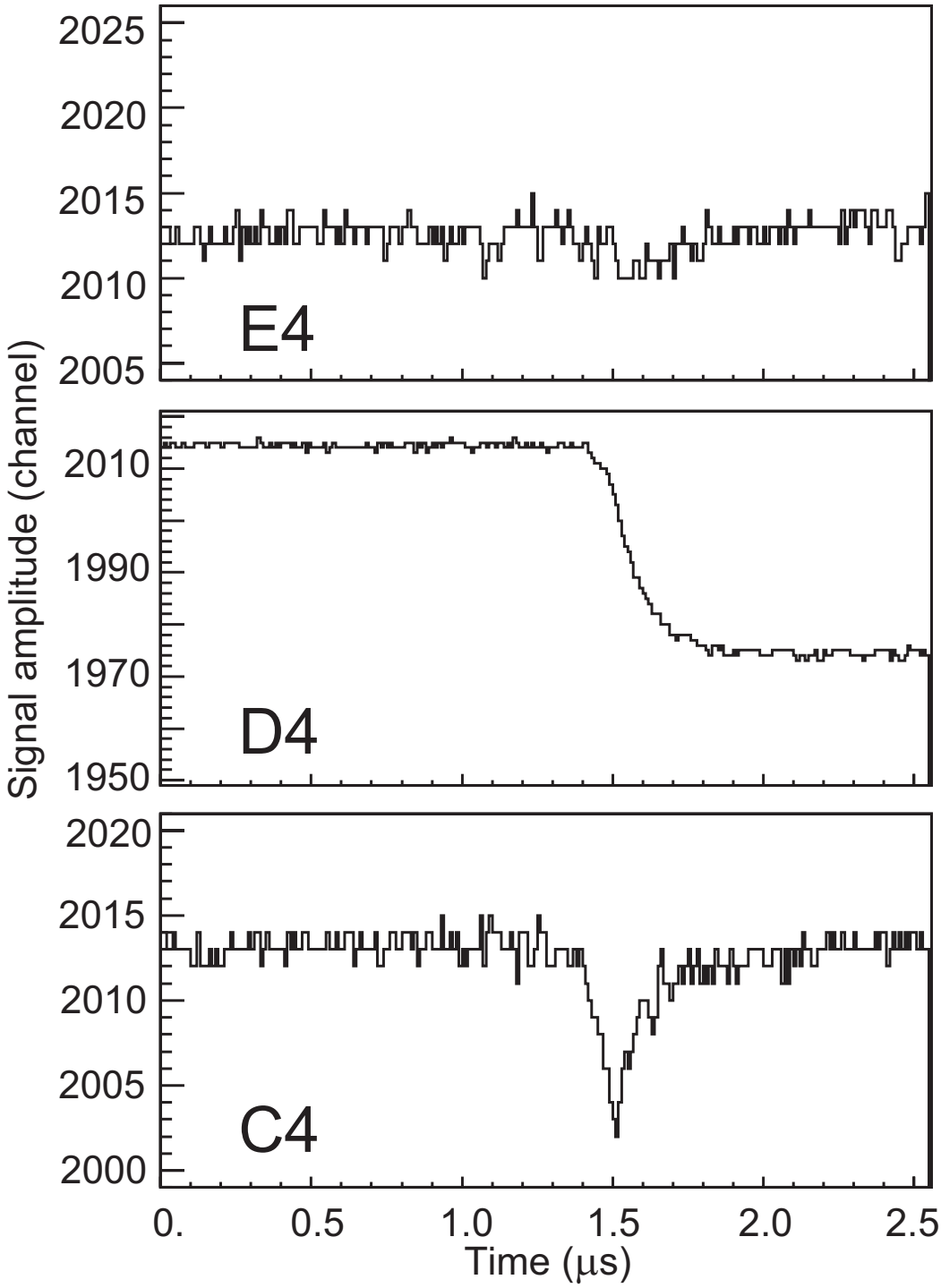

Figure 3.12: Segment signals for an interaction closer to the C4 side of the D4 segment (Quadrant 4).

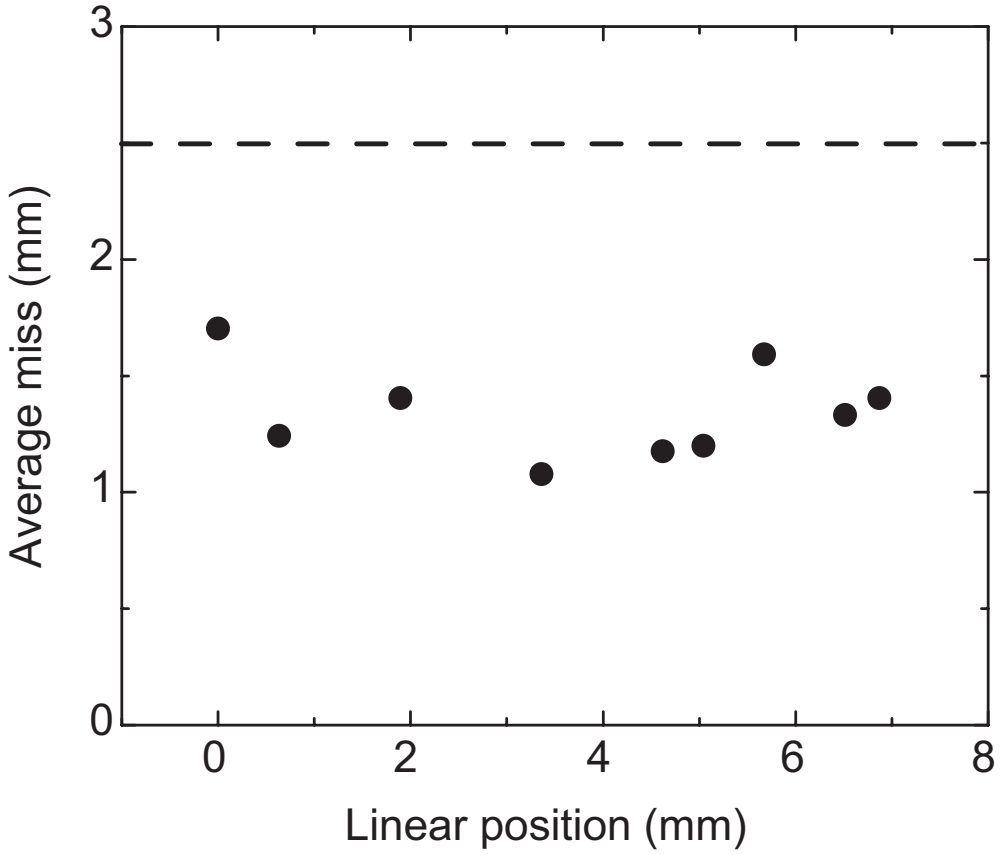

Figure 3.13: The average miss of the algorithm in estimating the interaction position for several positions of the collimator. In dashed line is plotted the theoretical average miss when no sub-segment position resolution is assumed.

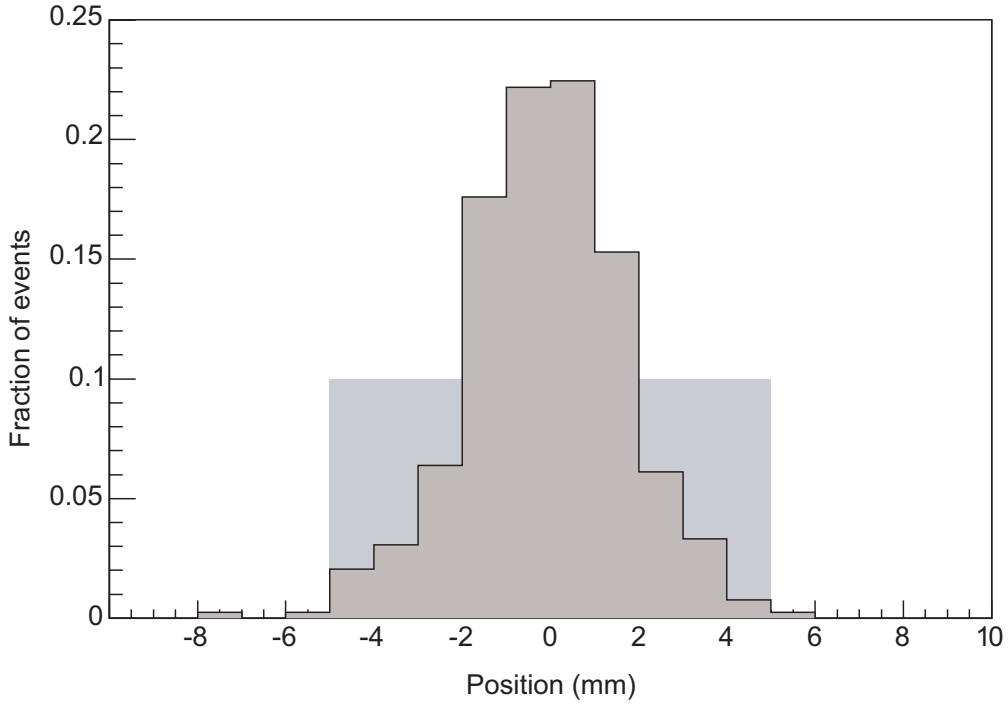

Figure 3.14: Histograms of the algorithm misses for each event in the data set when pulse shape analysis is involved (darker shade) compared to the case with no PSA (lighter color shade).

segmentation is 2.5 mm (Figure 3.13). This can be calculated by considering a uniform distribution of the events (see also Figure 3.14) and the fact that the miss in this case in the absolute value of the γ-ray interaction position. An average over the entire distribution gives a value which is a quarter of the length of the segment. The algorithm shows an improvement and works well across the length of the segment. A histogram of the misses for each event in the data set (all positions) is presented in Figure 3.14. The region colored with a lighter shade shows the expected distribution of misses when using only the contact segmentation and no pulse shape analysis.

For multiple interactions in a single segment, a gate on the 662 keV energy deposited in segment E4 was placed and the collimated beam was swept from the F side to the D side. Only the information from photons depositing their full energy in the targeted segment is recorded. With this requirement, the photon's interaction history must include either a photoelectric effect, of a succession of Compton interactions in the segment followed by a photoelectric effect. At that energy, the cross

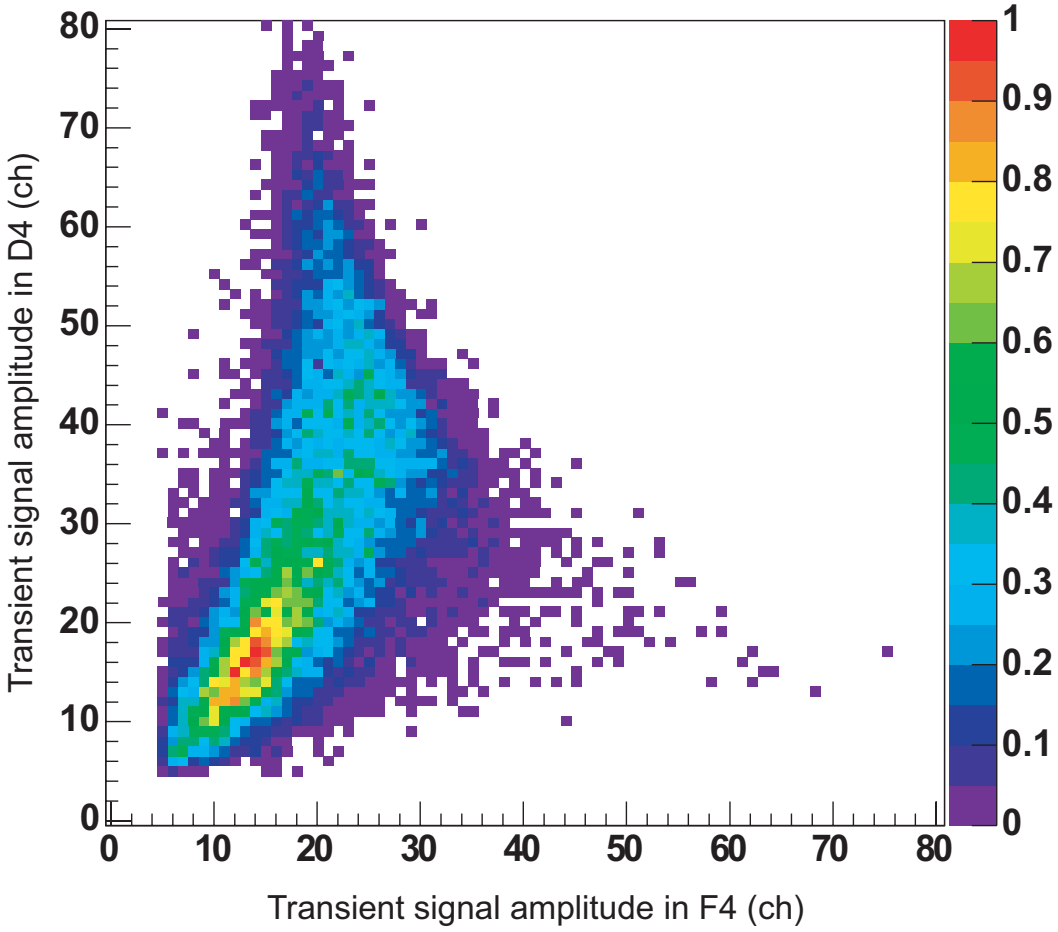

Figure 3.15: Amplitudes of the transient signals for segments F4 (horizontal) and D4 (vertical). The collimator is moved by 2 mm for each graph. First position.

section for the Compton scattering is significantly larger than the cross section for the photoelectric effect. Most likely the photon scatters several times before it is finally absorbed. Induced signal amplitudes in F4 (horizontal axis) and D4 (vertical axis) are plotted against each other in Figures 3.15, 3.16, 3.17, 3.18, 3.19. The case in Figure 3.15 corresponds to a position closer to the F side and the case in Figure 3.19 to a position of the collimator closer to the D side. The intermediary positions in Figure 3.16 through Figure 3.18 are for the collimator moved 2 mm each time. Plotted are only the positive amplitudes, for which the induced signal amplitude calculation was most reliable. Statistically it still can be estimated on which side of the segment the interactions occurred.

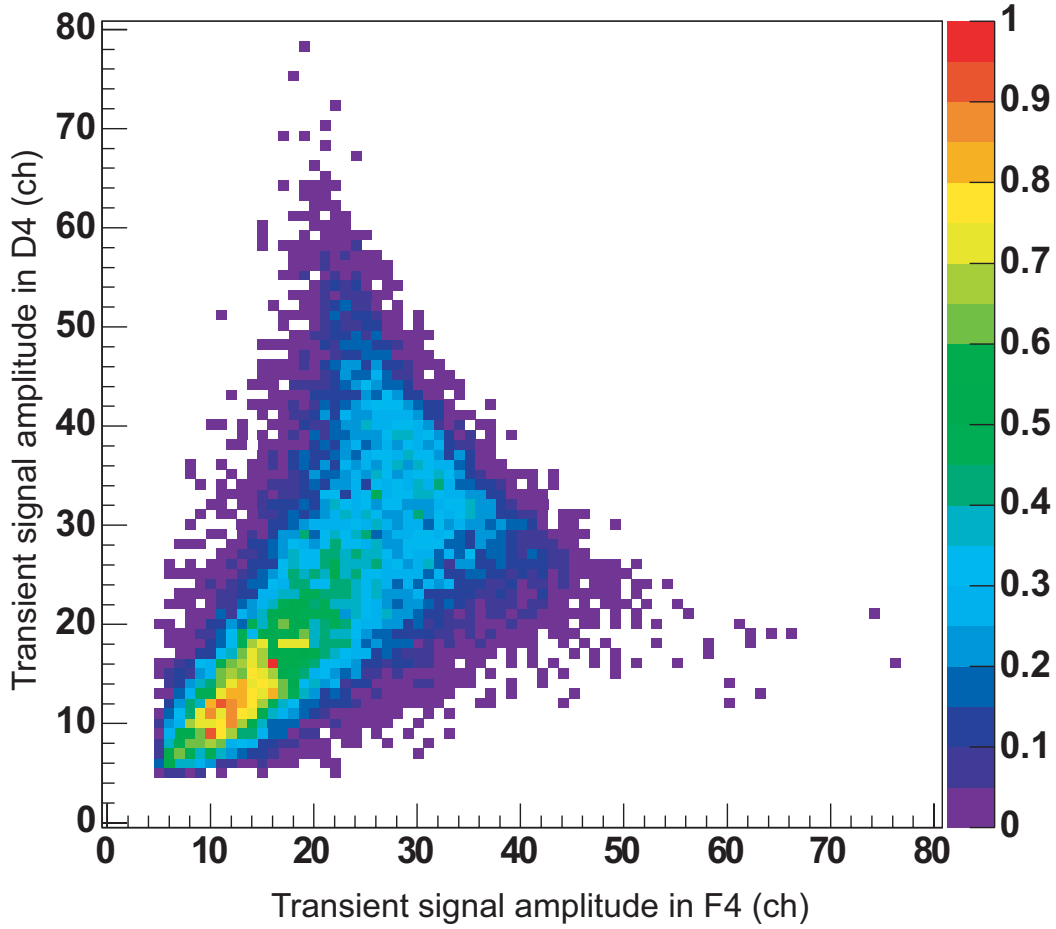

Figure 3.16: Amplitudes of the transient signals for segments F4 (horizontal) and D4 (vertical). The collimator is moved by 2 mm for each graph. Second position.

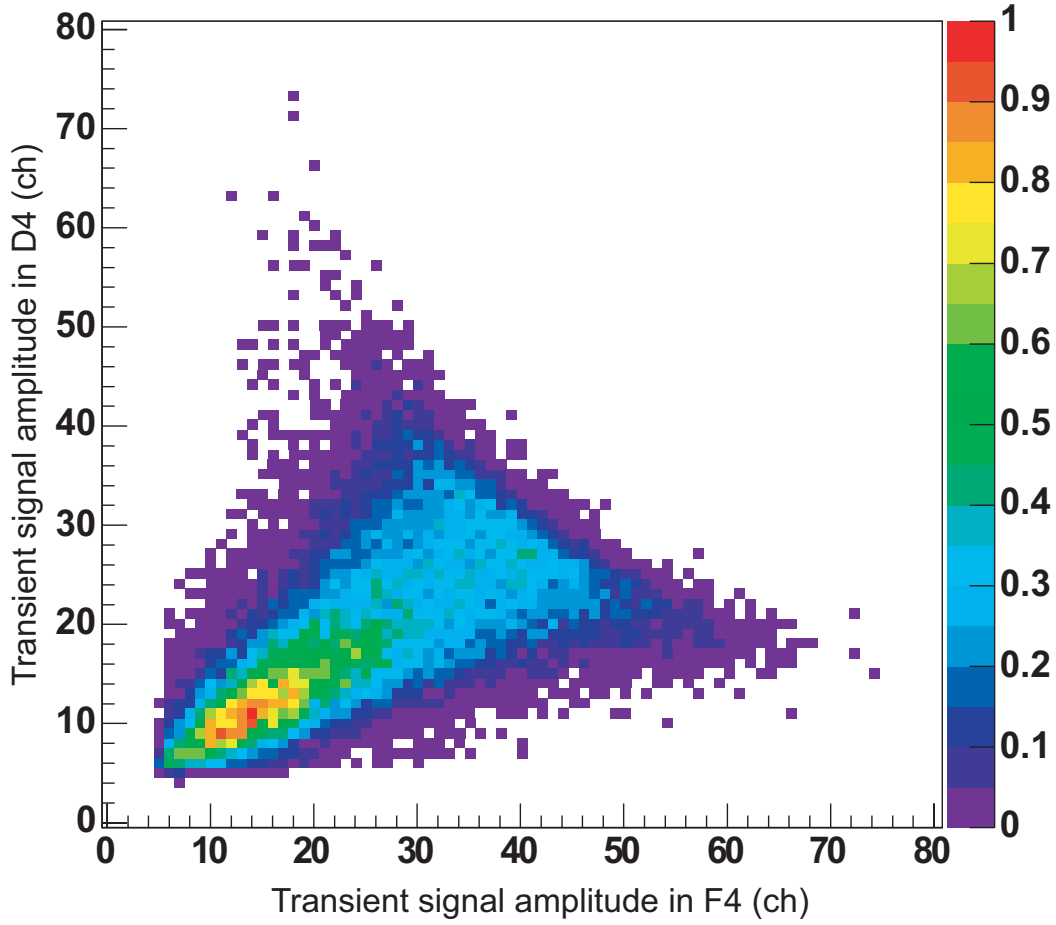

Figure 3.17: Amplitudes of the transient signals for segments F4 (horizontal) and D4 (vertical). The collimator is moved by 2 mm for each graph. Third position.

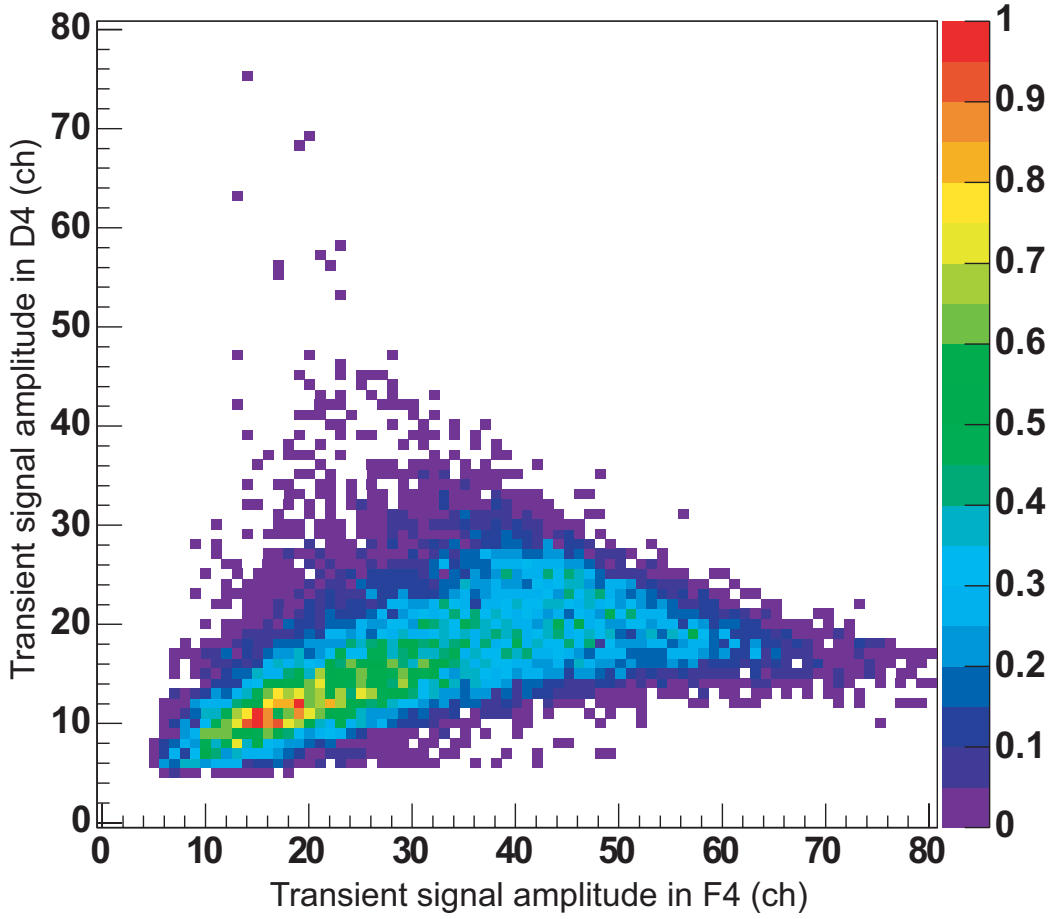

Figure 3.18: Amplitudes of the transient signals for segments F4 (horizontal) and D4 (vertical). The collimator is moved by 2 mm for each graph. Fourth position.

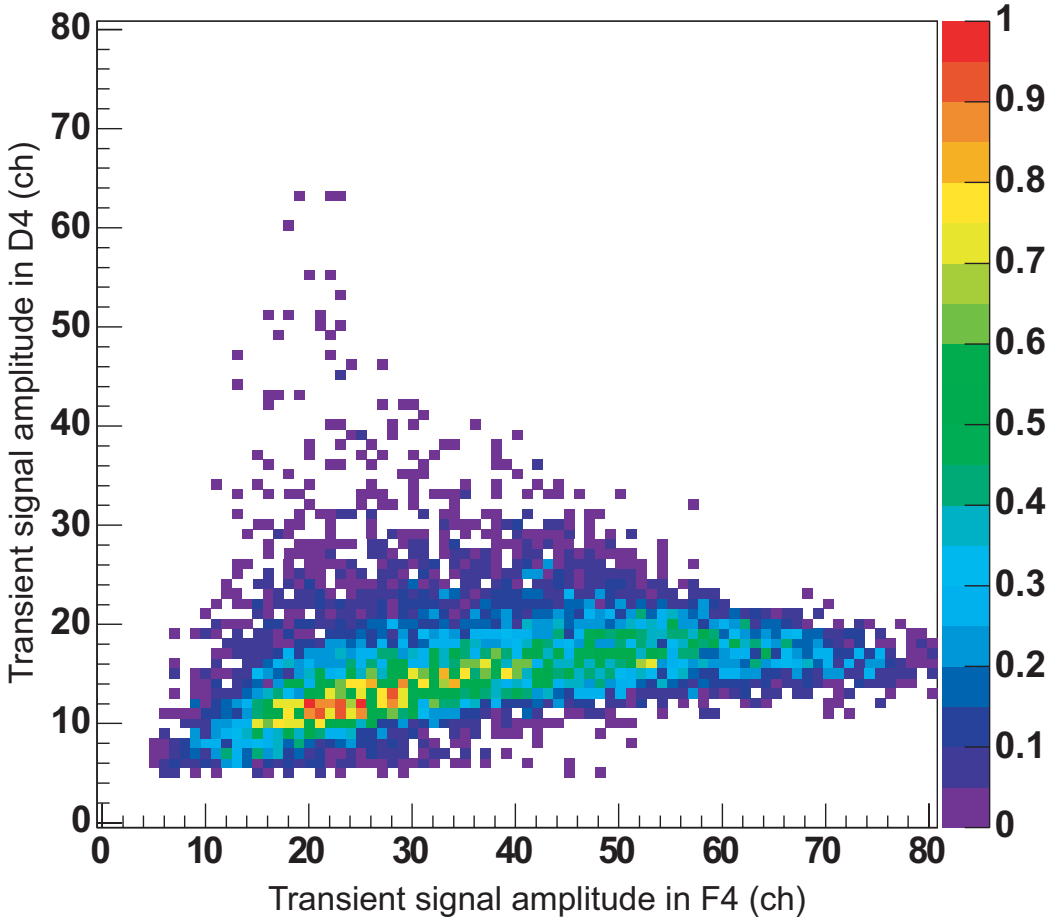

Figure 3.19: Amplitudes of the transient signals for segments F4 (horizontal) and D4 (vertical). The collimator is moved by 2 mm for each graph. Fifth position.

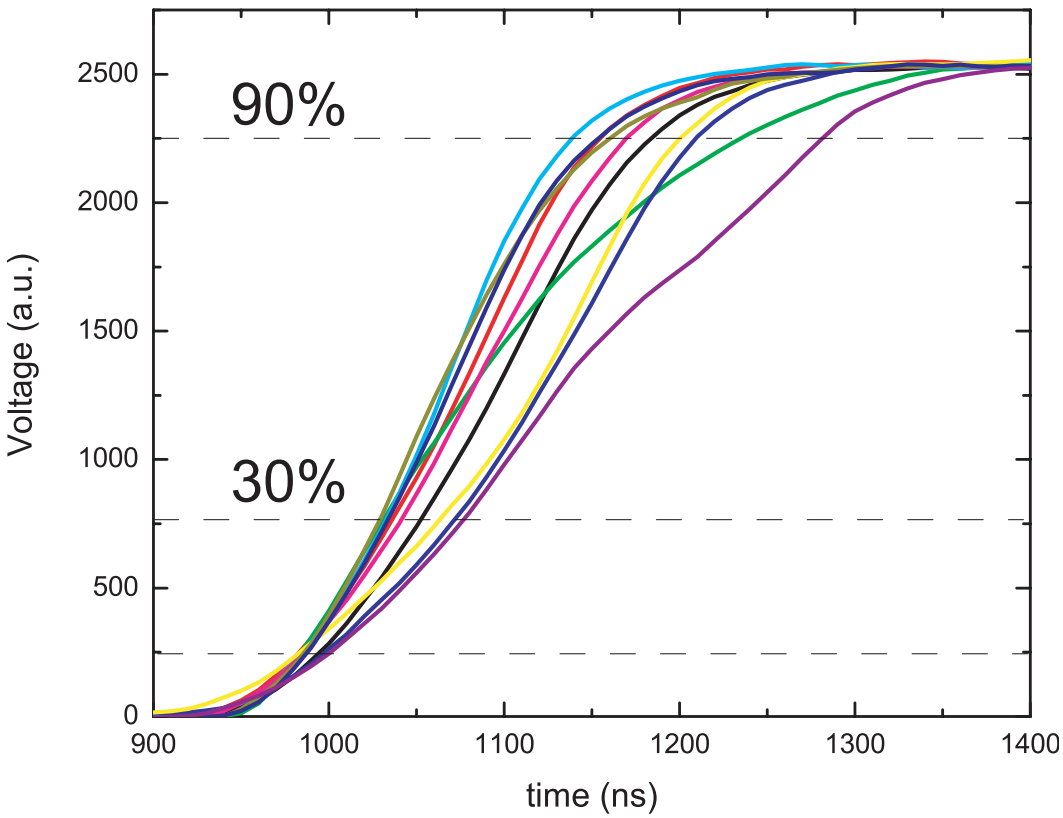

Figure 3.20: Central contact waveforms corresponding to a photopeak event at 1332 keV.

To investigate the radial position resolution, the focus was placed on the rise time analysis because it was expected that there would be a dependence of the rise times with the radial position of the interaction [70]. Figures 3.20 and 3.21 show waveforms taken from the central contact for events corresponding to a photopeak event from a 1332 keV γ-ray and from a segment in which the energy from a 662 keV γ-ray was fully deposited inside the segment, respectively.

Using the coincidence setup with the collimated source from the front of the detector and the scattered γ-rays detected at around 90 degree measurements were made for a number of radial positions. The rise time of the waveform was calculated as the time it takes to go from 10% of its total height to a given fraction of the total amplitude. Rise times for 30%, 60%, and 90% fractional amplitudes, denoted t30, t60 and t90 respectively, were measured. In Figures 3.22, 3.23, and 3.24, the three rise times are plotted function of the measured radii. The gaps on the radius axis

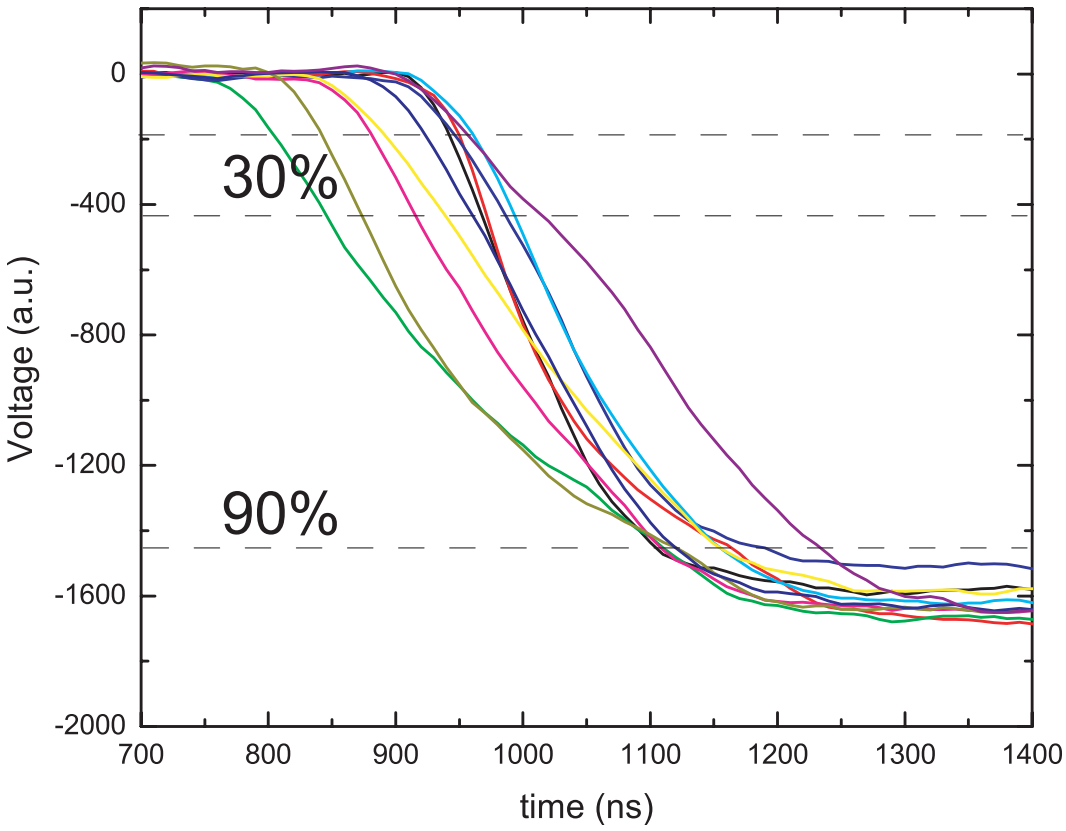

Figure 3.21: Segment waveforms corresponding to a photopeak event at 662 keV. Only the interactions in which the γ-ray energy was fully deposited in the segment are selected.

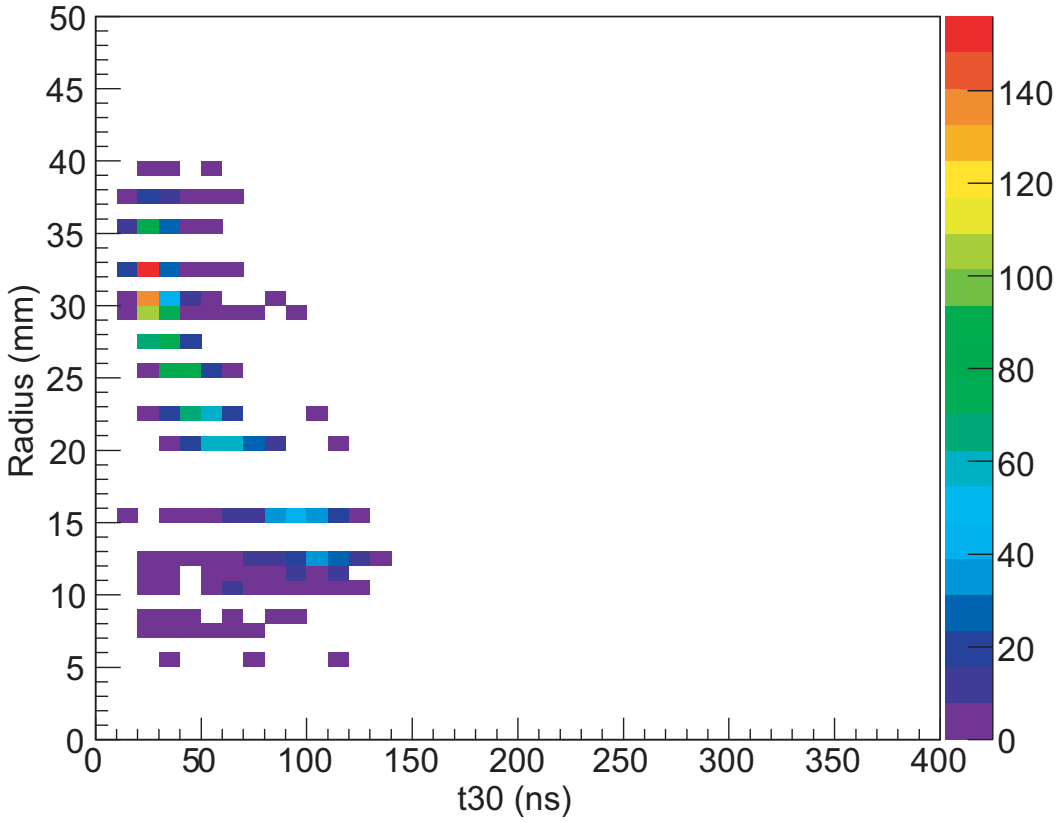

Figure 3.22: Time to reach 30% of the full amplitude (t30) plotted against the position of the collimator in the radial direction.

correspond to radii for which measurements were not performed. By plotting t30 on one axis and t90 on the other axis and color coding the radius it can be seen that the segment can be sub-segmented also along the radial dimension (see Figure 3.25).

Mostly for gating purposes, the deposited energy was reconstructed in software from the central contact and segment waveforms. When using analog electronics, the energy is usually determined by putting the pre-amplified signal into a shaping amplifier, then using the output of the shaping amplifier as the input to a peak-sensing analog-to-digital converter. With digital electronics, the digitized output of the preamplifier is recorded. The rest of the spectroscopic chain is implemented in software. Simple algorithms were used to accomplish this. The simplest one is to use the height of the signal relative to the baseline, since in principle it is proportional to the energy deposited. A baseline is calculated from the first 50 samples and it is subtracted from the signal, making the result more accurate. To reduce the high

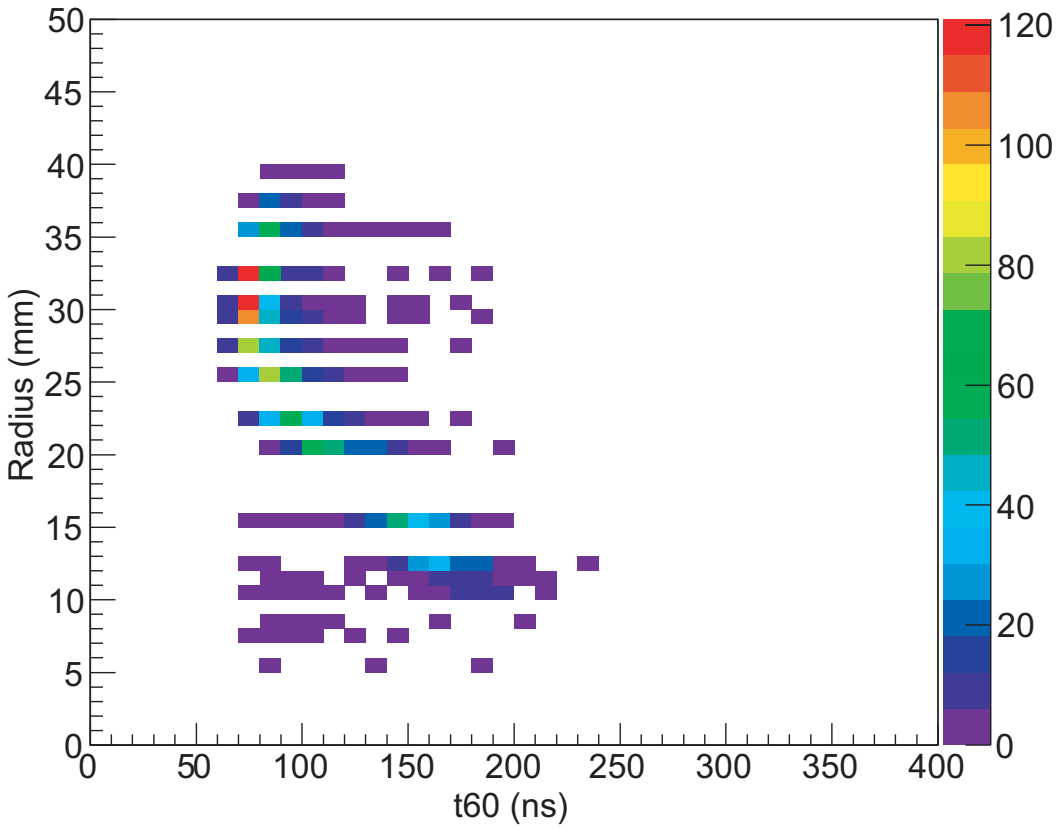

Figure 3.23: Time to reach 60% of the full amplitude (t60) plotted against the position of the collimator in the radial direction.

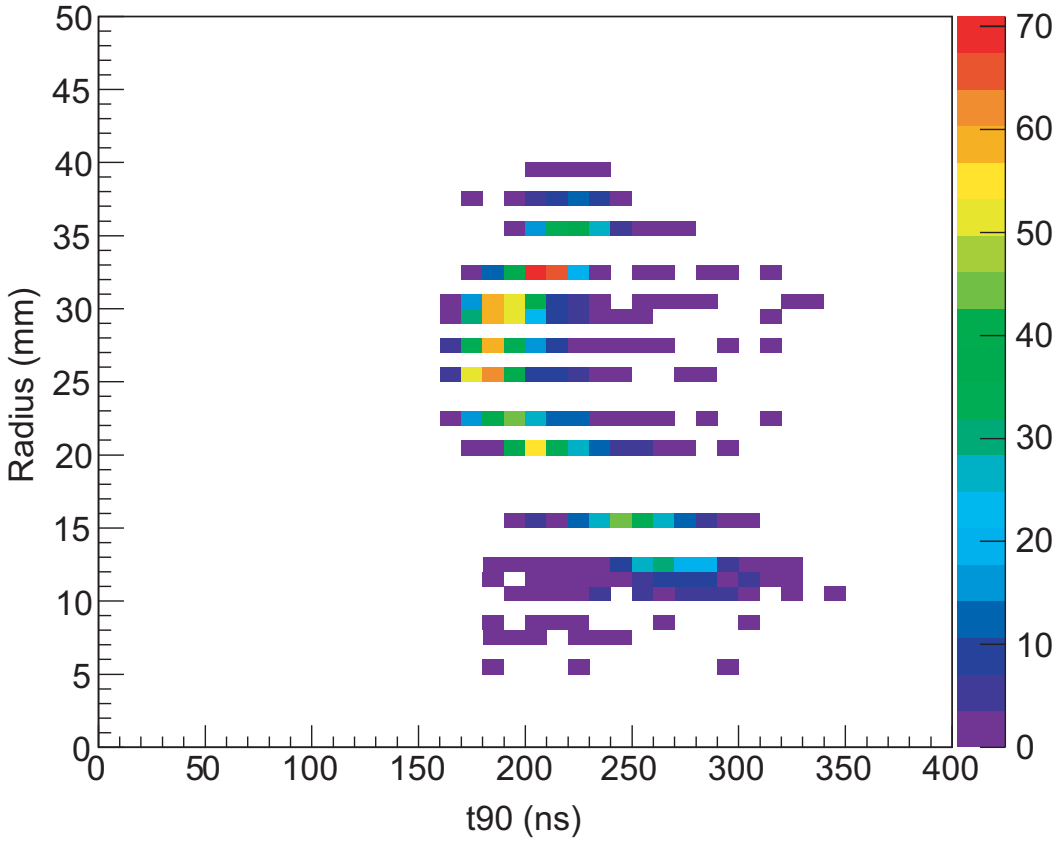

Figure 3.24: Time to reach 90% of the full amplitude (t90) plotted against the position of the collimator in the radial direction.

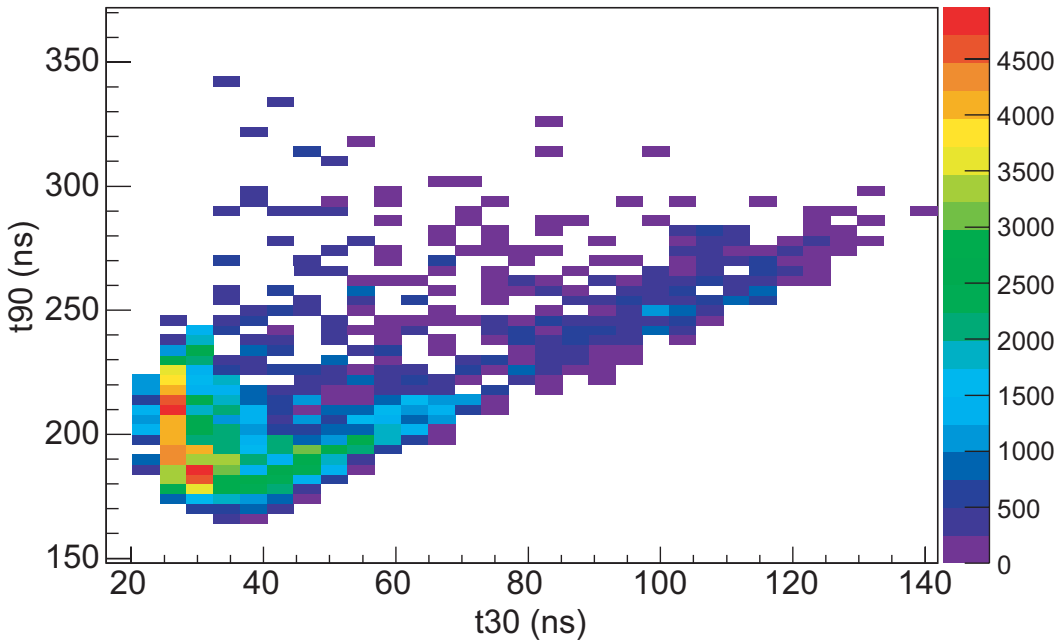

Figure 3.25: Time to reach 30% of the full amplitude plotted against the time to reach 90% of the full amplitude. The radius is color coded (arbitrary units).

frequency noise, smoothing techniques as running averages or Gaussian can be employed.

A better way to reconstruct the energy is to use a trapezoidal shaper [71, 72]. In terms of digital signal processing, this shaper is an infinite impulse response filter, with the equation:

$$y_n = y_{n-1} + x_n - x_{n-m} - x_{n-m-k} + x_{n-2*m-k}. \tag{3.7}$$

applied to the smoothed signal shape. In the relationship above x_n is the signal before the filter is applied and y_n is the resulting signal. The smoothing is done with a centered running average in 7 points or with a Gaussian filter before the trapezoidal filter is applied. A trapezoidal shaper corrects for the ballistic deficit and it also has the advantage that is easily implementable in the digitizing board's hardware. Because the various time constants involved in the signal amplification cannot be made infinitely large the signals associated with long charge collection times experience losses in the amplification. This effect is known as ballistic deficit. The filter has two independent parameters: integration time (m) and the flat top duration (k). From another perspective, it can be viewed as the difference between two running sums separated by a certain amount of samples and acting on the same trace. One drawback of this shaper is that in its simple form it does not apply pole-zero corrections. Figure 3.26 shows the central contact signal corresponding to a 1332 keV event from a ^{60}Co source, along with the same signal after a trapezoidal shaper with integration time of 1 μs and flat-top duration of 0.5 μs is applied. Notice the undershoot of the shaped signal on the right side of the trapezoid. The shape can be straightened with a pole-zero correction algorithm, like the Moving Window Deconvolution algorithm, for example Reference [73], leading to an improvement in the energy resolution. For the trapezoidal filter without any additional corrections, integration time 4 μs and flat-top duration 2 μs, the energy resolution attained was

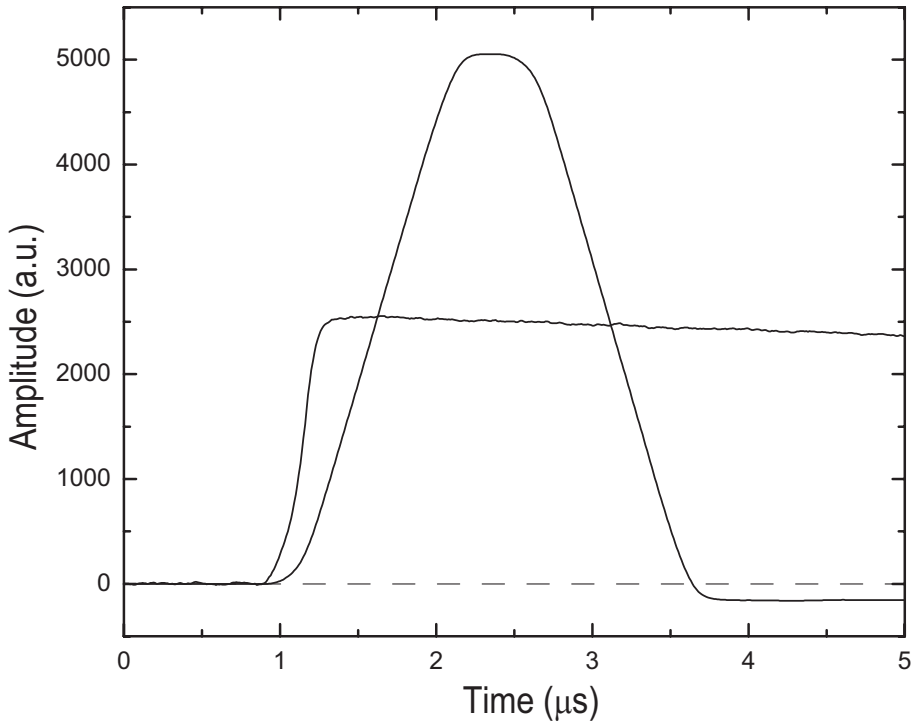

Figure 3.26: The central contact signal corresponding to a 1332 keV event and a trapezoidal shaper with integration time of 1 μs and flat-top duration of 0.5 μs applied on it.

about 4.6 keV Full width at half maximum (FWHM) for the central contact and 5.2 keV FWHM for segments for the ^{137}Cs 661.62 keV line. A previous measurement of the central contact energy resolution using a shaping amplifier and an ADC produced a value of 2.95 keV for the 1332 keV ^{60}Co line. The other methods tried (a CR-RC filter [74] and a trapezoidal shaper applied on a signal with the preamplifier decay time corrected) marginally improved the resolution. The main factor in the loss of energy resolution compared to the analog spectroscopic chain is the short integration time. Details of the algorithms and filters used are presented in the Appendix.

3.5 Summary

The goal of this study was to provide a basis and a proof-of-principle argument to future investigations. For single Compton interactions, the position resolution has been

increased from a theoretical 2.5 mm to 1.5 mm. Interaction positions for unrestricted events within a segment can be qualitatively assigned to one side of the segment or the other. Radial interaction position resolution can be achieved with rise time analysis.

A significant improvement in the scientific output of SeGA can be obtained with modest improvements in the Doppler correction mechanisms. There is a balance between the γ-ray efficiency of the spectroscopic system and its energy resolution. By doubling the effective segmentation along the z axis, the efficiency can be increased 4 times while the resolution is kept the same if the distance between target and detectors is reduced by half. This can either increase the number of counts in photopeaks four-fold, or reduce the beam time and cost of the beam time by a factor of four. This adds more flexibility to SeGA. Depending of which factor is critical, efficiency for very low rate beams or small cross sections or resolution for identification of doublets or the need for high peak-to-background ratios, the layout of detectors in the array can be modified to fit the experiment's needs.

Chapter 4

Conclusions

Quantum mechanical observables $B(E2; 0^+ \rightarrow 2_1^+)$ have been measured for the neutron-rich titanium isotopes ^{52}Ti, ^{54}Ti, and ^{56}Ti via intermediate-energy Coulomb excitation. Correlated with the energies of the first excited states of these nuclei, the reduced transition elements suggest a shell gap at neutron number N=32. There is no indication of a shell gap at N=34. Theoretical studies are presently under way to investigate further the energy spacings between the $p_{3/2}$, $p_{1/2}$ and $f_{5/2}$ neutron orbitals.

Doppler correction is essential in the determination of the de-excitation γ-ray energies emitted by fast-moving nuclei. An important ingredient in the Doppler correction is the estimation of the point where the first interaction of a photon inside the germanium detector occured. It has been demonstrated that for the SeGA detectors a sub-segment position resolution can be attained by using quantities directly derived (amplitudes, fractional rise times) from digitized central contact and segments waveforms.

Appendix A

Algorithm description

The Appendix describes the algorithms used in Chapter 3 for processing digitized waveforms taken from a SeGA detector's central contact and segments.

A.1 Centered running average

The filter generates an average of the sample with three samples before and three samples after.

$$y_n = \frac{x_{n+3} + x_{n+2} + x_{n+1} + x_n + x_{n-1} + x_{n-2} + x_{n-3}}{7}. \tag{A.1}$$

```
// centered running average using 7 points
void CWaveform::centeredRunningAverage()
{
//first and last 2 elements remain in the initial state
  for (unsigned int i = 3; i < m_iSize - 3; i++)
  {
     m_pWave[i] =  m_pWave[i+3]+ m_pWave[i+2]
                + m_pWave[i+1] + m_pWave[i]
             + m_pWave[i-1] + m_pWave[i-2] + m_pWave[i-3];
```

```
  m_pWave[i] /= 7.;
  }

  // now set the first and last 3 values
   m_pWave[0] = m_pWave[1]
              = m_pWave[2]
              = m_pWave[3];
   m_pWave[m_iSize - 3] = m_pWave[m_iSize - 2]
                        = m_pWave[m_iSize - 1]
                        = m_pWave[m_iSize - 4];
}
```

A.2 Gaussian smoothing using 9 points

A weighted average rather than a simple average is used for the Gaussian filter. The weighting factors form a Gaussian centered four samples before the current sample (Figure A.1).

$$y_n = \frac{x_n + 8x_{n-1} + 28x_{n-2} + 56x_{n-3} + 70x_{n-4} + 56x_{n-5} + 28x_{n-6} + 8x_{n-7} + x_{n-8}}{256}. \tag{A.2}$$

```
// Gaussian smoothing using 9 points
// y(n) = x(n) + 8*x(n-1) + 28*x(n-2) + 56*x(n-3) + 70*x(n-4) +
//        56*x(n-5) + 28*x(n-6) + 8*x(n-7) + x(n-8)
// The sum of all coefficients is 256.
void CWaveform::gaussianSmooth9()
{
//first 8 elements remain in the initial state
```

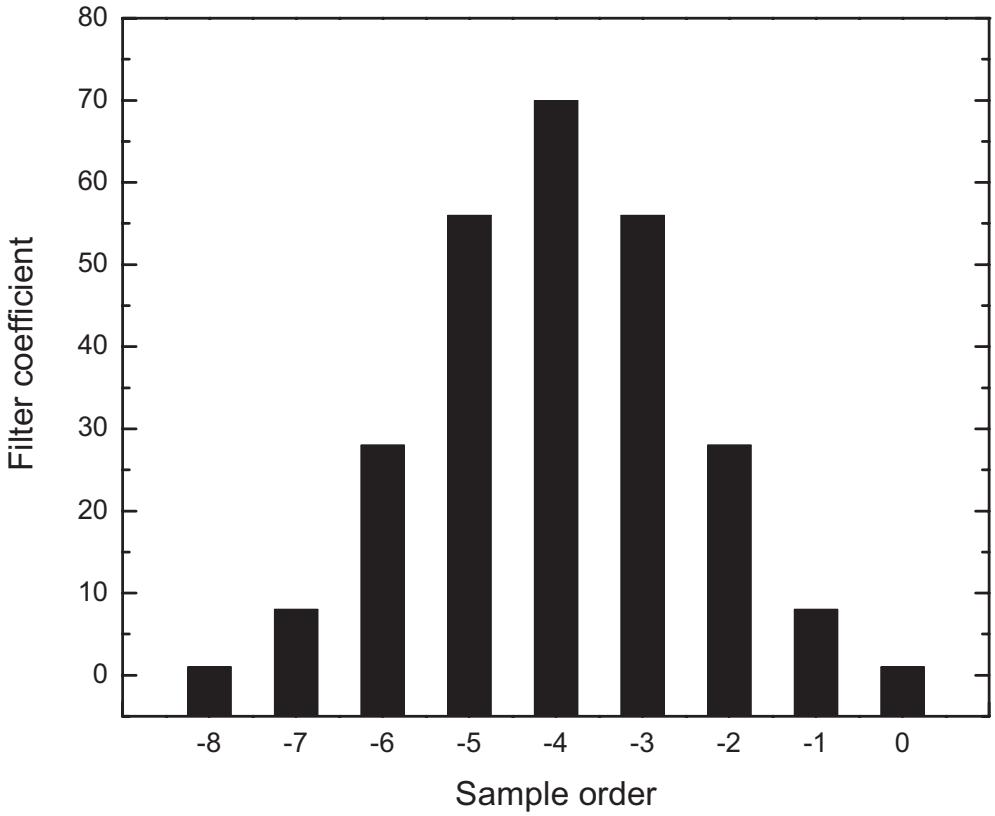

Figure A.1: Gaussian filter coefficients.

```
  for (unsigned int i = 8; i < m_iSize; i++)
  {
    m_pTest[i] = m_pWave[i] + 8.*m_pWave[i-1] + 28.*m_pWave[i-2] +
         56.*m_pWave[i-3] + 70.*m_pWave[i-4] +  56.*m_pWave[i-5] +
         28.*m_pWave[i-6] + 8.*m_pWave[i-7] + m_pWave[i-8];
    m_pTest[i] /= 256.;
  }
  //set the calculated elements
  for (unsigned int i = 8; i < m_iSize; i++)
  {
     m_pWave[i] = m_pTest[i];
  }
  // now set the first 8 elements
  for (unsigned int i = 0; i < 8; i++)
  {
    m_pWave[i] = m_pTest[8];
  }
}
```

A.3 Signal derivatives

Derivatives are important in estimating the signal before it is integrated by the charge-sensitive preamplifier. However, due to the noise present in the system, the following relationships cannot be used for real waveforms without smoothing.

The first derivative is calculated with:

$$y_i = \frac{-x_{i+2} + 8.x_{i+1} - 8.x_{i-1} + x_{i-2}}{12} \tag{A.3}$$

and the second derivative with:

$$y_i = \frac{-x_{i+2} + 16.x_{i+1} - 30.x_i + 16.x_{i-1} - x_{i-2}}{12} \tag{A.4}$$

```
void CWaveform::calculateDerivatives()
{
  //first and last 2 elements remain in an indefinite state
  for (unsigned int i = 2; i < m_iSize - 2; i++)
  {
    m_pDeriv1[i] = -m_pWave[i+2] + 8.*m_pWave[i+1]
                   -8.*m_pWave[i-1] + m_pWave[i-2];
    m_pDeriv1[i] /= 12.* m_dStep;

    m_pDeriv2[i] = -m_pWave[i+2] + 16.*m_pWave[i+1] -30.*m_pWave[i]
                +16.*m_pWave[i-1] - m_pWave[i-2];

    m_pDeriv2[i] /= 12.* m_dStep * m_dStep;
  }

  // zero the undefined points
  m_pDeriv1[0] = m_pDeriv1[1]
               = m_pDeriv1[m_iSize - 2]
               = m_pDeriv1[m_iSize -1] = 0.0;
  m_pDeriv2[0] = m_pDeriv2[1]
               = m_pDeriv2[m_iSize - 2]
               = m_pDeriv2[m_iSize -1] = 0.0;
}
```

A.4 Linear fit

Function to perform a linear regression on a portion of the waveform. It was used to estimate slopes of waveform rising edges and to measure in a first approximation the preamplifier decay time constant. The relations in the code work only for sampling of type (x_i, y_i) where x_i is defined as:

$$x_i = x_0 + i\delta_x \tag{A.5}$$

where δ_x is the spacing between samples. The fit function is:

$$Y = a + bX \tag{A.6}$$

The routine returns the (a, σ_a), (b, σ_b). With a extra pass it calculates χ^2.

```
struct LinRegressCoef
CWaveform::fitDataSegmentWithLine(unsigned int iBegin,
                                  unsigned int iNrSamples)
{
   double dSumX, dSumX2, dSumY= 0.0,
          dSumY2 =0.0 , dSumXY = 0.0, dDiscr;
   double dDeltaX = SAMPLING_DELTA;
   double a, b, Sig_a, Sig_b, dSigmaY, dChi2 = 0.0;
   struct LinRegressCoef Coeff;

   //check for possible out of boundary errors
   if (iBegin+iNrSamples >= WAVEFORM_SIZE)
   {
    cerr << "-------------------------------------------------"
          << endl;
```

```
 cerr << "WARNING -- The operation as requested would require"
       << "                          out of boundary access"
       << endl;
 cerr << "WARNING -- A truncation will be performed"
       << endl;
 cerr << "-------------------------------------------------"
       << endl;
 iNrSamples = WAVEFORM_SIZE - iBegin;
}
if (iBegin >= WAVEFORM_SIZE)
{
 cerr << "-----------------------------------------------"
      << endl;
 cerr << "ERROR -- The operation as requested would require"
      << "                         out of boundary access"
      << endl;
 cerr << "ERROR -- Returning zeroes..."
      << endl;
 cerr << "-----------------------------------------------"
      << endl;
 Coeff.a = 0.0;
 Coeff.b = 0.0;
 Coeff.siga = 0.0;
 Coeff.sigb = 0.0;
 Coeff.chi2 = 0.0;
 return(Coeff);
}
//sum of x
```

```
dSumX = 0.5*dDeltaX*(iNrSamples - 1)*iNrSamples +iNrSamples*iBegin;
//sum of x^2
dSumX2 = (1./6.)*iNrSamples*(dDeltaX*dDeltaX*\
       (2*iNrSamples*iNrSamples-3*iNrSamples+1)+\
       6.*dDeltaX*(iNrSamples-1)*iBegin+6.*iBegin*iBegin);
// discriminant
dDiscr = dDeltaX*dDeltaX*iNrSamples*iNrSamples
       *(iNrSamples*iNrSamples -1)/12.;
// for calculating Sum_y, Sum_y^2 ,and Sum_xy we need a loop
for (unsigned int i = iBegin; i < iBegin + iNrSamples; i++)
{
 dSumY += m_pWave[i];
 dSumY2 += m_pWave[i]*m_pWave[i];
 dSumXY += i*m_pWave[i];
}
// calculate the coefficients and their uncertainties
a = (dSumX2*dSumY - dSumX*dSumXY)/dDiscr;
b = (iNrSamples*dSumXY - dSumX*dSumY)/dDiscr;
// this pass is for calculating Chi-squared
for (unsigned int i = iBegin; i < iBegin + iNrSamples; i++)
{
 dChi2 += (m_pWave[i] - (b*i+a))*(m_pWave[i] - (b*i+a));
}
dSigmaY = sqrt(dChi2/(iNrSamples - 2));
Sig_a = dSigmaY*sqrt(dSumX2/dDiscr);
Sig_b = dSigmaY*sqrt(iNrSamples/dDiscr);
Coeff.a = a;
Coeff.b = b;
```

```
   Coeff.siga = Sig_a;
   Coeff.sigb = Sig_b;
   Coeff.chi2 = dChi2;
   return (Coeff);
}
```

A.5 Threshold passing point

The function returns the point on the waveform where the amplitude is higher than a given threshold. If the threshold is given as a fraction (f) of the amplitude of the waveform, then the point is:

$$y_{threshold} = y_{low}(1 - f) + y_{hi} * f \tag{A.7}$$

where y_{low} is the waveform baseline and y_{hi} is the maximum amplitude. It is between a simple leading-edge discriminator but the performance is lower than of a constant-fraction discriminator (CFD). In the case of a CFD, the zero-crossing point (the actual trigger point) is more accurate.

```
struct PairXY
CWaveform::getThresholdPassPoint(double dLowest,
                                 double dHighest,
                                 double dFraction,
                         enum DetectorType DetType)
{
   struct PairXY ThresholdPoint;

   if (DetType == GE_CENTRAL_CONTACT)
   {
```

```
 for(unsigned int i = 0; i < m_iSize; i++)
 {
  if( m_pWave[i] >= dLowest*(1. - dFraction) + dHighest*dFraction)
  {
   ThresholdPoint.x = (double)i;
   ThresholdPoint.y = m_pWave[i];
   return (ThresholdPoint);
  }
 }
}
if (DetType == GE_SEGMENT)
{
 for(unsigned int i = 0; i < m_iSize; i++)
 {
  if( m_pWave[i] <= dHighest*(1. - dFraction) + dLowest*dFraction)
  {
   ThresholdPoint.x = (double)i;
   ThresholdPoint.y = m_pWave[i];
   return (ThresholdPoint);
  }
 }
}
cerr << "-----------------------------------------------------"
          << endl;
cerr << "ERROR -- The wave form never passed the set threshold."
          << "Recheck your numbers." << endl;
cerr << "ERROR -- Returning zeroes..." << endl;
cerr << "-----------------------------------------------------"
```

```
                << endl;
   ThresholdPoint.x = 0.0;
   ThresholdPoint.y = 0.0;
   return (ThresholdPoint);
}
```

A.6 Trapezoidal shaper

The trapezoidal shaper equation is [71, 72]:

$$y_n = y_{n-1} + x_n - x_{n-m} - x_{n-m-k} + x_{n-2*m-k}. \tag{A.8}$$

With a shorter time constant it can pe used as a trigger or for pile-up inspection purposes.

```
double CWaveform::trapezoidalShaper(enum DetectorType DetType,
                                    unsigned int m,
                                    unsigned int k,
                                    struct PairXY TriggerPoint)
{
   unsigned int n;
   double elem_n_m,  elem_n_m_k, elem_n_2m_k;
   double dEnergy, dMin = +1.E+10, dMax = -1.E+10;

   if (DetType == GE_CENTRAL_CONTACT)
   {
    for (n = 0; n < m_iSize; n++)
    {
     // element x(n-m)
```

```
if((int)n -(int)m >= 0)
{
 elem_n_m = m_pWave[n-m] - TriggerPoint.y ;
}
else
{
 elem_n_m = 0.0;
}
// element x(n-m-k)
if((int)n - (int)m - (int)k >= 0)
{
 elem_n_m_k = m_pWave[n-m-k] - TriggerPoint.y;
}
else
{
 elem_n_m_k = 0.0;
}
// element x(n-2m-k)
if((int)n - 2*(int)m - (int)k >= 0)
{
 elem_n_2m_k = m_pWave[n-2*m-k] - TriggerPoint.y;
}
else
{
 elem_n_2m_k = 0.0;
}
m_pTrapezoid[n] = m_pTrapezoid[n-1]
         + (m_pWave[n] - TriggerPoint.y)
```

```
          - elem_n_m - elem_n_m_k + elem_n_2m_k;
  // calculate the extremes
  if (  m_pTrapezoid[n] > dMax)
  {
   dMax = m_pTrapezoid[n];
  }

  if (  m_pTrapezoid[n] < dMin)
  {
   dMin = m_pTrapezoid[n];
  }
 }
}
else if (DetType == GE_SEGMENT)
{
 for (n = (unsigned int) TriggerPoint.x; n < m_iSize; n++)
 {
  // element x(n-m)
  if((int)n -(int)m >= 0)
  {
   elem_n_m = TriggerPoint.y - m_pWave[n-m] ;
  }
  else
  {
   elem_n_m = 0.0;
  }

  // element x(n-m-k)
```

```
if((int)n - (int)m - (int)k >= 0)
{
 elem_n_m_k =  TriggerPoint.y - m_pWave[n-m-k];
}
else
{
 elem_n_m_k = 0.0;
}
// element x(n-2m-k)
if((int)n - 2*(int)m - (int)k >= 0)
{
 elem_n_2m_k = TriggerPoint.y - m_pWave[n-2*m-k];
}
else
{
 elem_n_2m_k = 0.0;
}
m_pTrapezoid[n] = m_pTrapezoid[n-1]
            + (TriggerPoint.y - m_pWave[n])
            - elem_n_m - elem_n_m_k + elem_n_2m_k;

// calculate extremes
if (  m_pTrapezoid[n] > dMax)
{
 dMax = m_pTrapezoid[n];
}
if (  m_pTrapezoid[n] < dMin)
{
```

```
      dMin = m_pTrapezoid[n];
     }
    }
   }
   dEnergy = dMax;//-dMin;
   return(dEnergy);
}
```

A.7 A differentiator-integrator shaper

A shaper using three parameters R (integration constant), D (differentiation constant), and τ (preamplifier decay time constant). It is a four-pass filter with an intermediary waveform (a_n).

$$a_n = x_n + (1 - \tau)x_n \tag{A.9}$$

$$y_n = a_n - a_{n-R} - a_{n-(R+D)} + a_{n-(2R+D)} \tag{A.10}$$

$$a_n = a_{n-1} + y_n \tag{A.11}$$

$$y_n = y_{n-1} + a_n \tag{A.12}$$

The energy is given by the maximum of the resulting y_n signal.

```
double CWaveform::shaper(double dDecayTimeConst,
                         double dR, double dD)
{
   double a, b, c;
   double dEnergy, dMin = +1.E+10, dMax = -1.E+10;
   int n;
```

```
a = 1.0-dDecayTimeConst;
for (n = 1; n < m_iSize; n++)
{
 m_pTrapezoid[n] = m_pWave[n] -a*m_pWave[n-1];
}
for (n = 0; n < m_iSize; n++)
{
 m_pDeriv1[n] += m_pTrapezoid[n];
 if (n > (int)dR)
 {
  m_pDeriv1[n] -= m_pTrapezoid[n-(int)dR];
 }
 if (n > ((int)dR+(int)dD))
 {
  m_pDeriv1[n] -= m_pTrapezoid[n-((int)dR+(int)dD)];
 }
 if (n > (2*(int)dR+(int)dD))
 {
  m_pDeriv1[n] += m_pTrapezoid[n-(2*(int)dR+(int)dD)];
 }
}
m_pTrapezoid[0] = 0.0;
for (n = 1; n < m_iSize; n++)
{
 m_pTrapezoid[n] = m_pTrapezoid[n-1]+m_pDeriv1[n];
}
m_pDeriv1[0] = 0.0;
for (n = 1; n < m_iSize; n++)
```

```
   {
    m_pDeriv1[n] = m_pTrapezoid[n]+m_pDeriv1[n-1];
   }
  //calculate extremes
  for (n = 1; n < m_iSize; n++)
  {
   if (m_pDeriv1[n] > dMax)
   {
    dMax = m_pDeriv1[n];
   }
   if (  m_pDeriv1[n] < dMin)
   {
    dMin = m_pDeriv1[n];
   }
  }
  dEnergy = dMax;// - dMin;
  return (dEnergy);
}
```

A.8 Statistics on a waveform segment

Extracts the mean and standard deviation for a section of the waveform. It is suitable for baseline calculations and simple noise amplitude estimation.

```
struct StatCoefs
CWaveform::calculateStatistics(unsigned int iBeginSample,
                        unsigned int iEndSample)
{
   double dMean = 0.0, dStdDev = 0.0, dVariance = 0.0;
```

```
   double dSum =0.0, dSumSquares = 0.0;
   struct StatCoefs Statistics;
   unsigned int i;
   unsigned int iIntervalSize;

   iIntervalSize = iEndSample - iBeginSample;
   for (i = iBeginSample; i < iEndSample; i++)
   {
    dSum += m_pWave[i];
    dSumSquares += m_pWave[i]*m_pWave[i];
   }
   dMean = dSum/iIntervalSize;
   dVariance = (dSumSquares
        - dSum*dSum/iIntervalSize)/(iIntervalSize - 1.);
   dStdDev = sqrt(dVariance);
   Statistics.mean = dMean;
   Statistics.stdev = dStdDev;
   return (Statistics);
}
```

A.9 RC-CR Filter

Described in detail in References [75] and [74], it is a succession of two single pole filter, a low-pass (integrator) followed by a high-pass (differentiator). It also applies a pole-zero correction to the shaped signal.

```
double CWaveform::shaperRC_CR(double dDecayTimeConstDiff,
         double dDecayTimeConstInt,
         double dPoleZeroCorrection)
```

```
{
   double dDecayFactorDiff, dDecayFactorInt;
   double dDF;

   double dEnergy = 0.0;
   double dBase = 0.0;
   dDecayFactorDiff = exp(-1./dDecayTimeConstDiff);
   dDecayFactorInt  = exp(-1./dDecayTimeConstInt);
   dDF = 0.5*(1+dDecayFactorDiff);
   // apply the differential filter (RC)
   for (unsigned int i = 2; i < m_iSize; i++)
   {
    m_pTrapezoid[i] = dDF * m_pWave[i] +
     (dPoleZeroCorrection - dDF)*m_pWave[i-1] +
     dDecayFactorDiff * m_pTrapezoid[i-1];
   }
   // apply the integral filter (CR)
   for (unsigned int i = 2; i < m_iSize; i++)
   {
    m_pTrapezoid[i] = (1.- dDecayFactorInt)*m_pTrapezoid[i] +
     dDecayFactorInt*m_pTrapezoid[i-1];
   }
   // energy is the max of the trapezoid shaped pulse
   for (unsigned int i = 0; i < m_iSize; i++)
   {
    if (m_pTrapezoid[i] > dEnergy)
    {
     dEnergy = m_pTrapezoid[i];
```

```
    }
    if (m_pTrapezoid[i] < dBase)
    {
     dBase = m_pTrapezoid[i];
    }
   }
   return dEnergy - dBase;
}
```

Bibliography

[1] R. du Rietz *et al. Phys. Rev. Lett.*, **93**:222501, 2004.

[2] A. Navin *et al. Phys. Rev. Lett.*, **85**:226, 2000.

[3] O. Sorlin *et al. Phys. Rev. Lett.*, **88**:092501, 2002.

[4] B.V. Pritychenko *et al. Phys. Rev. C*, **62**:051601, 2000.

[5] B.V. Pritychenko *et al. Phys. Rev. C*, **63**:047308, 2001.

[6] B.V. Pritychenko *et al. Phys. Rev. C*, **65**:061304, 2002.

[7] H. Scheit *et al. Phys. Rev. Lett.*, **77**(19):3967–3970, 1996.

[8] J.I. Prisciandaro *et al. Phys. Lett.*, **B510**:17, 2001.

[9] T. Otsuka *et al. Phys. Rev. Lett.*, **87**:082502, 2001.

[10] M. Honma *et al. Phys. Rev. C*, **65**:061301, 2002.

[11] S.N. Liddick *et al. Phys. Rev. Lett.*, **92**:072502, 2004.

[12] S.N. Liddick *et al. Phys. Rev. C*, **70**:064303, 2004.

[13] R.V.F. Janssens *et al. Phys. Lett.*, **B 546**:55, 2002.

[14] B. Fornal *et al. Phys. Rev. C*, **70**:064304, 2004.

[15] K.L. Yurkewicz *et al. Phys. Rev. C*, **70**:054319, 2004.

[16] G. Kraus *et al. Phys. Rev. Lett.*, **73**:1773, 1994.

[17] T. Glasmacher. *Annu. Rev. Nucl. Part. Sci.*, **48**:1, 1998.

[18] E.Z. Fermi. *Z. Phys.*, **29**:315, 1924.

[19] C.F. Weizsäcker. *Z. Phys.*, **88**:612, 1934.

[20] K. Alder *et al. Rev. Mod. Phys.*, **28**:432, 1956.

[21] F.D. Becchetti *et al. Phys. Rev. C*, **40**:1104, 1989.

[22] J.J. Kolata *et al. Nucl. Instr. and Meth. B*, **503**:503, 1989.

[23] J.A. Brown *et al. Phys. Rev. Lett.*, **66**:2452, 1991.

[24] M. Oshima *et al. Nucl. Instr. and Meth. A*, **312**:445, 1992.

[25] A. Winther and K. Alder. *Nucl. Phys.*, **A319**:518, 1979.

[26] T. Glasmacher. *Nucl. Phys. A*, **693**:90–104, 2001.

[27] A. Gade *et al. Phys. Rev. C*, **68**:014302, 2003.

[28] K. L. Miller. *Study of Neutron-Deficient Nickel Isotopes Via One-Neutron Knock-out and Intermediate-Energy Coulomb Excitation.* PhD thesis, Michigan State University, 2003.

[29] M.A. Deleplanque *et al. Nucl. Instr. and Meth. A*, **430**:292–310, 1999.

[30] I.-Y. Lee *et al. Nucl. Phys. A*, **746**:255C–259C, 2004.

[31] D. Bazzacco. *Nucl. Phys. A*, **746**:248C–254C, 2004.

[32] D.-C. Dinca *et al. Phys. Rev. C*, **71**:041302, 2005.

[33] B. A. Brown. *Prog. in Part. and Nucl. Phys.*, **47**:517, 2001.

[34] F. Tondeur. *Z. Phys.*, **A 288**:97, 1978.

[35] P. Haensel and J. L. Zdunik. *Astron. Astrophys.*, **222**:353, 1989.

[36] J. Dobaczewski *et al. Phys. Rev. Lett.*, **72**:981, 1994.

[37] J.M. Pearson *et al. Phys. Lett. B*, **387**:455, 1996.

[38] G. A. Lalazissis *et al. Phys. Lett.*, **B 418**:7, 1998.

[39] A. Huck *et al. Phys. Rev. C*, **31**:2226, 1985.

[40] D.C. Radford *et al. Phys. Rev. Lett.*, **88**:222502, 2002.

[41] D.J. Morrissey *et al. Nucl. Instr. and Meth. B*, **204**:90, 2003.

[42] D. Bazin *et al. Nucl. Instr. and Meth. B*, **204**:629, 2003.

[43] J. Yurkon *et al. Nucl. Instr. and Meth. A*, **422**:291, 2001.

[44] W.F. Mueller *et al. Nucl. Instr. and Meth. A*, **466**:492, 2001.

[45] GEANT. CERN library long writeup. Technical Report W5013, CERN, 1994.

[46] H. Scheit. *Low-Lying Collective Excitations in Neutron-Rich Even-Even Sulfur and Argon Isotopes Studied via Intermediate-Energy Coulomb Excitation and Proton Scattering.* PhD thesis, Michigan State University, 1998.

[47] H. Olliver *et al. Phys. Rev. C*, **68**:044312, 2003.

[48] S. Raman *et al. Atomic Data and Nuclear Data Tables*, **78**:1, 2001.

[49] Zhou Chunmei. *Nucl. Data Sheets*, **76**:399, 1995.

[50] B.A. Brown *et al. Phys. Rev. C*, **14**:1016, 1976.

[51] H. Junde. *Nucl. Data Sheets*, **90**:1, 2000.

[52] M. Hjorth-Jensen *et al. Phys. Rep.*, **261**:125, 1995.

[53] M. Honma *et al. Eur. Phys. J. A*, *Proc. Fourth Int. Conf. on Exotic Nuclei and Atomic Masses (ENAM04)*, 2005.

[54] B. Fornal *et al.* :to be published., 0000.

[55] B. A. Brown and B. H. Wildenthal. *Phys. Rev. C*, **21**:2107, 1980.

[56] B.A. Brown *et al. Nucl. Phys. A*, **277**:77–108, 1977.

[57] T. Mizusaki. *RIKEN Accel. Prog. Rep.*, **33**:14, 2000.

[58] P.F. Mantica *et al. Phys. Rev. C*, **67**:014311, 2003.

[59] P.F. Mantica *et al. Phys. Rev. C*, **68**:044311, 2003.

[60] L.A. Riley *et al. Phys. Rev. C*, :to be published., 2005.

[61] C.M. Campbell *et al. First measurement of an excited state in* ^{40}Si, :to be published., 2005.

[62] D. Bazin *et al. Phys. Rev. Lett.*, **91**:012501, 2003.

[63] A. Gade *et al. Phys. Rev. C*, **69**:034311, 2004.

[64] S. Ramo. *Proc. IRE*, **27**:584, 1939.

[65] W. Shockley. *J. Appl. Phys.*, **9**:635, 1938.

[66] G. F. Knoll. *Radiation Detection and Measurement Nuclear Reactions, 3rd ed.* John Wiley & Sons, Inc., 2000.

[67] L. Mihailescu *et al. Nucl. Instr. and Meth. A*, **447**:350–360, 2000.

[68] R. Fox *et al. IEEE Trans. Nucl. Sci.*, 2004.

[69] R. Fox *et al. 13th IEEE-NPSS Real Time Conference*, 2003.

[70] Th. Kroell *et al. Nucl. Instr. and Meth. A*, **371**:489–496, 1996.

[71] V. Radeka. *Nucl. Instr. and Meth.*, **99**:525–539, 1972.

[72] Valentin T. Jordanov and Glenn F. Knoll. *Nucl. Instr. and Meth. A*, **345**:337–345, 1994.

[73] A. Georgiev and W. Gast. *IEEE Trans. Nucl. Sci.*, **40**:770–779, 1993.

[74] T. Kihm *et al. Nucl. Instr. and Meth. A*, **489**:334–339, 2003.

[75] Steven W. Smith. *The Scientist and Engineer's Guide to Digital Signal Processing*. California Technical Pub., 1997.